Doctor thesis

A study of the $\eta\pi^+\pi^-\pi^0$ system centrally produced in pp interactions at 450 GeV/c

Department of Physics,
Tohoku University

Tetsushi Hino

December, 1998

Abstract

The purpose of this thesis is to search for a hybrid meson state which has an exotic quantum number $J^{PC} = 1^{-+}$ in the $f_1(1285)\pi^0$ system produced in the pp central production process

$$pp \rightarrow p_f X^0 p_s,\ X^0 \rightarrow f_1(1285)\pi^0,\ f_1(1285) \rightarrow \eta\pi^+\pi^-,$$

at 450 GeV/c incident proton beam momentum from CERN SPS observed by the WA102 experiment.

The hybrid meson state is a bound system of a $q\overline{q}$ pair and a valence gluon. The existence of such hadronic states with extra gluonic degree of freedoms is predicted by the presence of the self-interaction of gluons, which is a natural consequence of the non-Abelian nature of Quantum Chromodynamics (QCD). The non-Abelian nature of QCD is essential to a successful explanation for characteristic behavior of the strong force, such as "*asymptotic freedom*" and "*infrared slavery*", but it has not been proved experimentally so far. The observation of hybrid states would give a direct proof of this primary of QCD.

The analysis of the $f_1(1285)\pi$ channel is strongly motivated by the prediction of the flux tube model: the model predicts that the hybrid state with $J^{PC} = 1^{-+}$ will preferentially decay into the $f_1(1285)\pi$ channel. The $J^{PC} = 1^{-+}$ quantum number is not allowed for ordinary $q\overline{q}$ pairs, therefore the observation of the resonant state with 1^{-+} leads to confirmation of the existence of the non-$q\overline{q}$ state unambiguously. Currently three previous experiments reported the observation of the 1^{-+} wave through the partial wave analysis in the $f_1(1285)\pi$ system obtained from the $\pi^- p$ diffractive reaction. They observed that the 1^{-+} intensity was distributed around 2.0 GeV/c^2, which is in good agreement with the model prediction for the hybrid mass. Thus the 1^{-+} wave in the $f_1(1285)\pi$ channel is considered to be the best candidate of the hybrid meson at present. However, its assignment as a hybrid state has not been confirmed because of difficulty to observe the phase motion of the 1^{-+} wave due to its rather broad observed width and a lack of any well-established state in the $f_1(1285)\pi$ channel which is needed as a reference state for the observation of the phase motion. In order to disclose the nature of the 1^{-+} wave in the $f_1(1285)\pi$ channel, more data from different reactions appear to be needed.

The central production process is believed to be one of "gluon rich" processes, where gluonic exotic states are expected to be produced preferentially. In the reaction, both of the beam and target proton exchange particles and form the neutral

meson system X^0. The subscripts f and s represent that the beam and target proton are scattered as the fastest and slowest particle in the laboratory frame, respectively. As the center-of-mass energy of the reaction becomes higher, Pomeron exchange is considered to dominate the reaction and hence formed X^0s are thought to have gluonic content more hopefully. Therefore if the 1^{-+} wave observed in the $f_1(1285)\pi$ channel is really a hybrid state, it is expected to be produced dominantly in the central production process.

In the experiment, the fast and slow proton and charge particles in the final state were measured by the Omega spectrometer which is composed of a superconducting magnet with a central field of 1.35 T, and gammas from decays of neutral particles were detected by the hodoscope electromagnetic calorimeter GAMS. GAMS consists of 64×64 lead glass matrix cells and measures detected positions and energies of gammas. The experimental trigger was designed to reject the pp elastic scattering and target diffraction process, both of which dominate the central production process. Through 90 days in 1995 run and 95 days in 1996 run, total 5×10^8 events were obtained.

Various offline cuts were applied and finally total of 1811 events were selected from the 1995 and 1996 data as centrally produced $f_1(1285)\pi^0$ candidates. In order to obtain the spin parity of the observed system, the partial wave analysis (PWA) based on the maximum likelihood fit method was attempted. The decay amplitude of the system was represented by the spin-orbit (LS) scheme using spherical harmonics, assuming two isobars, $f_1(1285)/\eta(1295)$ in the $\eta\pi^+\pi^-$ system for the primary decay and $a_0^\pm(980)$ in the $\eta\pi^\pm$ system for the secondary decay. All decay angles were with respect to the exchanged particle axis. Data samples of the 1995 and 1996 runs were combined by taking into account the difference between detector acceptances, and were included in the fit simultaneously. To stabilize the fit, the combined data sample was divided into three 0.4 GeV/c^2 mass bins from 1.4 to 2.6 GeV/c^2.

The result of the PWA showed that a combination of exotic 1^{-+} waves of $f_1(1285)\pi^0$ and $\eta(1295)\pi^0$ was best fitted and gave about 3σ larger likelihood than other combinations in the 1.8–2.2 and 2.2–2.6 GeV/c^2 regions. On the other hand, any combination did not have a significantly larger likelihood than the others in the 1.4–1.8 GeV/c^2 region. Especially the 1^{++} wave, which was observed dominantly at ~ 1.7 GeV/c^2 in all three previous $\pi^- p$ diffractive reaction experiments, had only a considerably smaller likelihood in any mass bin.

In conclusion, only the combination of the exotic $f_1(1285)\pi^0$ and $\eta(1295)\pi^0$ 1^{-+} waves was observed with a significant likelihood difference. As it was impossible to see the phase motion of waves due to the limited statistics, it cannot be concluded that the 1^{-+} waves are resonant states. However, it is considered that the clear appearance of the exotic 1^{-+} wave in the "gluon rich" central production suggest the hybrid nature of the 1^{-+} wave in the $f_1(1285)\pi$ channel.

Contents

1 Introduction **1**
1.1 Purpose 1
1.2 Non-$q\bar{q}$ mesonic states—Exotic mesons 1
1.3 How to look for exotic mesons 3
1.4 Overview of this thesis 6

2 Searches for 1^{-+} exotics **7**
2.1 Experimental searches 7
2.2 Interpretation of 1^{-+} exotics 17
2.3 Summary 19

3 WA102 experiment **21**
3.1 WA102 experimental setup 21
3.1.1 Overview of setup 21
3.1.2 Beam measurement 22
3.1.3 Target 26
3.1.4 Slow proton measurement 26
3.1.5 Fast proton measurement 30
3.1.6 Medium track measurement 30
3.1.7 Gamma detection 31
3.1.8 Experimental trigger 33
3.2 Event statistics 33
3.3 Event reconstruction 34
3.3.1 Reconstruction of charged track 34
3.3.2 Reconstruction of gamma event 34

4 Event selection for the $\eta\pi^+\pi^-\pi^0$ channel in WA102 **42**
4.1 Removal of charged track impacts on GAMS 42
4.2 Removal of gammas due to noise 42
4.3 Removal of other channels 44
4.4 Cut on the confidence level 48
4.5 Removal of the fast proton correlation 50
4.6 Results of the event selection 50

5 Analysis of the $f_1(1285)\pi$ channel **54**
5.1 Selection of the $f_1(1285)\pi^0$ channel 54
5.2 Study of the mass spectrum 55
5.3 Spin analysis for the $f_1(1285)\pi^0$ channel 60
5.3.1 Definition of axes 60
5.3.2 Calculation of decay amplitudes 61
5.3.3 Study of the detector acceptance 63
5.3.4 Results of the spin analysis 71
5.4 Discussion 80

6 Conclusion **84**

Acknowledgements

First of all, I would like to thank to Professor Takemi Nakagawa, for his warm, rigorous, patient and great deal of guidance for me through all my student life. He has always given me continual encouragement, precious advises and many supports at various stages.

I would like to express my great appreciation to Professor Tsuneaki Tsuru and Professor Kunio Takamatsu for giving me an opportunity to participate in research on meson spectroscopy as a member of the WA102 collaboration. They have patiently guided and taught me whole in my activity for this thesis.

I would like to thank Professors Jean-Pierre Stroot, Jean-Pierre Peigneux and Yuri Prokoshkin (who deceased unfortunately in 1997 spring) who are leaders of the GAMS collaboration, and willingly allow me to join the experiment. I would also like to thank to the WA102 spokesperson, Dr Andrew Kirk, who has never been too busy to answer to my persistent questions very kindly and patiently. I would never have completed my thesis without great amount of guidance from him. My special thanks must also be given to Dr Alexander Singovski who is the WA102 contactperson and has given me a lot of crucial guidance, too. Thanks are also extended to Dr Frank Votruba who willingly presented his data for me, and Dr Andrei Sobol who has provided a nice kinematical fitting program and given helpful comments to me. I would like to thank all other members of the GAMS and Omega group, especially I will never forget warm supports from Professor Anatoli Lednev and Dr Viktor Kolosov with whom I enjoyed coffee time in the GAMS barrack during beam time shifts, and Dr Petya Shagin with whom I greeted 1998 new year during his stay at KEK.

I would like to thank all members of the KEK-GAMS group for their special supports during my stay at KEK: Professor Susumu Inaba who has always given me warm supports, Dr Yoshiji Yasu for much help with computing problems, Professor Hajime Shimizu who has given very useful comments on my analysis and a lot of encouragement for my activity. I am particularly grateful to Dr Toru Kinashi and Dr Taku Ishida who have continuously guided my analysis with many helpful and precise suggestions. I have also received much guidance and friendship from members of the AIDA experiment, Professor Hideyuki Kawai, Hiroshi Yoshida, Yasuhisa Tajima, Hirofumi Nakayama, Toshinari Matsumoto, Sosuke Horikawa and all other members. Special thanks go to Dr Shigeru Ishimoto who has given me many nice advices for my comfortable stay at CERN, and to Noriaki Hidaka who has given a lot of encouragement during the hardest last three months.

Now many thanks go to members of Experimental Nuclear Physics Group at Tohoku University and Nuclear Instrument Group of CYRIC. I would like to thank Professors Osamu Hashimoto, Hikonojo Orihara, Tsutomu Touhei and Kousuke Kageyama who have guided my activity and given much encouragement. I will never forget a memory of Professor Takashi Yamaya who gave many good advices and warm encouragement (and a good wine). I would like to express my great appreciation to all staffs and fellow students: Dr Yuu Fujii who has given a lot of help and useful tips for all kinds of problems, Akiyoshi Yamazaki and Asaki Yamamoto with whom I have learned (and drunk much alcohol) together over six years, Tsuyoshi Aizawa, Mitsunobu Matsunaga, Tsuyoshi Kuzumaki, Yoshihiro Saitou, Masato Hirai and secretaries Naoko Kawamura and Yumi Nomura who all have made my campus life much more fruitful, Dr Atsuki Terakawa who has given many supports to my activity at CYRIC, Morio Kato who has supported my studies and given much encouragement (and nicely caught my wild pitches) ... it is much to be regretted that I cannot give here all names of whom I am indebted to in my student life.

Finally, I would like to express my gratitude to my parents, who allow me to go on to the doctor course and have always given all kinds of supports to me. I would like to devote this thesis to my father, who had longed to see it (though maybe he would not understand) but can never see it.

Chapter 1

Introduction

1.1 Purpose

The purpose of this thesis is to search for a hybrid meson state which has an exotic quantum number $J^{PC} = 1^{-+}$ in the $f_1(1285)\pi^0$ system produced in the pp central production process

$$pp \rightarrow p_f X^0 p_s,\ X^0 \rightarrow f_1(1285)\pi^0,\ f_1(1285) \rightarrow \eta\pi^+\pi^-,$$

at 450 GeV/c incident proton beam momentum from CERN SPS observed by the WA102 experiment. The subscripts f and s represent that the beam and target proton are scattered as the fastest and slowest particle in the laboratory frame, respectively.

1.2 Non-$q\bar{q}$ mesonic states—Exotic mesons

According to the Standard Model, which has been extremely successful in explaining particle physics up to present energy scales, all hadronic matter is composed of quarks and gluons. The simplest representations of $SU(3)$ color singlet for hadrons, that is, *mesons* which consist of valence $q\overline{q}$ pairs and *baryons* which consist of 3 valence quarks, have been very successful to classify the observed spectra into *multiplets* by their spin J, parity P and charge conjugation C. Table 1.1 shows examples of meson nonets, grouped by their isotopic spin I.

Now the concerns of the hadron physics have been on the new forms of hadronic matter beyond the simple $q\overline{q}$ or qqq picture. In the 0^{++} sector of Table 1.1, assignments of the $I = 0, 1$ parts are not confirmed in fact. For the $I = 1$ part, two candidates, $a_0(980)$ and $a_0(1450)$, are observed for only one expected state and more than four states[1] are reported for the $I = 0$ part for only two states to emerge.

[1]Currently 7 states in the mass range below 2.2 GeV/c^2 are listed on the 1998 edition of the Particle Data Listing and four states out of them, $f_0(400\text{–}1200)$, $f_0(980)$, $f_0(1370)$ and $f_0(1500)$, are confirmed as resonant states[1].

$^{2S+1}L_J$	J^{PC}	$u\overline{d}, u\overline{u}, d\overline{d}$ $I=1$	$u\overline{u}, d\overline{d}, s\overline{s}$ $I=0$	$u\overline{s}, d\overline{s}$ $I=1/2$
$^1S_0$	0^{-+}	π	η, η'	K
$^3S_1$	1^{--}	ρ	ω, ϕ	$K^*(892)$
$^1P_1$	1^{+-}	$b_1(1235)$	$h_1(1170), h_1(1380)$	$K_{1B}^\dagger$
$^3P_0$	0^{++}	$a_0(980)$? $a_0(1450)$?	$f_0(400\text{–}1200)$? $f_0(980)$? $f_0(1370)$? $f_0(1500)$?	$K_0^*(1430)$
$^3P_1$	1^{++}	$a_1(1260)$	$f_1(1285), f_1(1510)$	$K_{1A}^\dagger$
$^3P_2$	2^{++}	$a_2(1320)$	$f_2(1270), f_2'(1525)$	$K_2^*(1430)$

† The K_{1A} and K_{1B} are nearly equal (45°) mixes of the $K_1(1270)$ and $K_1(1400)$.

Table 1.1: Meson nonets containing light quarks.

Their masses lie too closely each other to regard any of them as a radial excitation. These facts would suggest the existence of objects beyond a simple $q\overline{q}$ structure. Our interests are now on investigation of such non-$q\overline{q}$ mesonic states—exotic mesons.

One of such exotic states is the $qq\overline{q}\overline{q}$ multiquark state. It is the simplest meson system that can have color singlet quantum numbers except $q\overline{q}$[2]. It is suggested that the structure can be either of a baglike one or a cluster of mesons. For example, $a_0(980)$ and $f_0(980)$ are thought to be $K\overline{K}$ *molecules*[1].

The requirement of the models beyond the simple quark model has been urged not only by the observation of the extra meson states, but also by the demand from Quantum Chromodynamics (QCD), the quantum field theory describing the interactions of quarks and gluons. It is expressed mathematically as a non-Abelian gauge theory on the result of a requirement of the $SU(3)$ local gauge invariance on the quark color fields. Its physical interpretation suggests an important prediction that the carrier of the strong force, that is, the gluon is self-interacting. This becomes clear if the QCD Lagrangian

$$\begin{gathered}\mathcal{L} = \overline{q}(i\gamma^\mu\partial_\mu - m)q - g(\overline{q}\gamma^\mu T_a q)G_\mu^a - \frac{1}{4}G_{\mu\nu}^a G_a^{\mu\nu} \\ (G_{\mu\nu}^a = \partial_\mu G_\nu^a - \partial_\nu G_\mu^a - g f_{abc} G_\mu^b G_\nu^c)\end{gathered} \tag{1.1}$$

is rewritten in the symbolic form[3]:

$$\mathcal{L} = \text{“}\overline{q}q\text{”} + \text{“}G^2\text{”} + g\text{“}\overline{q}qG\text{”} + g\text{“}G^3\text{”} + g^2\text{“}G^4\text{”}.$$

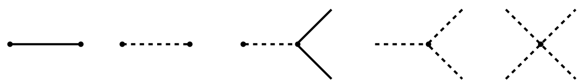

The first three terms describe the free propagation of the quarks, gluons and quark–gluon interactions and the remaining two terms show the presence of three and four gluon vertices. This feature of QCD implies the existence of the further exotic meson states. They are a bound system which contains not only valence quarks but also valence gluons, called *hybrid*, or a system which is composed totally of valence gluons, called *glueball*. Conversely, the observation of these exotic states with extra gluonic degree of freedoms would be a direct proof of the non-Abelian nature of QCD.

At present there are many candidate glueballs and hybrid states, reported experimentally. In the next section, experimental approaches to these states are discussed.

1.3 How to look for exotic mesons

The difficulty in classifying the gluonic states is due to an absence of reliable ways to predict their observable properties such as mass, spin, decay mode, etc.. QCD has been very successful in describing hadronic reactions, but for hadron structures its analytic solutions are not available because the perturbation method becomes unworkable inside hadrons due to large strong couplings. Instead, many models have been proposed to draw observable characteristics of exotic mesons, but most of them need many parameters and their predictions are strongly parameter dependent, hence their reliability was considered to be quite poor.

Recently, however, there have been enormous improvements in the prediction powers. One of them is the numerical approach to the solution of QCD for hadron masses, based on the lattice gauge theory. Two recent calculations predict the lowest lying glueball state has $J^{PC} = 0^{++}$, mass 1.5–1.7 GeV/c^2 and width 100–150 MeV/c^2[4, 5]. Their calculations still need more improvements since they all employ the quenched approximation and the results show some discrepancies. Nevertheless, these results support the existence of the scalar glueball, which has been suggested by the observation of extra states in the 0^{++} sector, as can be seen in Table 1.1. For example, $f_0(1500)$ is now believed to be the most probable candidate for the scalar glueball[1].

While the precision of the theoretical prediction has been improved as described above, it also appears clear that gluonic states do not exhibit strikingly different properties from ordinary mesons (except their quantum numbers, which will be discussed later). For example, the scalar glueball would have a mass 1.5–1.7 GeV/c^2 which is comparable with those of other ordinary scalar mesons. This means that the theoretical prediction supports the existence of the scalar glueball but cannot distinguish it from the other states unless the precision of the calculation is further improved. Thus, in order to classify the scalar glueball, qualitative explanations appear to be still needed such as flavor independent coupling to quarks, suppressed coupling to photons, etc.. The assignment of $f_0(1500)$ as a scalar glueball is supported by many experimental results, which suggest such characteristic properties of $f_0(1500)$.

At present, the only apparent feature of exotic mesons, which can distinguish them from ordinary mesons, is their quantum numbers. For the $q\overline{q}$ system, the total intrinsic spin S can be either 0 or 1 since quarks have spin $\frac{1}{2}$. The total spin J of the meson is then the vector sum of its intrinsic spin and the relative orbital angular momentum L between the quark and antiquark. The parity of the meson and the charge conjugation of its neutral member is then given by

$$P = (-1)^{L+1},\ C = (-1)^{L+S}. \tag{1.2}$$

From the relation above, it is apparent that some combinations of J^{PC}, for example 1^{-+}, are disallowed for the ordinary $q\overline{q}$ pair. This is not the case for glueballs or hybrid mesons, which are combinations of 1^{--} gluons or mixtures of quarks and gluons. Hence an observation of states having these exotic quantum numbers, so-called "oddball", is immediately an unambiguous confirmation of the existence of exotic states.

It is also believed that probes of "gluon rich" channels are needed for the observation of gluonic states. Up to a few year ago, most hadron spectroscopy had been performed using peripheral reactions where the interactions are dominated by quarks and these channels are considered not to be "gluon rich" enough to make gluonic states observable. In practice, experimental observations of new states which do not fit well into the standard $q\overline{q}$ multiplets have been made now in channels which are thought to be gluon rich[6]. Figure 1.1 summarizes several reactions which are thought to be good sources of such gluon rich channels.

(a) J/Ψ decay. This channel has well defined initial state properties and a relatively limited number of final states, so they do not suffer from large backgrounds. Both of the hadronic decay (a) and the radiative decay (a') are believed to be a highly gluon rich channel.

(b) Central production. At high center-of-mass energy and low four momentum transfered at the two exchange vertices, Reggeon–Pomeron and Pomeron–Pomeron exchanges become significant relatively to Reggeon–Reggeon exchange[7]. Since the Pomeron is considered to be a multi-gluon state, the central production involving Pomeron exchange is believed to be gluon rich.

(c) Proton-antiproton annihilation. The annihilation region of quarks and antiquarks is thought to be a source of gluons.

(d) Special hadronic reactions. A example is shown here, where the $\phi\phi$ system is thought to be produced through an intermediate state containing gluons. Reactions of this kind which have disconnected quark lines are called as OZI violating[8, 9, 10].

The central production (b) is the one which has been studied by the WA102 experiment.

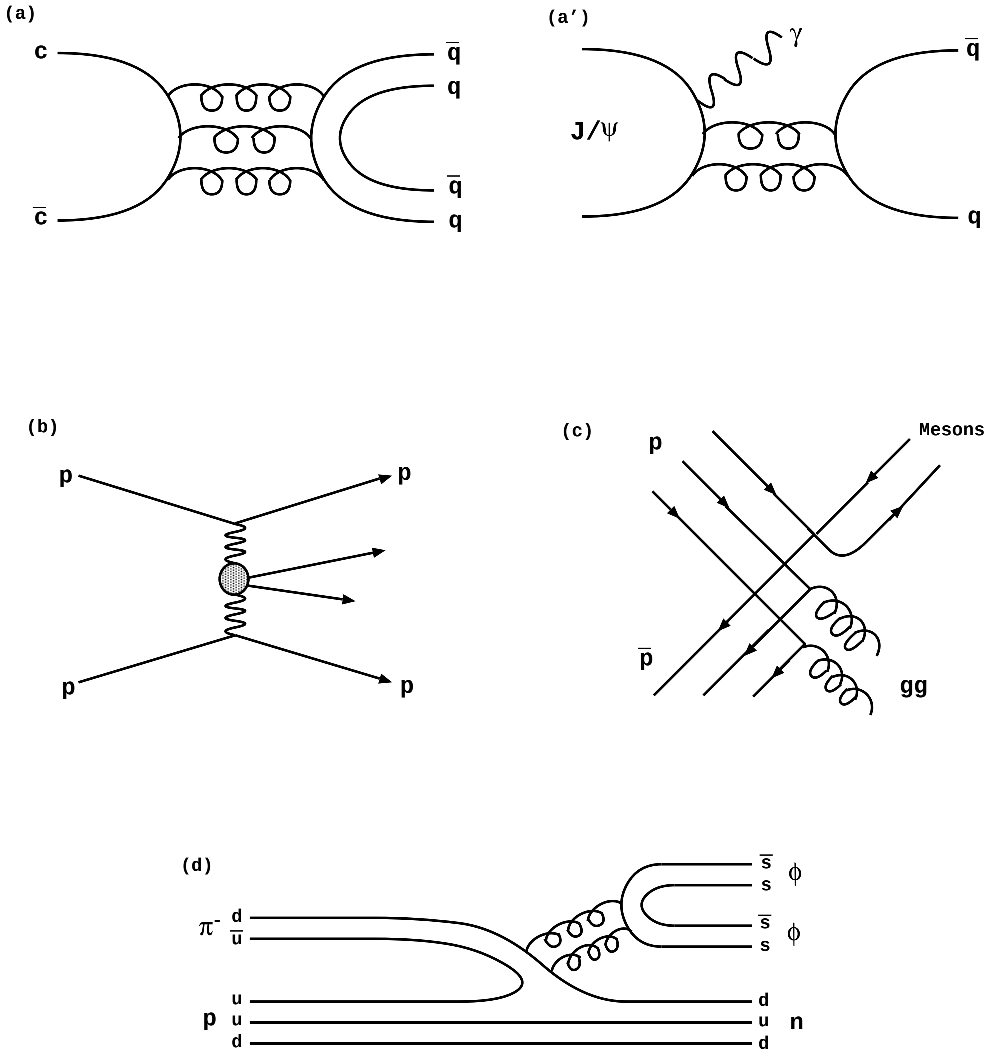

Figure 1.1: Examples of gluon rich channels.

1.4 Overview of this thesis

At present the 1^{-+} wave has been observed in several different channels: $\eta\pi$, $\eta'\pi$, $\rho\pi$, $f_1(1285)\pi$, etc.. The decay of the hybrid meson into the $f_1(1285)\pi$ channel was predicted by the flux tube model[11, 12, 13, 14] and three preceding experiments have reported the observation of the 1^{-+} wave in the $f_1(1285)\pi$ channel. In spite of the several observations of the 1^{-+} waves, however, classification into a hybrid meson or other exotic states has not been established for any 1^{-+} wave yet. The present circumstances of the searches for the 1^{-+} exotics will be described in chapter 2.

Data used in this thesis are from the WA102 experiment. The WA102 experiment has been designed to observe the exclusive central production process. Details of the experimental setup will be described in chapter 3.

In the following chapters, details of the analysis of the $\eta\pi^+\pi^-\pi^0$ channel is described. Firstly event selection procedures for the $\eta\pi^+\pi^-\pi^0$ channel will be described in chapter 4. Then a description of the analysis of the $f_1(1285)\pi^0$ channel will be given and results of the analysis will be discussed in chapter 5.

Finally, relevant conclusions will be drawn and possibilities for further studies discussed in chapter 6.

Chapter 2

Searches for 1^{-+} exotics

At present it is considered that the best way to confirm the existence of exotic meson states unambiguously is to search for resonant states with exotic J^{PC} quantum numbers which cannot be coupled by the ordinary $q\overline{q}$ pair. Especially the $J^{PC} = 1^{-+}$ state has been the most preferred object for that purpose, since its quantum number can be approached easily, for example, by a combination of $I = 0$ and 1 pseudoscalar mesons with the relative P-wave angular momentum.

Now candidates of the 1^{-+} exotic state have been reported on several channels. In particular, for each channel of the $\eta\pi$, $\eta'\pi$, $\rho\pi$ and $f_1(1285)\pi$, more than one experimental group have reported the observation of the 1^{-+} exotic wave. However, any of them has not been successfully classified as a glueball, hybrid nor multiquark state. This is because not only the ambiguity of the data analysis but also that of the interpretation of analysis results cannot be excluded. To confirm the existence of the 1^{-+} state, a consistent explanation through all the observed 1^{-+} exotic waves in different channels is strongly needed now.

In this chapter the current status of the search for the 1^{-+} state is described. The results of the preceding experiments are reviewed on each decay channel and various interpretations of 1^{-+} states currently suggested are the summarized.

2.1 Experimental searches

All reports for observations of the 1^{-+} wave are listed in Table 2.1, and details of each observation are described in the following.

$\eta\pi$ channel

The $\eta\pi$ channel is the simplest channel where the $J^{PC} = 1^{-+}$ state can be searched for. η has $I^G = 0^+$ and π has 1^-, thus the $\eta\pi$ system has $I^G = 1^-$, which corresponds to $C = +$ for the neutral member. Therefore the P-wave angular momentum between η and π, which are both $J^P = 0^-$, leads uniquely to $J^{PC} = 1^{-+}$. The experimental search for the 1^{-+} state in the $\eta\pi$ channel is thus to look for the

	P_{beam} (GeV/c)	channel	mass (MeV/c^2)	width (MeV/c^2)
$\pi^- p$ charge exchange				
GAMS	32,38,100	$\eta\pi^0$	~ 1300	
BNL E852	18	$\eta\pi^0$	seen	
$\pi^- p$ diffractive				
KEK E179	6.3	$\eta\pi^-$	1323.1 ± 4.6	143.2 ± 12.5
VES	37	$\eta\pi^-$	~ 1370	~ 380
		$\eta'\pi^-$	1572 ± 18	550 ± 57
		$\rho\pi^-$	~ 1600	~ 200
		$f_1(1285)\pi^-$	seen	
BNL E818	18	$f_1(1285)\pi^-$	1600–2200	
BNL E852	18	$\eta\pi^-$	1370 ± 16	385 ± 40
		$\eta'\pi^-$	~ 1600	
		$\rho\pi^-$	1593 ± 8	168 ± 20
		$f_1(1285)\pi^-$	1600–2200	
$\overline{p}n$ annihilation				
Crystal Barrel		$\eta\pi^-, \eta\pi^0$	1400 ± 20	310 ± 50

Table 2.1: Summary of observations on $J^{PC} = 1^{-+}$ exotic waves.

resonant state with the P-wave angular momentum, which can be investigated by the two-body partial wave analysis (PWA) since both of η and π can be observed unambiguously.

The first report of the observation of the $J^{PC} = 1^{-+}$ state was given in this channel by the GAMS collaboration[15]. They studied the charge exchange reaction

$$\pi^- p \rightarrow \eta\pi^0 n, \tag{2.1}$$

at 100 GeV/c incident beam momentum and observed the significant P_0-wave contribution on the $\eta\pi^0$ partial wave at the $\eta\pi^0$ effective mass of ~ 1.4 GeV/c^2. The notation for the partial wave is $L_{\lambda\pm}$: the angular momentum L between η and π, helicity λ and the naturality of the exchanged particle[1]. Here L_0 means the zero helicity formed by unnatural parity exchange (UPE). They also observed that the phase variation of the P_0-wave relative to that of the well-established $\eta\pi^0$ D-wave, $a_2(1320)$ state, was compatible to that of the resonance state, thus they concluded that the 1^{-+} wave is the first evidence of the exotic 1^{-+} state. This state is listed as $\hat{\rho}(1405)$ in PDG[1]. However, a problem was pointed out on their analysis[16, 17]. GAMS group reported that $a_2(1320)$ and $\hat{\rho}(1405)$ were observed in UPE (P_0-wave) which is inconsistent with the results of the previous experiments and the prediction of the Regge theory that the ratio of the cross section of production for $a_2(1320)$

[1] $+$ $\cdots$ natural parity exchange (parity $= (-1)^J$).
$-$ $\cdots$ unnatural parity exchange ($(-1)^{J+1}$)

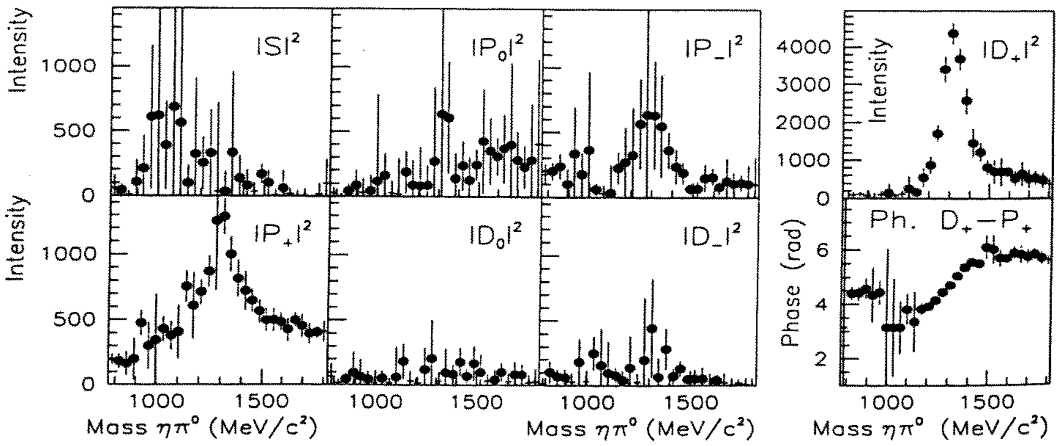

Figure 2.1: GAMS reanalyzed $\eta\pi^0$ partial wave intensities[15]. The relative $D_+ - P_+$ phase motion can be interpreted as being due to the phase motion of D_+-wave ($a_2(1320)$) only.

state between UPE and natural parity exchange (NPE) is proportional to $1/p$, where p denotes the incident beam momentum. That is, in the high energy region NPE is believed to dominate the reaction. Yu.D.Prokoshkin and S.A.Sadovsky claimed that the discrepancy was caused by the use of an approximate likelihood function in the PWA, which is valid only if the number of events available in the analysis is large enough[16, 17]. Recently the GAMS group reported the reanalysis of their data together with the analysis of newly obtained data with different incident beam momentum of 32 and 38 GeV/c as a preliminary result[6]. Their new result showed the significant $\eta\pi^0$ 1^{-+} signal in the P_+-wave but its phase does not show a clear resonant behaviour (Fig. 2.1).

The KEK E179 experiment investigated the diffractive reaction[18]

$$\pi^- p \rightarrow \eta\pi^- p, \tag{2.2}$$

at 6.3 GeV/c incident beam momentum. Their aim was to search for the isovector partner of $\hat{\rho}(1405)$. In their PWA, a clear enhancement was observed in NPE, at the lower mass $\sim$ 1.3 GeV/c^2 and with the narrower width $\sim$ 0.14 MeV/c^2 than those observed by GAMS collaboration. The phase of the P_+-wave does not show distinct variation relative to the D_+-wave ($a_2(1320)$), which suggests that the P_+-wave is also a resonant state (Fig. 2.2).

VES[19] and BNL E852 collaboration[20] also reported the P_+-wave on $\eta\pi^-$ channel, which are very consistent each other as for the observed masses and widths (Fig. 2.3(a) and 2.4). E852 studied the reaction (2.2) with the incident beam momentum 18 GeV/c and VES studied the same reaction using the Be target with the incident beam momentum 37 GeV/c. The behaviour of the phase and amplitude of the P_+ wave in both experiments can be well explained by the presence of a resonance with mass $\sim$ 1.37 GeV/c^2 and width $\sim$ 0.38 GeV/c^2. The compatibility of

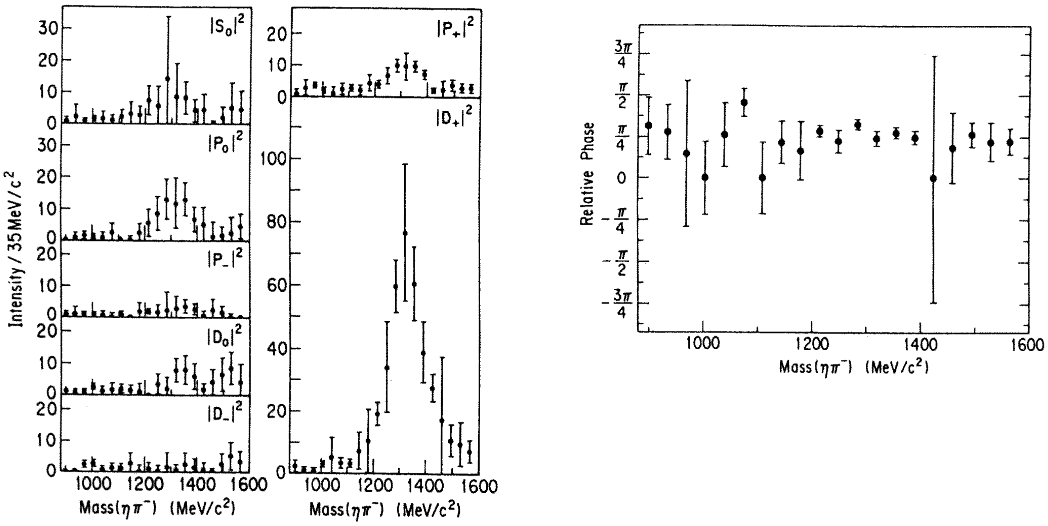

Figure 2.2: KEK $\eta\pi^-$ partial wave intensities[18]. The phase motion (right figure) shows that of the D_+-wave relative to the P_+-wave.

the two results appears to show that the experiments and analysis techniques are well understood and give reproducible results. E852 also reported their preliminary analysis of $\eta\pi^0$ channel in the reaction (2.1) with the incident beam momentum 18 GeV/c[6]. They observed a broad P_+-wave as well, but it does not show a resonant phase motion, which seems consistent with the result of the reanalysis of GAMS group.

The Crystal Barrel collaboration reported the observation of the 1^{-+} wave in the different reaction[21]. They studied $\overline{p}n$ annihilation channel

$$\overline{p}d \to \pi^-\pi^0\eta p,$$

and observed that the P-wave of both of $\eta\pi$ charge combinations interfere with ρ^- and $a_2(1320)$ states on the Dalitz plot (Fig. 2.5). This suggests the resonant character of the $\eta\pi$ P-wave and the fit gives the resonance parameters of mass ~ 1.4 GeV/c^2 and width ~ 0.31 GeV/c^2, which is in good agreement with the VES and E852 results.

$\eta'\pi$ channel

The analysis of the $\eta'\pi$ channel is almost the same as that of the $\eta\pi$ channel. The P-wave angular momentum between η' and π becomes a sign of the 1^{-+} exotic quantum number.

VES observed a P_+-wave with the largest intensity in the $\eta'\pi^-$ channel of the π^-p diffractive reaction: the same experiment as the $\eta\pi$ data were taken[19] (Fig. 2.3(b)). They compared the matrix element squared of the P_+-waves of the $\eta'\pi^-$ and $\eta\pi^-$ channel, which are the intensities divided by the two-body phase space and the

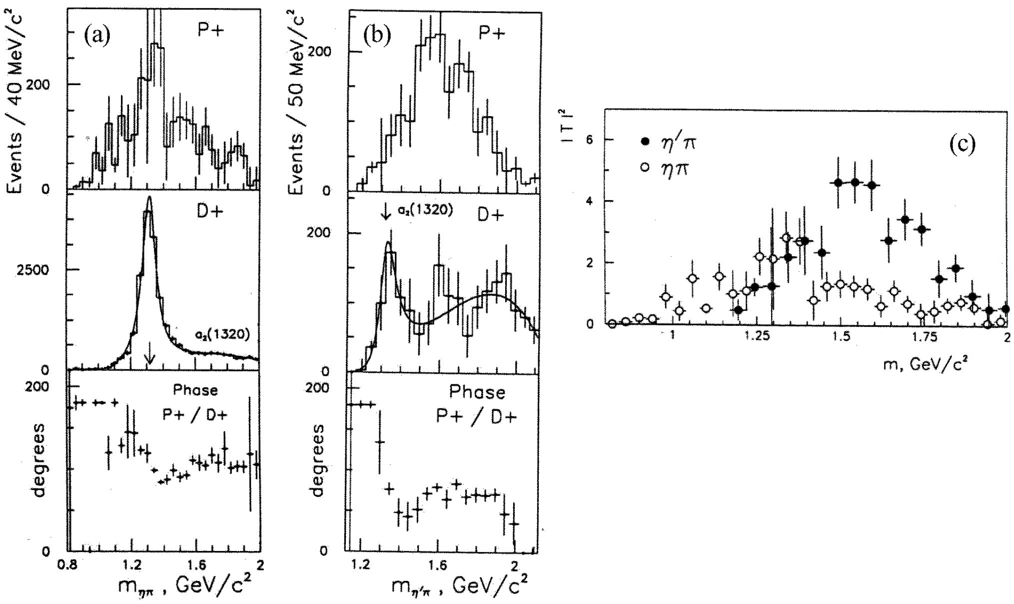

Figure 2.3: VES results[19]. (a) $\eta\pi^-$ partial wave intensities. (b) $\eta'\pi^-$ partial wave intensities. (c) Comparing the matrix element squared of the P_+-waves in the $\eta\pi^-$ and $\eta'\pi^-$ channels.

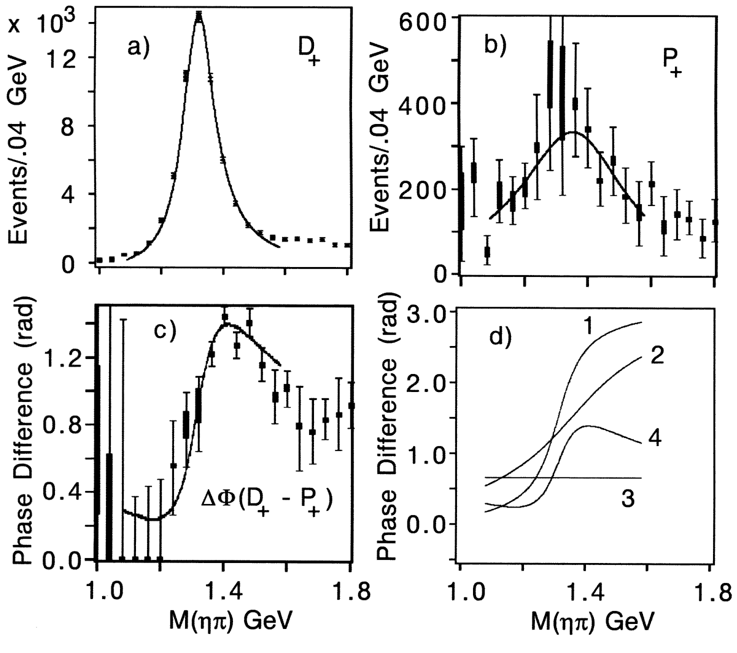

Figure 2.4: E852 $\eta\pi^-$ partial wave intensities[20]. The lines in d) correspond to 1. the fitted D_+ Breit-Wigner phase, 2. the fitted P_+ Breit-Wigner phase, 3. the fitted $D_+ - P_+$ relative production phase and 4. the overall $D_+ - P_+$ phase difference as shown in c) but with a different scale.

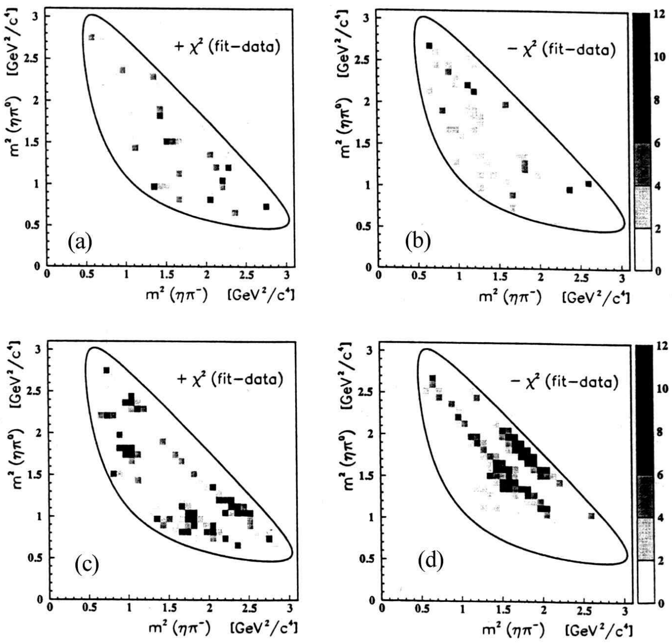

Figure 2.5: Distributions of the deviations of the individual terms χ_i^2 in the fitting: $\chi^2 = \sum_{\text{cells}}(N_i^{\text{exp}} - N_i^{\text{theor}})^2/\sigma_i^2$[21]. (a) The fit exceeds the data and (b) the data exceeds the fit. (c),(d) Same as (a) and (b), respectively, but a fit does not includes the $\eta\pi$ P-wave.

branching ratios of η and η' decays (Fig. 2.3(c)). They claimed that the significant excess of the P_+-wave in the $\eta'\pi^-$ channel with respect to the $\eta\pi^-$ channel is consistent with the theoretical prediction for the hybrid state[22], which is discussed later. A Breit-Wigner fit to the bump of the P_+-wave gives mass ~ 1.6 GeV$/c^2$ and width ~ 0.55 GeV$/c^2$[6].

E852 also reported a dominant P_+-wave in the $\eta'\pi^-$ system as a preliminary result[6]. The data are very similar to the VES result in the case of the $\eta\pi^-$ channel.

$\rho\pi$ channel

ρ meson has $I^G(J^P) = 1^+(1^-)$, hence $J^{PC} = 1^{-+}$ can be coupled by the P-wave angular momentum and $I = 1$ coupling of the $\rho\pi$ system. The charged combinations such as $\rho^0\pi^\pm$ or $\rho^\pm\pi^0$ must have $I = 1$ and thus the P-wave of them leads to 1^{-+}, though other quantum numbers such as $J^{PC} = 0^{-+}, 2^{-+}$ can also be coupled.

VES[23] and E852[6] reported the observation of the 1^{-+} wave in the $\pi^+\pi^-\pi^-$ channel of the same experiments as their $\eta\pi^-$ and $\eta'\pi^-$ data were taken. E852 claimed that the 1^{-+} wave shows a significant phase motion relative to other major resonant waves and suggested that this state is a resonance. A fit to the 1^{-+} wave gives mass ~ 1.6 GeV$/c^2$ and width ~ 0.17 GeV$/c^2$[6]. E852 also observed the 1^{-+} wave in the $\pi^-\pi^0\pi^0$ system in the same experiment[6]. The VES result shows the similar 1^{-+} wave as that of E852. At first VES claimed that the 1^{-+} wave is a resonance with mass 1.62 GeV/c^2 and width ~ 0.2 GeV/c^2[23] but recently pointed out that their result is model dependent: the resonance-like P-wave structure at ~ 1.6 GeV/c^2 disappears in a different reaction model used in the PWA. The bump could be seen if the full coherence of the decay channel with the same J^P is assumed in the reaction while it disappeared if additional parameters were added and the interference of the largest wave with the other waves with the same J^{PC} is arbitrary determined. Moreover, they reported that the growth of 1^{-+} wave around ~ 1.6 GeV/c^2 was observed by rejection of some minor waves from the PWA. The former caution appears not to irrelevant to the result of E852, since full coherence of the decay channel with the same J^{PC} is usually assumed in order to reduce the number of free parameters in the PWA.

The intensity of the 1^{-+} wave in the $\pi^+\pi^-\pi^-$ channel is relatively large compared with those of the $\eta\pi$ and $\eta'\pi$ channels, but a special care will be needed for the analysis of this channel[2].

$f_1(1285)\pi$ channel

Searches for the 1^{-+} state in the $f_1(1285)\pi$ channel have been strongly motivated by a theoretical prediction and the hybrid state in this channel is the main interest of this thesis. The flux tube model[11, 12, 13, 14] predicts the dominant decay of the 1^{-+} hybrid states into the $f_1(1285)\pi$ and $b_1(1235)\pi$ channel. However, the $f_1(1285)\pi$ channel is preferred one for the data analysis because $f_1(1285)$ has a narrower width and the final system of its decay is relatively simple [3], compared with the case of $b_1(1235)$. $f_1(1285)$ has $I^G(J^{PC}) = 0^+(1^{++})$ and therefore the $f_1(1285)\pi$ system with the S-wave angular momentum is coupled uniquely into the $J^{PC} = 1^{-+}$ quantum number.

Currently three experiments have reported their searches for the 1^{-+} state in the $f_1(1285)\pi$ channel. The first report was by VES[23], who analyzed the $f_1(1285)\pi$ channel of the same experiment as the $\eta\pi^-$, $\eta'\pi^-$ and $\rho\pi$ data were taken. They carried out the PWA for 1.02×10^5 $\eta\pi^+\pi^-\pi^-$ events, and found the 1^{++} dominant wave together with the small but significant 1^{-+} wave (Fig. 2.6). Much clearer evidence for the 1^{-+} state was reported by BNL E818 collaboration[24], who studied the reaction

$$\pi^- p \to f_1(1285)\pi^- p,\ f_1(1285) \to K^+\overline{K}^0\pi^-$$

at 18 GeV/c incident beam momentum. The 1^{-+} signal in their PWA is rather substantial, of the ratio at 45 ± 6 % to total of 747 events. Figure 2.7 presents the

[2]All data of the $\pi^+\pi^-\pi^-$ and $\pi^-\pi^0\pi^0$ channels were presented at XXVI International Conference on High Energy Physics[23] and Hadron 97[6], but none of them has not been published yet.

[3]The major decay mode of $f_1(1285)$ is: $f_1(1285) \to a_0(980)\pi, a_0(980) \to \eta\pi$, where the final system consists of three particles, while that of $b_1(1235)$ is: $b_1(1235) \to \omega\pi, \omega \to \pi^+\pi^-\pi^0$, where the final system consists of four pions.

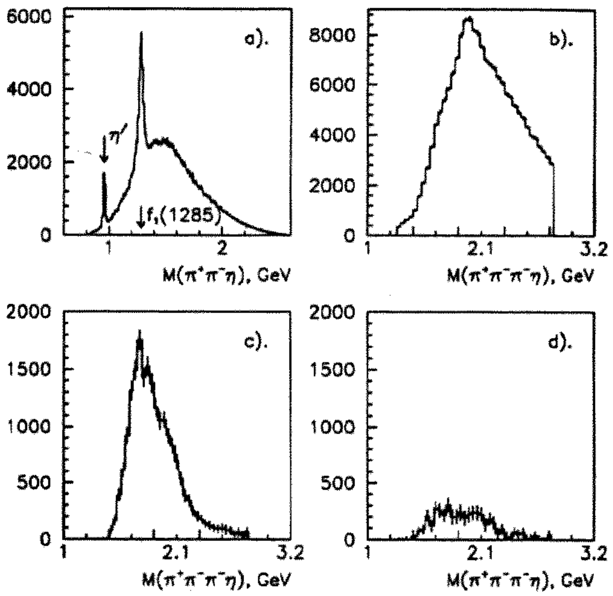

Figure 2.6: Result of VES experiment[23]. (a) Mass spectrum of $\eta\pi^+\pi^-$ subsystem. (b) Total mass spectrum of $\eta\pi^+\pi^-\pi^-$. (c) $J^{PC}M^{\epsilon} = 1^{++}0^+$ and (d) $1^{-+}1^+$ intensities.

result of PWA by E818. The observed states in their analysis are J^{PC}[isobar]]M^{ϵ} = $1^{++}[f_1(1285)]0^+$, $1^{-+}[f_1(1285)$ and $\eta(1295)]1^+$, $2^{++}[f_1(1285)]1^+$, where M and ϵ represents the absolute value of the spin projection and the naturality of the exchanged particle, respectively. The 1^{++} state is consistent with the VES result and they have suggested it as a radial excitation of the $a_1(1260)$. The 1^{-+} state is broad and they have claimed it is a compound system: a state at 1.7 GeV/c^2 decaying to both $f_1(1285)\pi$ and $\eta(1295)\pi$, and that at 2.0 GeV/c^2 decaying only via $f_1(1285)\pi$ channel. The rapid phase motion is observed only in the higher part of the 1^{-+} state and this indicates only the $f_1(1285)\pi$ channel at 2.0 GeV/c^2 is significant for the 1^{-+} state. Their conclusions are, however, based on limited statistics.

The latest report was from E852, who analyzed the $f_1(1285)\pi$ channel of the same experiment as the $\eta\pi^-$, $\eta'\pi^-$ and $\rho\pi$ data were taken. They obtained about 12000 events as $f_1(1285)\pi$ candidates. Their PWA results are shown in Fig. 2.8, which appear to be very consistent with those of E818 except the assignment of the 2^{-+} wave. They have given further suggestions as follows:

- The small phase motion between the 1^{++} and 1^{-+} waves indicates the two waves are either resonant or non-resonant together.
- The strong phase motion of the 2^{-+} wave relative to the other two waves indicates one more resonance in the 2^{-+} wave than in the 1^{++} and 1^{-+} waves.
- Therefore, this analysis suggests either a single resonance (2^{-+}) or four resonances (one 1^{++}, one 1^{-+} and two 2^{-+}) interpretation.

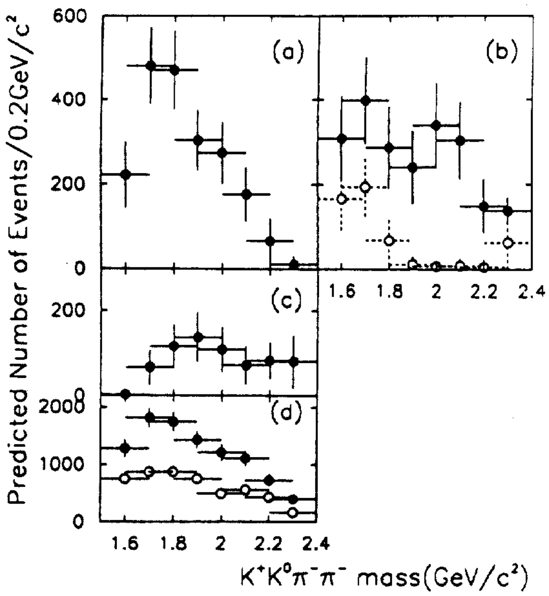

Figure 2.7: Result of E818 experiment[24]. (a) $J^{PC}M^{\epsilon} = 1^{++}0^{+}$ intensity. (b) $1^{-+}1^{+}$ intensity with combined $f_1(1285)\pi$ and $\eta(1295)\pi$ decay modes. The dotted spectrum shows $\eta(1295)\pi$ wave only. (c) $2^{++}1^{+}$ intensity. (d) All partial waves included in the fit. The open circles in the plot show the background.

	1^{++} (1.7 GeV/c^2)	1^{-+} (1.6–2.2 GeV/c^2)	2^{-+} (1.6–2.1 GeV/c^2)
VES	dominant	seen	–
E818	dominant	$\eta(1295)\pi + f_1(1285)\pi$	2^{++}
E852	dominant	$f_1(1285)\pi$	one or two states

Table 2.2: List of experimental results for $f_1(1285)\pi$ channel[23, 24, 25].

The results of these three experiments are listed in Table 2.2. In summary, the $f_1(1285)\pi$ channel is considered to mainly consist of three components—1^{++}, 1^{-+} and 2^{-+} (or 2^{++}) waves. The 1^{++} wave dominates in the $f_1(1285)\pi$ channel and its appearance in three experiments are very consistent. The 1^{++} intensity can be well represented by a Breit-Wigner form and its mass and width are found to be 1.7 and 0.4 GeV/c^2 respectively[25]. The 2^{-+} (2^{++}) wave is relatively small and there is a disagreement between E818 and E852 on its assignment. This disagreement is possibly due to a misassignment of either result caused by statistical fluctuations of its small intensity. The exotic 1^{-+} wave has been observed in all three experiments. The 1^{-+} intensity is not small in the E818 and E852 results but there are some differences between two results compared with the excellent agreement of the 1^{++} case.

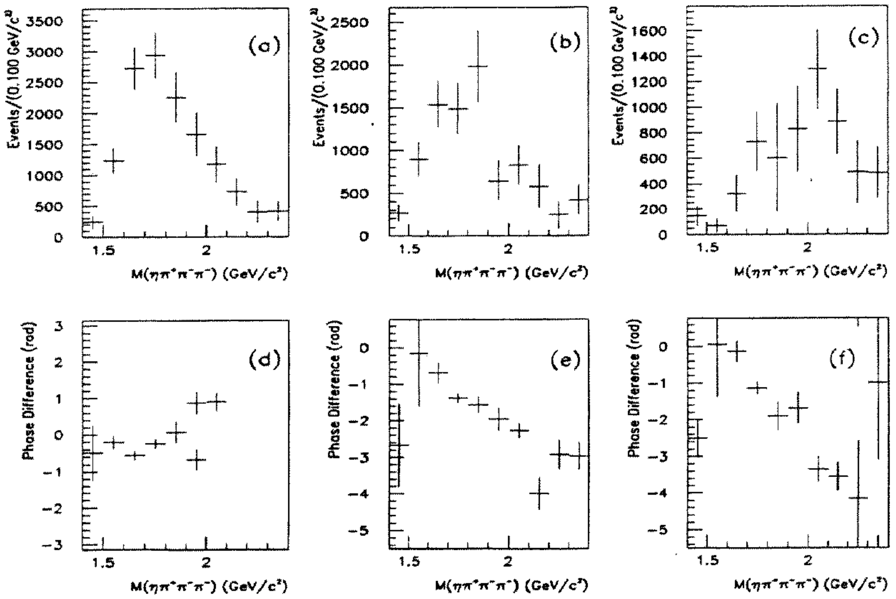

Figure 2.8: Result of E852 experiment[25]. (a) $J^{PC}M^{\epsilon} = 1^{++}0^{+}$ $f_1(1285)\pi^-$ intensity. (b) $1^{-+}1^{+}$ $f_1(1285)\pi^-$ intensity. (c) $2^{-+}1^{+}$ $f_1(1285)\pi^-$ intensity. (d) $[\phi_{1^{++}0^{+}} - \phi_{1^{-+}1^{+}}]$. (e) $[\phi_{1^{++}0^{+}} - \phi_{2^{-+}0^{+}}]$. (f) $[\phi_{1^{-+}1^{+}} - \phi_{2^{-+}0^{+}}]$.

other channels

The GAMS group reported the observation of the 1^{-+} candidate in the $\eta\eta'$ channel of the $\pi^- p$ charge exchange reaction with 38 GeV/c incident beam momentum[26]. They observed a peak with mass $\sim$ 1.9 GeV/c^2 and rather narrow width $\sim$ 0.1 GeV/c^2. Because of the low statistics, they could not carry out PWA and thus the quantum number of this peak was not determined. The possible quantum numbers are $J^{PC} = 0^{++}, 1^{-+}$ or 2^{++} obtained from those of η and η' (0^{-+}). The possibility of higher spin states are disfavored by the behaviour of the angular distribution between η and η': the angular distribution becomes more and more isotropic when $|t|$ increases, where t denotes the momentum transfer squared[26]. This state has not observed in the $\pi\pi$, $\eta\eta$ nor $K\overline{K}$ channels and they suggested that such a decay property could indicate a large gluonic component and this state could be considered as a hybrid if $J^{PC} = 1^{-+}$ or a glueball if $J^{PC} = 0^{++}$ or 2^{++}.

The $b_1(1235)\pi$ channel is another channel which the flux tube model predicts as a dominant decay mode of the hybrid state. However, the final system of its major decay mode consists of 5 pions (see footnote on page 13). Thus the analysis of this channel is much more complicated than that of the $f_1(1285)\pi$ channel due to the large multiplicity of combinations of pions. VES and E852 reported that their analysis of the $b_1(1235)\pi$ channel is now going on[6].

2.2 Interpretation of 1^{-+} exotics

The $J^{PC} = 1^{-+}$ quantum number can be accessed by the glueball, hybrid and multiquark state (baglike or dimeson). For the 1^{-+} state in the $\eta\pi$, $\eta'\pi$, $\rho\pi$ (charged) and $f_1(1285)\pi$ systems, the glueball interpretation can be ruled out since those system have $I = 1$ which cannot be coupled by gluons only. Moreover, a recent lattice calculation presented that mass of the glueball with $J^{PC} = 1^{-+}$ is higher than 3 GeV/c^2[4]. Therefore the 1^{-+} state which we are interested in at present is a candidate for either of the hybrid or multiquark state.

The present analysis has been strongly motivated by the prediction of the flux tube model for the hybrid state[12, 14]. This model is based on the strong coupling expansion of the lattice QCD Hamiltonian. In the semiclassical explanation of the flux tube model, $Q\overline{Q}$ pair is connected with the flux tube of colored fields and the gluonic degree of freedom of the hybrid state is represented as the excitation of the flux tube along the relative coordinate $\vec{r}_A$ of the $Q-\overline{Q}$ and the transverse coordinate of the flux tube $\vec{y}_\perp \equiv -(\vec{y}\times\hat{r}_A)\times\hat{r}_A$, where $\vec{y}$ denotes the relative coordinate between the center of $Q\overline{Q}$ and the flux tube (Fig. 2.9). Decay occurs when the flux tube breaks at any point along its length, producing a $q\overline{q}$ pair in a relative $J^{PC} = 0^{++}$ state. The distribution of the flux tube is more structured for the hybrid state due to its excitation than that of the ordinary meson where the flux tube is in its ground state, and this gives the characteristic property of decay of the hybrid meson[14]. In the case of final states consisting of two ground state mesons "$(L = 0) + (L = 0)$" (L:the angular momentum of $q\overline{Q}$ or $\overline{q}Q$), for example, $\pi\pi$, $\eta\pi$, $\rho\pi, \ldots$, the angular momentum of the excited flux tube cannot be absorbed anywhere, thus the decay of the hybrid state into these final states would be strongly suppressed[12]. On the other hand, the decay of the hybrid state into "$(L = 1) + (L = 0)$" meson pairs, such as $f_1(1285)$ and $b_1(1235)\pi$, is expected to be favored. F.E.Close and P.R.Page estimated partial width[14] for the decay of the 1^{-+} state at mass of 2.0 GeV/c^2 as follows:

$$f_1\pi : b_1\pi : \rho\pi : \eta\pi : \eta'\pi = 60 : 170 : 5-20 : 0-10 : 0-10 \text{ (MeV)}. \tag{2.3}$$

According to the flux tube model, the 1^{-+} signal in the $f_1(1285)\pi$ channel observed by VES, E818 and E852 is the most probable candidate for the hybrid state. However, any of three experiments has not given a firm conclusion that the 1^{-+} wave is a resonant state. This is mainly due to the absence of other well established states in the $f_1(1285)\pi$ channel, which makes the determination of the phase motion of the 1^{-+} wave difficult. For example, in the $\eta\pi$ channel, the phase motion of the 1^{-+} wave can be investigated by seeing its relative variation to that of the well established $a_2(1320)$ state.

On the other hand, the assignment of the 1^{-+} state at ~ 1.4 GeV/c^2 in the $\eta\pi^-$ channel observed by KEK, VES, E852 and Crystal Barrel as the hybrid state is not favored by the flux tube model. A recent lattice calculation for the hybrid mass, which gives the mass around 2 GeV/c^2[27], is not favor for the $\eta\pi^-$ 1^{-+} wave being

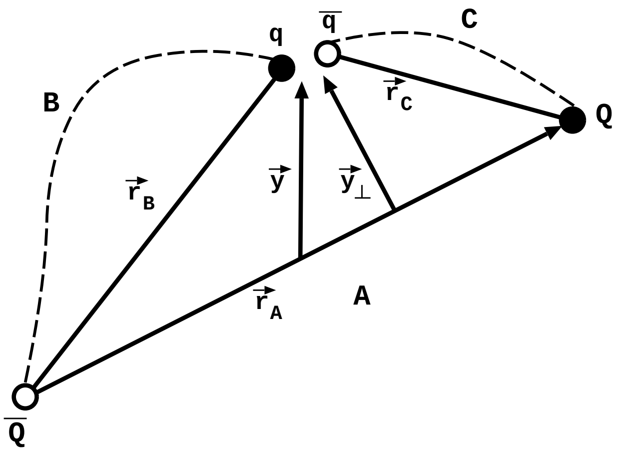

Figure 2.9: Semiclassical picture of the flux tube model for the meson decay: $A(Q\overline{Q}) \to B(q\overline{Q})C(\overline{q}Q)$.

the hybrid state, neither. Nevertheless, the resonance-like phase motion of the 1^{-+} wave is observed by all the experiments. One interpretation for this state is that it is a multiquark state, but it cannot be explained why the resonant phase motion of the 1^{-+} wave is not observed in the $\eta\pi^0$ channel. This state have $I = 1$ and thus it must be observed in both of the $\eta\pi^-$ and $\eta\pi^0$ channels. A.Donnachie and P.R.Page estimated a contribution of another interpretation[28]: the $\eta\pi$ 1^{-+} resonance may be created from the $b_1(1235)\pi$ channel through the final state interaction, which is illustrated in Fig. 2.10, and the interference with the Deck background will make the resonance-like peak at ~ 1.4 GeV$/c^2$. The Deck background is a broad low mass enhancement produced for a particle pair system in three particle final state[29]. They assume that the 1^{-+} state at 1.6 GeV$/c^2$ observed in the $\eta'\pi^-$ and $\rho\pi$ channel have the $b_1(1235)\pi$ decay mode. They obtained the significant $\eta\pi$ partial width from the assumed $b_1(1235)\pi$ channel through the final state interaction and found that the interference with the Deck background can shift the peak down from 1.6 to 1.4 GeV$/c^2$.

The 1^{-+} waves observed at ~ 1.6 GeV$/c^2$ in the $\eta'\pi^-$ and $\rho\pi$ channel look very similar each other. Thus A.Donnachie and P.R.Page assumed that these 1^{-+} waves arise from the same origin and are the hybrid state. This assumption can explain the resonance-like behavior of the 1^{-+} wave in the $\eta\pi$ channel as described above. However, the flux tube model predicts that the decay of the hybrid state into the $\eta'\pi$ and $\rho\pi$ channels is strongly suppressed relative to the $f_1(1285)\pi$ channel. This means that the strong signal of 1^{-+} wave must be observed at ~ 1.6 GeV$/c^2$ in the $f_1(1285)\pi$ channel but the experimental results show the 1^{-+} intensity of the $f_1(1285)\pi$ channel peaks at higher mass ~ 2.0 GeV$/c^2$. It appears difficult to regard the 1^{-+} waves of the $f_1(1285)\pi$ and $\eta'\pi^-/\rho\pi$ channel as an identical one. Moreover, the 1^{-+} wave in the $\rho\pi$ has not confirmed yet due to the ambiguity of the analysis as mentioned before.

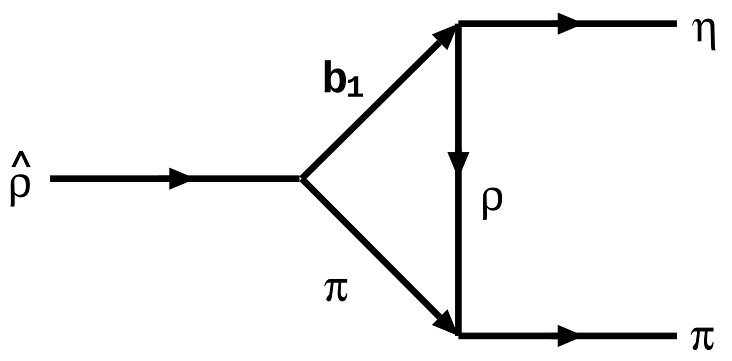

Figure 2.10: Decay of $\hat{\rho}$ to $\eta\pi$ through the final state interaction.

Apart from the flux tube prediction, the larger intensity of the $\eta'\pi$ 1^{-+} wave relative to that of the $\eta\pi$ channel is consistent with the prediction for hybrid systems. In the lowest order nonvanishing diagram for the hybrid $\to \eta\pi(\eta'\pi)$ decay, the $q\overline{q}$ pair will be created by the gluon which becomes a color singlet by exchanging additional gluons, and the $q\overline{q}$ pair with the remaining flavor singlet will then turn into an $\eta(\eta')$ through the flavor singlet component[22]:

$$|uG\overline{d}\rangle \to |u(\overline{q}q)_8\overline{d}\rangle \to |(q\overline{q})_1(u\overline{d})_1\rangle \to |M_{q\overline{q}}; M_{u\overline{d}}\rangle,$$

where G denotes the gluon, the subscript 1 and 8 denote the color singlet and octet, respectively, and M denotes the meson state. Since the η' has a large $SU(3)$ flavor singlet component, the decay into the $\eta'\pi$ channel is expected to be dominant.

2.3 Summary

The evidence for the existence of the 1^{-+} state has been reported in various channels, but none of them has been classified as the exotic state without any inconsistency.

The flux tube model has been successful in a prediction of widths and decay modes of some well-known hadrons. Its applicability for the hybrid state can be tested by investigating its prediction of the dominant observation of the 1^{-+} hybrid state in the $f_1(1285)\pi$ and $b_1(1235)\pi$ channels. Unfortunately, the analysis of the $f_1(1285)\pi$ and $b_1(1235)\pi$ are not so easy as those of the $\eta\pi$ and $\eta'\pi$, because the well-established state does not exist in these channels, which are useful for the check of the validness of the analysis or as the reference of the phase variation. However, since the successful application of the flux tube model for the hybrid state leads to the confirmation of the hybrid state, it is clearly worth trying.

All previous observations of the 1^{-+} wave in the $f_1(1285)\pi$ channel have been done through the π^-p diffractive reaction. From the view of the flux tube model, the contribution of "valence gluon" to the production of hybrid states can not be understood directly because the hybrid structure is expressed as an excitation of the flux tube connecting quarks in this model. However, in glueball searches it is thought to be important to analyse channels where the converse is the case, that is, it is important to search glueballs in "gluon rich" channel. This has been supported so far by many observations of glueball candidates in the 'gluon rich' processes presented in Fig. 1.1. Hence it is natural to extend this motivation to the case of hybrid states. The WA102 experiment is designed to observe the central production process, where Pomeron-Pomeron or Pomeron-Reggeon collisions are believed to produce "gluon rich" central system. Therefore an analysis of the centrally produced $f_1(1285)\pi$ system is of much interest.

Chapter 3

WA102 experiment

The WA102 experimental setup is optimized for the exclusive measurement of the pp central collision reaction

$$pp \rightarrow p_f(X^0)p_s, \tag{3.1}$$

at 450 GeV/c incident proton momentum, where the subscripts f and s denote the fastest and slowest particle in the laboratory frame, respectively, and X^0 represents the central system produced in this reaction. Figure 3.1 presents the pictorial diagram of the required reaction. Both protons exchange particles in the reaction. Since the Reggeon-Pomeron or Pomeron-Pomeron exchanges, which is the aimed reactions in the present experiment, is expected to become dominant relatively to the Reggeon-Reggeon exchange as four momentum transfered at each vertex becomes smaller[7], the reaction where protons almost preserve their initial momenta through the scattering should be selected. In the laboratory frame this corresponds to the case where the beam proton is scattered into the very forward direction as the fastest particle in the system ($\sim$ 400 GeV/c), while the target proton is recoiled as the slowest particle ($\sim$ 1 GeV/c) in the system.

The central system X^0 immediately decays into several charged and/or neutral particles. The charged particles which have a long lifetime such as $\pi^\pm$ and $K^\pm$ are observed as the medium tracks ($\sim$ 10 GeV) in the laboratory frame. The charged particles which have a short lifetime and the neutral particles decay sequentially and are finally observed as πs, Ks and gammas.

3.1 WA102 experimental setup

3.1.1 Overview of setup

Figures 3.2 and 3.3 present layouts of the WA102 experimental setup of 1995 run and 1996 run, respectively. The feature of the WA102 setup is the assemblage of Omega and GAMS. The Omega spectrometer is a multi-user detector designed for measuring fixed-target interactions that produce many final-state charged particles.

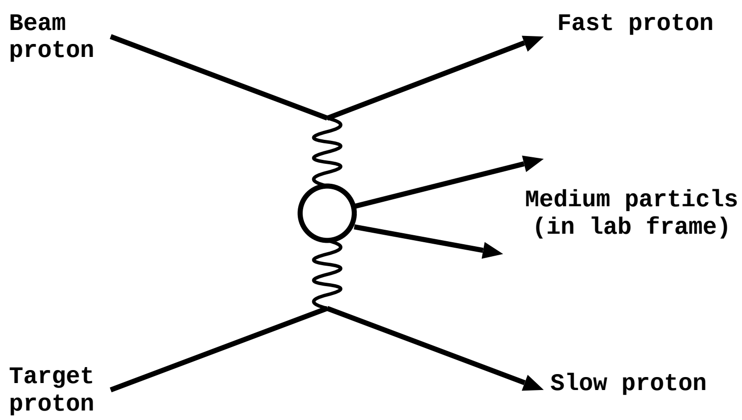

Figure 3.1: Diagram of the pp central collision.

It consists of a superconducting magnet that is capable to produce a central field of up to 1.8 T and sets of MWPC's, drift chambers, μ-strip detectors and trigger scintillation counters. For the WA102 experiment the field was used with 1.35 T to enable to detect the slowest particle with a momentum below the energy of 1 GeV/c. The specification of each detector is summarized in Table 3.1.

GAMS a the hodoscope electromagnetic calorimeter made of lead glass cells. It has good position and energy resolutions for the gamma detection, then is excellent for the measurement of the neutral particles decaying into gammas. By combining Omega and GAMS, it is expected to detect charged and neutral particles simultaneously with a high multiplicity. This is a big advantage to study various decay modes.

The experimental setup of the 1995 run was optimized for the gamma detection by locating GAMS as near to the target as possible, while the setup of the 1996 run was optimized for the measurement of channels including Kaons. In the 1996 run, the Čerenkov counter was installed between the drift chamber and GAMS for particle identification.

What are to be measured in the reaction are the beam proton, fast proton, slow proton and decay products of the central system X^0. Details of the measurement of each particle will be described in the following.

3.1.2 Beam measurement

The beam is a 450 GeV/c proton beam extracted from the CERN SPS through the H1 beam channel. No secondary targets are used, thus the beam is essentially 100% protons. The beam signal is defined before interacting with the target, by using four scintillation counters of S2, S4, V2 and V4 (Fig. 3.4). S2 and S4 are signal counters which are square slabs of side 2.5 and 0.8 cm, respectively. V2 and V4 are veto counters which are also slabs of side 17 cm both, but have a hole of

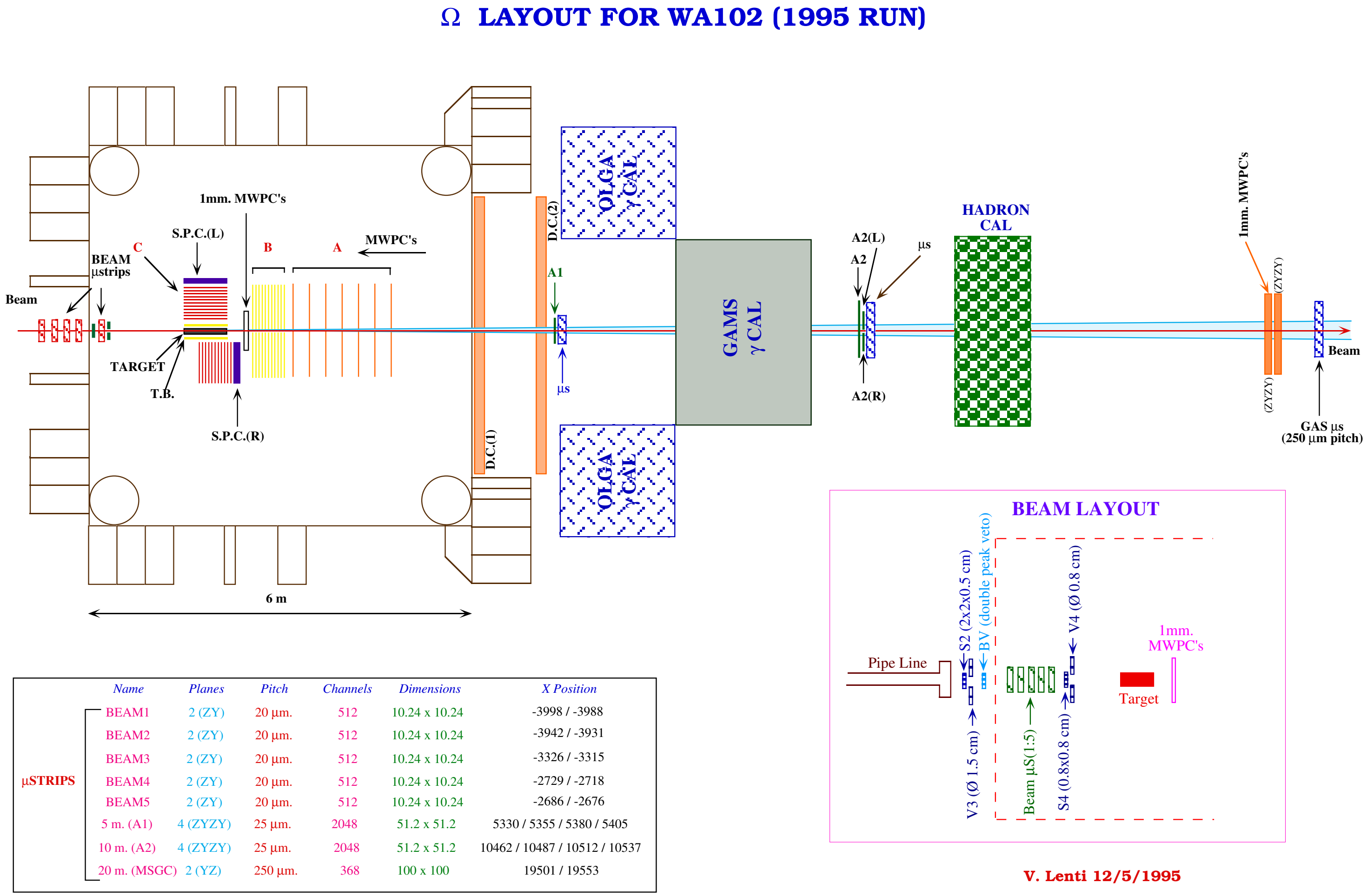

	Name	Planes	Pitch	Channels	Dimensions	X Position
µSTRIPS	BEAM1	2 (ZY)	20 µm.	512	10.24 x 10.24	-3998 / -3988
	BEAM2	2 (ZY)	20 µm.	512	10.24 x 10.24	-3942 / -3931
	BEAM3	2 (ZY)	20 µm.	512	10.24 x 10.24	-3326 / -3315
	BEAM4	2 (ZY)	20 µm.	512	10.24 x 10.24	-2729 / -2718
	BEAM5	2 (ZY)	20 µm.	512	10.24 x 10.24	-2686 / -2676
	5 m. (A1)	4 (ZYZY)	25 µm.	2048	51.2 x 51.2	5330 / 5355 / 5380 / 5405
	10 m. (A2)	4 (ZYZY)	25 µm.	2048	51.2 x 51.2	10462 / 10487 / 10512 / 10537
	20 m. (MSGC)	2 (YZ)	250 µm.	368	100 x 100	19501 / 19553

Figure 3.2: Layout of the WA102 experimental setup of the 1995 run.

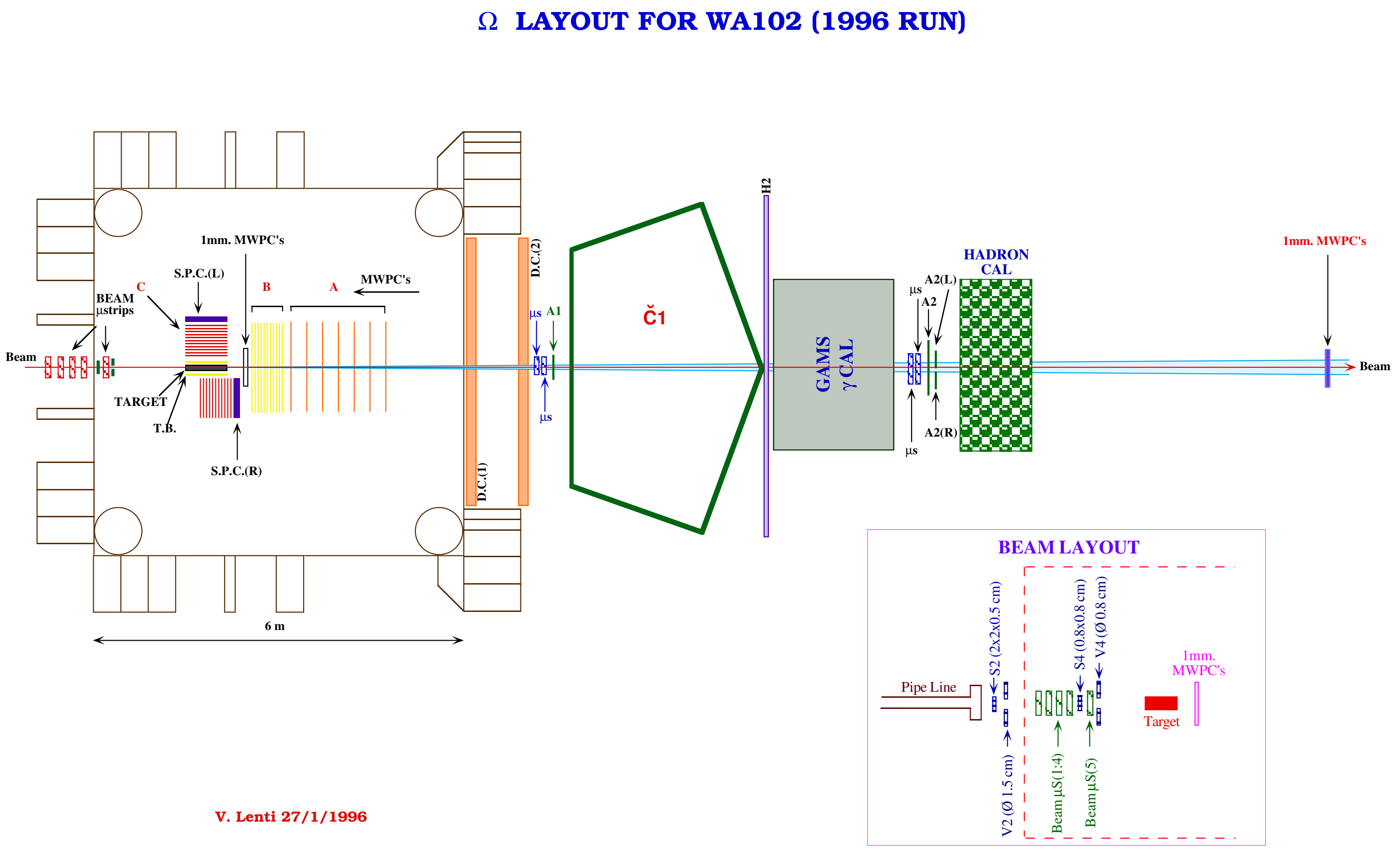

Figure 3.3: Layout of the WA102 experimental setup of the 1996 run.

	Planes	Pitch	Dimensions(cm)	X position (m)
Beam				
Hodoscope	YZY	1 mm	1.8×1.8	$-14.887 \sim -4.439$
μ-strips	ZY $\times$ 5	20 μm	1.024×1.024	$-4.063 \sim -2.843$
Slow				
MWPC(C)	UY(VY) $\times$ 8	2 mm	51×80	-1.360 (left)
				$-1.453 \sim -1.017$ (right)
Fast				
μ-strips	ZYZY	25 μm	5.12×5.12	$5.365 \sim 5.440^*$
μ-strips	ZYZY	25 μm	5.12×5.12	$11.230 \sim 11.305^*$
MWPC	ZYUW $\times$ 2	1 mm	25×25	$19.384 \sim 20.008$
MSGC	YZ	250 μm	10×10	$19.233 \sim 19.615$
Medium track				
MWPC(A)	UYV $\times$ 7	2 mm	150×90	$-0.116 \sim 1.686$
MWPC(B)	UY(VY) $\times$ 8	2 mm	150×90	$-0.748 \sim -0.312$
Drift chamber	YZYZ $\times$ 2	5 cm	315×150	$3.271 \sim 4.499$
Vertex				
MWPC	ZYUW	1 mm	25×25	$-0.808 \sim -0.784$
Target		$60\ \phi \times 600$ mm^3		-1.500

Table 3.1: Specifications of detectors used in the Omega spectrometer. The X,Y,Z axes are of the Omega system, where X axis is along the beam and the origin is the center of the magnetic field. The Y plane is inclined to the vertical in the system and U, V and W planes are inclined at $\pm 10.14°$ and $100.14°$ to the Y plane, respectively. *) Distances of the 1995 run. In the 1996 run μ-strip detectors at ~ 5 m were moved to 1.7 m upstream while ones at ~ 10 m were moved to 0.4 m downstream to install the Čerenkov counter between the drift chamber and GAMS.

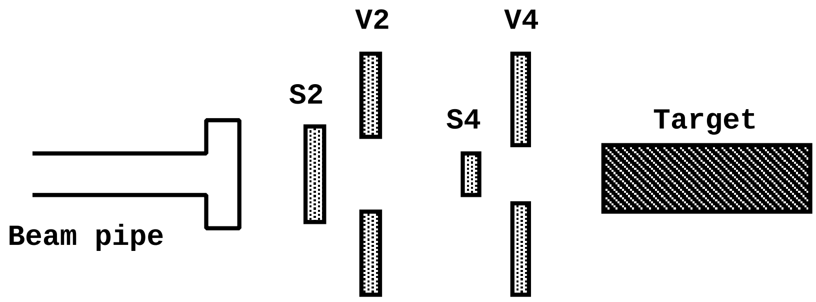

Figure 3.4: Layout of the beam trigger counters.

diameter 1.5 and 0.8 cm, respectively. A beam signal is defined by the condition that both of S2 and S4 are hit but neither V2 nor V4 are. And further, to confirm that only one particle passes the beam trigger and hence interacts with the target, the clean beam (CB) logic is used.

Figure 3.5 presents the CB trigger logic diagram and its timing of signals. The CB coincidence requires a BEAM, S2, S2P and the inverse of S2P where S2P is an extra signal taken from S2. The timing is trimmed so as to coincident in general case, but $\overline{\mathrm{S2P}}$ will have a longer duration if a second particle arrives, in which case the event will be rejected.

The direction of the beam is measured by beam hodoscopes and beam μ-strip detectors. The beam hodoscope consists of 16 scintillation counters of 3 mm width, which are put side by side with 1 mm overlaps each other. The beam μ-strip detectors are five sets of 20 μm pitch silicon strips, where each set consists of Y and Z planes.

3.1.3 Target

The target is a cylinder of liquid hydrogen of 6 cm diameter and 60 cm long, contained in a mylar and aluminium canister. The target is located at 1.5 m up-stream of the center of the Omega magnetic field. It is surrounded by the target box counter used for the slow particle trigger, which is described in the next section.

3.1.4 Slow proton measurement

The slow proton is measured with the set of 2 mm pitch multiwire proportional chamber (labelled as C in Figs. 3.2 and 3.3). The C-chambers are aligned so as for the detector planes to be parallel to the beam direction on the left side of the target and to be normal on the right side. This arrangement is chosen for the maximum acceptance of the slow particle which is bent in the magnetic field as presented in Fig. 3.6.

The slow proton counters on both sides of the target (labelled as SPC(L) and SPC(R)) and the target box counter (labelled as TB) are used to confirm only one

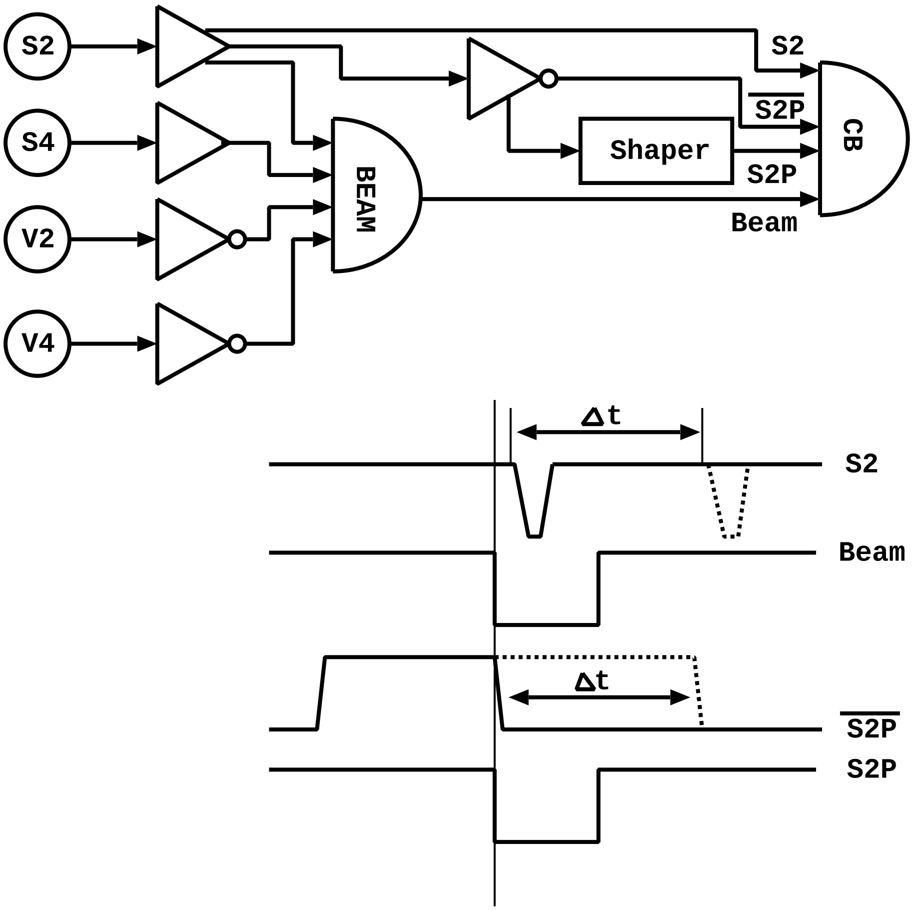

Figure 3.5: Beam trigger logic and timing of signals to define Clean Beam (CB). Events with more than one incident particle were rejected.

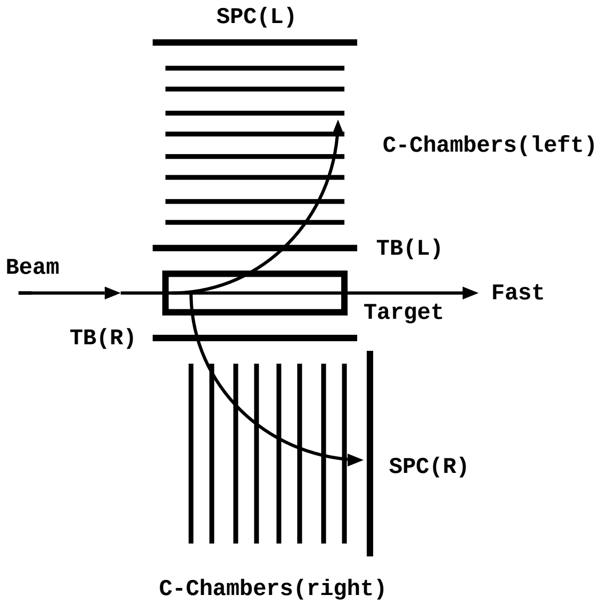

Figure 3.6: Alignment of the C-chambers.

slow particle in the reaction, to reject the target diffraction event which competes with the central collision process (Fig. 3.7). SPC(L) and SPC(R) consist of 14 scintillator slabs of 6 cm width and 1 m active length (SPC(L)) and 7 cm width and 70 cm active length (SPC(R)), respectively. TB is composed of 10 scintillator slabs surrounding the target on four sides, left open at the upstream and the downstream sides of the target in order to let through the beam and forward particles. Only the left side and the right side slabs (labelled TB(L) and TB(R) in Fig. 3.8) are trigger counters, while others are used as veto. The trigger for the slow proton requires a coincidence between a signal from one side of the target box (either TB(L) or TB(R)) and a signal from only one or two slabs in the slow proton counter on the same side. That is, only the coincidence between TB(L) and SPC(L) or TB(R) and SPC(R) are accepted while such as one between TB(L) and SPC(R) or multiple hit to the target box or the slow proton counters are rejected.

The slow proton counters are used also for the particle identification. Figure 3.9 presents a plot of ADC pulse height of SPC(L) versus particle momentum. The upper band labelled p is due to slow protons while the lower one is due to pions. The maximum on the plot corresponds to a proton being stopped in the medium and giving up all of its energy, and the rapid decrease of the ADC amplitude at the low momentum (< 0.35 GeV/c) is due to the energy loss of protons in the target and the target box counter[1]. Protons can be selected by using a software cut on this distribution after the particle momentum is calculated by the charged track reconstruction procedure.

[1]The track reconstruction program TRIDENT takes into account the energy loss of the slow particle during calculating its momentum (see section 3.3.1).

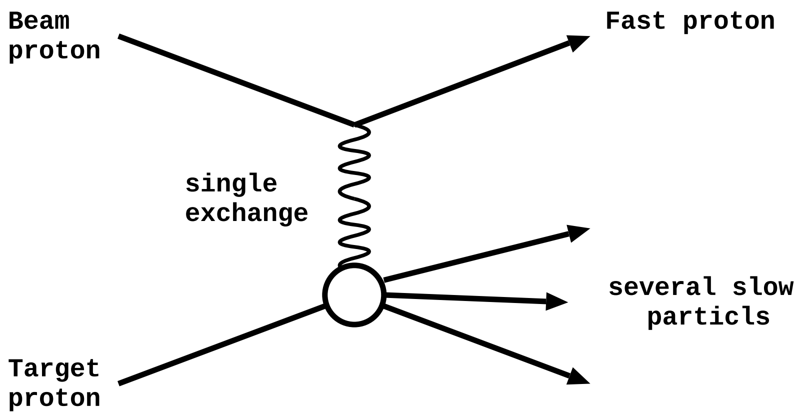

Figure 3.7: Diagram of a typical target diffraction event.

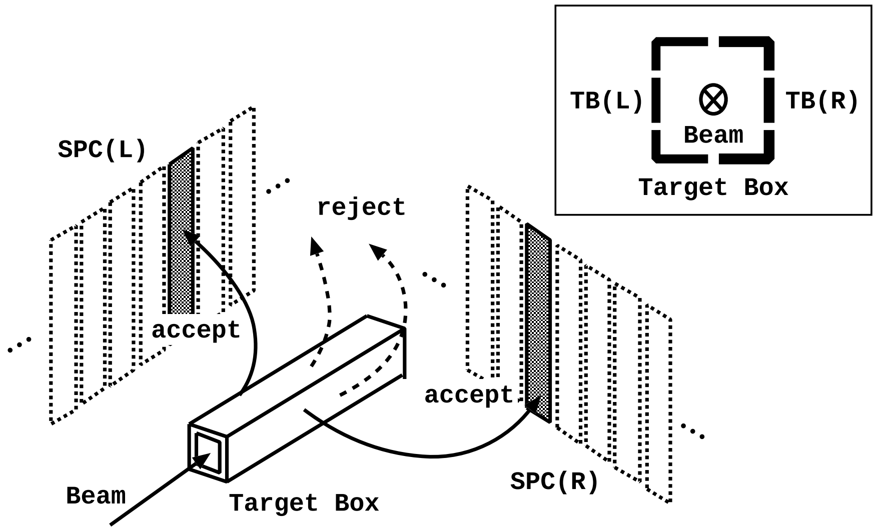

Figure 3.8: Slow proton trigger.

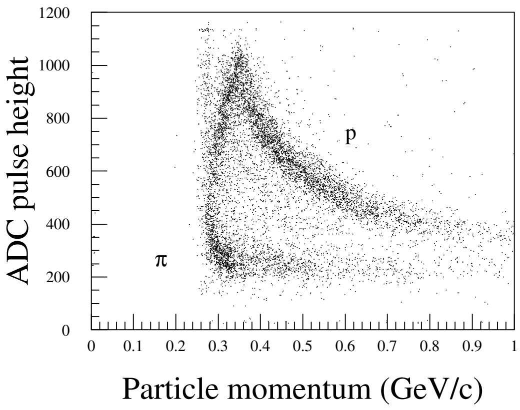

Figure 3.9: ADC pulse height of the slow proton counter versus particle momentum.

3.1.5 Fast proton measurement

The fast proton is measured with the 25 μm pitch μ-strip detectors located at 5 and 10 m downstream of the center of the Omega system, the 1 mm pitch multiwire proportional chambers and the 250 μm pitch μ-strip gas chambers located at 20 m downstream.

For the fast proton trigger a set of scintillation counters, labelled A1, A2, A2(L) and A2(R) in Figs. 3.2 and 3.3, are used. A1 is a square slab of scintillator of side 2.5 cm and A2 is of side 5.0 cm. They are located behind the drift chambers and GAMS, respectively. A2(L) and A2(R) are located immediately behind A2, on the left and right sides of the beam direction, and are used to find the fast track direction (see section 3.1.8).

3.1.6 Medium track measurement

The charged particles with medium momenta in the reaction, produced by the decay of the central system X^0, are measured with the set of 2 mm pitch multiwire proportional chambers (labelled A and B in Figs. 3.2 and 3.3) and the set of the drift chambers with 2.5 cm spacing between the sense and field wire. The drift chambers are located immediately outside the Omega magnetic field. The 1 mm pitch MWPC located at just downstream of the target is used to associate the track found in chambers above and the reaction vertex. This is also in the case of the fast track.

In the 1996 run the Čerenkov counter was installed behind the drift chambers and used for the particle identification.

	GAMS2000	GAMS4000
TYPE-Transparency class	TF1-000	F8-00
PbO(%)	50	45
Density(g/cm^3)	3.85	3.60
Radiation Length X_0(cm)	2.6	2.9
Molière radius(cm)	$\sim$2.5	
Cell Dimension	38 mm $\times$ 38 mm $\times$ 450 mm	
Number of Cells	1535	4092
Matrix: $N_x \times N_y - N_{\rm hole}$	$48 \times 32 - 1$	$64 \times 64 - 4$
Position Resolution, σ_x		
at 25 GeV	1.3 mm	2 mm
at 200 GeV	-	1 mm
Energy Resolution(FWHM)	$0.027 + 0.13/\sqrt{E(\mathrm{GeV})}$	
Mass Resolution for Particles	a few%	
Max. Number of simultaneous γ	10	20

Table 3.2: The main parameters of GAMS calorimeter.

3.1.7 Gamma detection

For the detection of high energy gammas, produced by electromagnetic decay of the neutral particles, are done with the hodoscope electromagnetic calorimeter GAMS. GAMS consists of 64×64 lead-glass counter cells. It has a hole in the center in order to let the beam and fast proton go through. The parameters of the GAMS detector are listed in Table 3.2[2]. Choice of these parameters are described in Ref. [30] and a brief description as for the position and energy resolution is given here.

The position and energy resolution of the hodoscope calorimeter are closely related with the cell dimension of the radiator. The choice of size of a glass was based on the measurements of the electron beams using prototypes[30]. Figure 3.10(a) presents the accuracy of the coordinate measurements as a function of the cell size, obtained by comparing the evaluated coordinate with the measured value by a scintillation hodoscope of ± 0.35 mm precision. This dependency can be represented well by an exponential function, and the accuracy is almost independent of the electron energy. Figure 3.10(b) presents the energy resolution as a function of the radiator length. The discrepancy from the 'ideal' counters, which have a full transparency, at the large l is due to the light absorption in the glass. From these data the transverse dimension d = 38 mm and the length l = 45 cm have been chosen. This transverse

[2]The GAMS project has been performing experiments using two hodoscope spectrometers, GAMS2000 at IHEP (Protovino) and GAMS4000 at CERN. GAMS4000 is of the present experiment. Table 3.2 presents the parameters of both detectors.

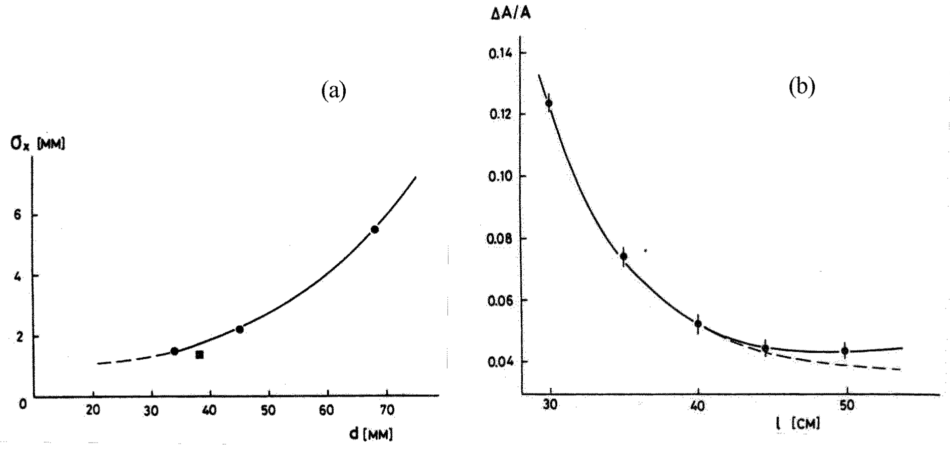

Figure 3.10: Correlation between the size of the radiator and the obtained position and energy resolution[30]. (a) Accuracy of the coordinate measurements σ_x as a function of the cell size d at $E_e = 25$ GeV. The circles are measured values of prototypes and the square is of GAMS. Dependency is represented by exponential function (solid line). (b) Energy resolution (FWHM) as a function of the radiator length l at $E_e = 26$ GeV. A is the sum of amplitudes. The solid curve follows the experimental points and the dashed curve shows the ideal counters with a full transparency.

size allows two gammas to be distinguished if they are separated by $l_{\gamma\gamma} \geq 3$ cm by using the electron shower profile, as described later, and the length enables one to measure gammas with energies up to a few hundred GeV.

In the 1995 run the additional electromagnetic calorimeter OLGA was installed at both sides of GAMS in order to gain the acceptance of the gamma detection. OLGA is composed with 6×19 lead glass blocks on each side, where each block is size of $14\phi \times 47$ cm^3. In practice, however, since an enough acceptance of the gamma detection has been achieved only with GAMS and it is difficult to integrate data from GAMS and OLGA due to different qualities of data, OLGA was removed from the setup in the 1996 run, and data from OLGA has not been used in the present analysis.

In both of the 1995 and 1996 runs, the hadron calorimeter HC240[31] was installed behind GAMS. HC240 consists of 240 total absorption counters, where each counter is composed with thirty-six 25 mm thick steel plates interleaved with 5 mm thick scintillator sheets. HC240 can be used as anticoincidence to exclude the hadronic event on GAMS. It is necessary to reject such events, because not only the gammas from the decay of the central system X^0 but also the medium tracks from the same decay might impact on GAMS and be observed as if they were extra gammas. However, by extrapolating the track observed in the tracking chambers (such as A, B and drift chambers) and looking for the shower cluster on GAMS associated with the impact point predicted by this extrapolation, these events can be removed very successfully (see section 4.1). Then the information from HC240 is not used in the present analysis.

3.1.8 Experimental trigger

To observe the central collision the signal from the clean beam trigger (described in section 3.1.2), slow proton counter (section 3.1.4) and fast proton counter (section 3.1.5) are used as elements of the overall experimental trigger.

Since the *pp* elastic scattering process dominates the central collision process, as the first stage the trigger elements are combined so as to reject the elastic scattering. This is achieved by classifying the event with the combinations of the trigger element as follows:

LL
RR
LR or RL with GAMS

The first letter of the class assignments denotes which SPC was triggered and the second letter shows which of A2(L) and A2(R) was fired. All of the condition classes above require the clean beam signal. In the elastic scattering the two outgoing protons travels in opposite directions each other, then it can be rejected by LL or RR. The third class allows the fast and slow particles travel in opposite directions but requires a signal from GAMS, which ensures the production of the central system.

Then as the second stage, multiplicities from the wire chambers are used in order to do further checks on an event. The two specific planes in the C-chambers are checked and required that only one or two wires must be fired per plane to increase track reconstruction efficiency significantly. Furthermore, multiplicity of the A3 chamber (the third set from the target in the A-chamber series) is used for the trigger of events where the central system decays only into charged particles, such as $X^0 \to \pi^+\pi^-$. These events are rejected by the first step triggers.

After an event has been classified according to one of the above criteria, the chamber information and the information from the μ-strip detectors are read out and stored.

3.2 Event statistics

The intensity of the primary beam from the CERN SPS H1 beam channel is 1.7×10^{11} protons/spill, which are induced with the duration of 2.6 sec through the 14.4 sec cycles. The beam intensity is reduced by an absorber to 2×10^7 protons/spill, and then kept to $5 \sim 6 \times 10^6$ protons/spill at the S2 counter by using collimators. This intensity leads to the experimental trigger of ~ 900 events/burst.

In the 1995 run 200×10^6 events were recorded from the 90 days of beam time, while 300×10^6 events were from the 95 days in the 1996 run.

3.3 Event reconstruction

3.3.1 Reconstruction of charged track

For the reconstruction of the charged tracks, which are the beam, slow, fast and medium tracks, the program TRIDENT was used. TRIDENT is a wide use program for experiments using the Omega spectrometer. The modified version of TRIDENT for the WA102 experimental setup was used in the present analysis. The details of TRIDENT is described in Ref. [32]. Only essential points are described below.

TRIDENT attempts to reconstruct events by track recognition, momentum calculation and the production of fits to reaction vertices. At first the program looks for the detector points as candidates of tracks, using the center of the target as an approximation of the reaction vertex. Each track (the beam, slow, fast and medium) is searched in the appropriate detectors described in the previous sections. Then the intersection of the slow track and beam is calculated. At this time the energy loss in the target box counter is corrected for the slow proton before the calculation. Using this point as an initial value, the primary vertex and all tracks (except the fast track) extrapolated to this point are fitted and particle momenta are calculated. The curve of slow track is correctly reparameterized here, then the energy loss in the target can be calculated and the slow particle momentum is corrected. At the same time, fits of other vertices and their associated tracks are done as well. Finally the fast track is fitted to the primary vertex.

3.3.2 Reconstruction of gamma event

In this section the reconstruction procedure for gamma events is described. More detailed description can be referred in Ref. [33, 34].

Determination of shower coordinate

The shower coordinate X is calculated by correcting the simple estimation of the center of gravity

$$X_c = \frac{\sum_{i=1}^{n} E_i X_i}{\sum_{i=1}^{n} E_i}, \tag{3.2}$$

as

$$X = X_c + \Delta(X_c), \tag{3.3}$$

where E_i and X_i are the energy deposited in cell i and the cell center position, respectively. Coordinates calculated simply with Eq. (3.2) are biased except in the center and the edge of cells, because the distribution of the energy deposit is not uniform along the transverse axis. Figure 3.11 presents the calculated density of the center of gravity position X_c, obtained in a experiment with a wide 10 GeV electron beam. A periodic structure of the density distribution is seen, while the true electron position density is almost uniform because of the wide beam.

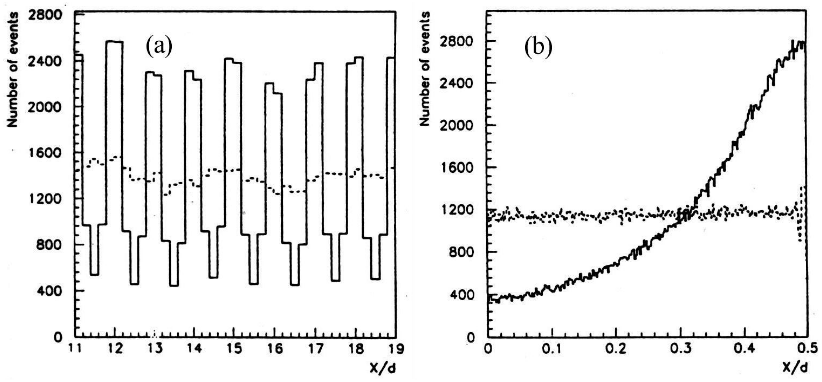

Figure 3.11: (a) Distribution of the center of gravity calculated with Eq. (3.2) (solid line) and the coordinate corrected with Eq. (3.3) (dashed line). (b) Same distributions for the mean values over all cells (half a period). The horizontal axis in each plot is the transverse coordinate X divided by the cell size d. Plots are from Ref. [33].

In good optical contact between the lead glass radiators and photomultipliers, the transverse shower profile is well represented by a double exponential approximation[35]. The optical grease, however, has not been used in the current GAMS experiments (the reason is explained later), hence the shower profile can not be represented by the double exponential slope any longer. Instead the correction function $\Delta(X_c)$ is used, which is of a form as

$$\Delta(X_c) = at(t^4 + bt^2 + c)(t^2 - \frac{1}{4})(t^2 - q), \tag{3.4}$$

where $t = (X_c - X_0)/d$. X_0 is the position of the cell edge nearest to X_c, and d is GAMS cell size. The term $t^2 - \frac{1}{4}$ is introduced due to X_c being unbiased at the cell center. Parameters a, b, c are obtained by fitting the calculated electron position density to the uniform distribution, and q is set so as to make the second derivative of the function zero at the cell center. In Fig. 3.11 the distribution of the position density calculated with this correction is presented by dashed line. The periodic structure has almost disappeared.

Shower transverse profile

In the original GAMS design optical grease was used between the lead glass radiators and photomultipliers. Since 1986, however, optical grease has been removed to reduce the noises of muon flux or non interacting hadrons, whose direction is parallel to the GAMS front surface. As a result, the threshold of gamma detection can be reduced, while no deterioration of energy resolution is observed though the total amount of light on the photocathode is reduced by a factor of 3. This is because the energy resolution of lead glass calorimeters much depends on the electromagnetic shower fluctuations and is not affected by the photostatistics significantly.

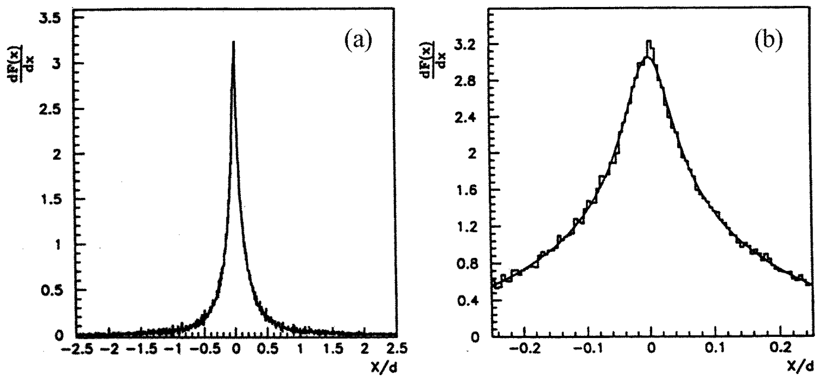

Figure 3.12: (a) X-projection of the transverse energy density distribution in the shower and (b) its enlargement. The horizontal axis in each plot is the transverse coordinate X divided by the cell size d. Plots are from Ref. [33].

The absence of optical grease makes the shower transverse profile different from the representation of the double exponential approximation. A corrected shower profile can be obtained from a two-dimensional cumulative distribution defined as

$$F(x,y) = \int_{-\infty}^{x} \int_{-\infty}^{y} \Phi(x,y)dydx, \tag{3.5}$$

where $\Phi(x,y)$ is the energy density distribution. Here $\Phi(x,y)$ is obtained by differentiating Eq. (3.5). The cumulative function is built using the observed value of energy deposit in each cell: x and y are the horizontal and vertical distances between the right and upper edge of a cell and the impact position evaluated with Eqs. (3.2) and (3.3).

The transverse distribution of the shower energy is axially symmetry in a uniform detector, hence Φ can be expressed as a function of radius, instead of two-dimensional parameters. This leads to a form of an approximation of the transverse shower profile such as

$$\Phi(r) = \frac{1}{2\pi} \sum_{i=1}^{3} \frac{a_i b_i}{(r^2 + b_i^2)^{3/2}}, \tag{3.6}$$

where a_i and b_i are parameters obtained by fitting the calculated Φ to the measured one. Figure 3.12 presents the X-projection of the transverse energy distribution, obtained by differentiating the measured cumulative distribution, and its approximation represented by Eq. (3.6).

Calibration of GAMS

The energy calibration of each cell of GAMS was done by using a 20 GeV/c electron beam produced with a internal target of CERN SPS. GAMS can be moved vertically and horizontally across the beam line so that all cells are irradiated. The beam was defocused for calibration purpose and irradiated about 16 cells simultaneously.

To determine the calibration coefficients α_i of each cell, a formula defined as,

$$\frac{1}{\alpha_i^{(k)}} = \frac{1}{\alpha_i^{(k-1)}} \left(1 - \frac{E_e - E_0^{(k)}}{E_e} \frac{w_i^{(k)}}{\sum_{\nu=1} w_i^{(\nu)}} \right), \tag{3.7}$$

is iteratively used. Here $w_i^{(k)} = (E_i^{(k)}/E_e)^2$ is a weight factor, E_e is the electron energy, $E_i^{(k)} = \alpha_i^{(k-1)} A_i$ where A_i is the amplitude of each cell, $E_0^{(k)}$ is the sum over $E_i^{(k)}$, ν is a number labelling the events. The form of the weight factor $w_i^{(k)}$ is chosen so as to reduce the influence of the hadronic contamination (hadrons release much less energy in the counter). At the start of the iteration, identical calibration coefficients $\alpha_i^{(0)}$ are assigned to all cells as a zero approximation. Then new values of coefficients $\alpha_i^{(k)}$ are calculated in each k-th event by using Eq. (3.7) for the cells hit by the electron shower.

This calibration was done once a month during the experimental run.

Separation of two nearby gammas

The gamma reconstruction program follows three steps.

The first step of the procedure is to search clusters. A cluster consists of one or several energy deposited cells adjacent horizontally and vertically each other and are separated from other clusters with zero energy cells. There is a possibility that more than one gamma form a one cluster. These gammas can be separated in the following steps. Each cluster is analyzed independently in the procedure.

The second step and third step are iterated mutually. In the second step, peaks are searched in the cluster. A peak is located in a cell whose deposited energy is higher than any other neighboring cells. Some clusters consist of electron showers made by several gammas and hence contain several peaks. In this case the region of each peak is calculated by sharing the cell energy with other overlapping peak regions, according to the expected energies from the gamma position in each peak and the shower profile (3.6). The gamma position in each peak is calculated in the next step and used in this step after the 2nd iteration.

In the third step, gammas are reconstructed in each peak region. The current reconstruction program is capable to reconstruct two gammas from one peak simultaneously. At first only single gamma is assumed, and a function defined as

$$\chi^2 = \sum_{i=1}^{n} \frac{(A_i - E_i)^2}{c^2 A_i (1 - A_i/E_0) + q}, \tag{3.8}$$

is minimized in two-dimensional space (X and Y). Here A_i is the measured energy of the ith cell, E_i is the calculated energy from the gamma position estimated by Eqs. (3.2) and (3.3) and the shower profile (3.6), and E_0 is the total gamma energy

($\sum A_i$). Two constants, c^2 and q, represent the shower fluctuation coefficient and the electronics noise (pedestal fluctuation), respectively. In the present experiment c^2 is set to 15 MeV. Since the gamma energy is calculated without fit but as the sum over all cell energies, the term $1 - A_i/E_0$ is included. If $\chi^2/N_{\mathrm{d.o.f}} < 3$ ($N_{\mathrm{d.o.f}}$ being the degree of freedom, equal to $N_{\mathrm{cell}} - 2$ with constraints of the total energy and the energy distribution) is achieved, the procedure is finished. Otherwise the two-gamma hypothesis is took into account.

The two gamma separation is done by minimizing Eq. (3.8) in three-dimensional space: $\alpha = (E_1 - E_2)/E_0$, $\Delta X = X_1 - X_2$ and $\Delta Y = Y_1 - Y_2$. The energy and center-of-gravity coordinates of each gamma are calculated from these variables and the total energy E_0 and center-of-gravity coordinates X_0, Y_0 of the peak region, as follows:

$$\begin{aligned} &E_1 = E_0(1+\alpha)/2,\ X_1 = X_0 + \Delta X(1-\alpha)/2,\ Y_1 = Y_0 + \Delta Y(1-\alpha)/2, \\ &E_2 = E_0(1-\alpha)/2,\ X_2 = X_0 - \Delta X(1+\alpha)/2,\ Y_2 = Y_0 - \Delta Y(1+\alpha)/2. \end{aligned} \tag{3.9}$$

The two gamma hypothesis is adopted if χ^2 is relatively smaller than χ^2 in one gamma case (in the present experiment, the condition $\chi^2(2\gamma) < \chi^2(1\gamma) - 6$ is used).

The efficiency ϵ of two nearby gamma separation has been investigated with Monte Carlo simulation of $M \to 2\gamma$ isotropic decay[34]. Here ϵ depends on the two gamma distance and the energy of each gamma, hence ϵ is a three-dimensional function in general. For the better perspective, a variable defined as

$$D = 2MZ/E_0 \tag{3.10}$$

is used instead of the distance of two gammas, where M is the effective mass of two gammas, Z is the distance from the decay point to GAMS and E_0 is the total energy. The dependency of ϵ as a function of D on the decay asymmetry α becomes much week compared with the case being a function of the two gamma distance, therefore ϵ can be presented as a function of two variables (E_0 and D). D is equivalent to the two gamma distance for the symmetric decay ($E_1 = E_2$).

Figure 3.13 presents the results of the simulation at the total energy of $E_0 = 10$ GeV. Figure 3.13(a) presents the efficiency of two nearby gamma separation. Dashed line represents the probability in this program to find only one gamma. The 50% level of the separation efficiency corresponds to $D = 1.9$ cm. Figure 3.13(b) presents the two gamma distance when the third (false) gamma is found during the two gamma separation procedure. Figure 3.13(c) presents the distribution of $D_{\min}$, the distance between the false gamma and the true gamma nearest to the false one in that case. Figure 3.13(d) is same as Figure 3.13(b) but under the condition of $D_{\min} \geq 20$ mm. This shows the probability to find a false gamma is only 0.1% with the criterion of $D_{\min} \geq 20$ mm.

The energy dependence of the efficiency at the same D is determined by fluctuations of energy deposited in each cell and the energy threshold for low energy gamma detection. The two gamma separation efficiencies for the total energy of 4, 10 and 40 GeV are presented in Fig. 3.14.

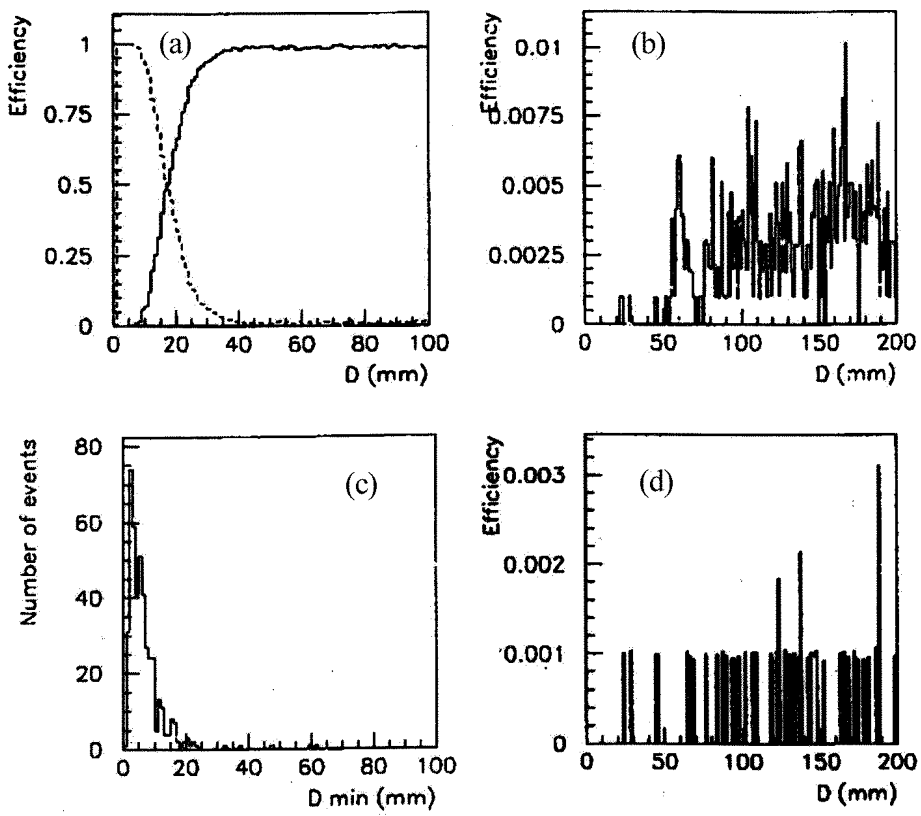

Figure 3.13: (a) Two gamma separation efficiency (solid line) and probability to find only one gamma (dashed line) as a function of D. (b) Probability to find a false gamma in the two gamma separation procedure. (c) Distribution of the distance between the false gamma and the nearer true gamma. (d) Same as (b) but $D_{\rm min} \geq 20$ mm is required. All plots are from Ref. [34].

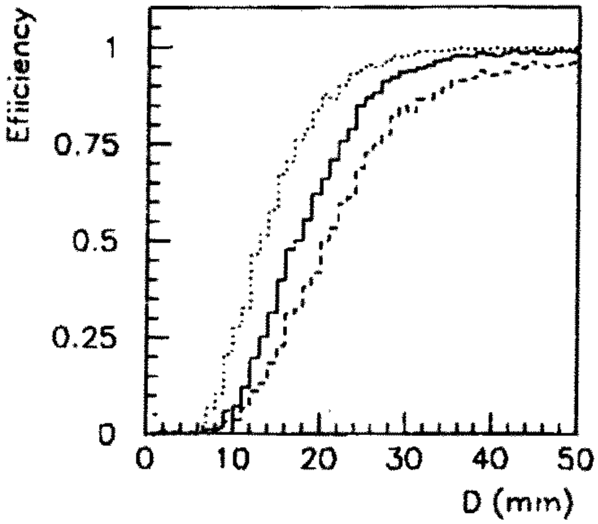

Figure 3.14: Two gamma separation efficiencies for the various total energies[34]. Dashed, solid and dotted lines represent the cases of E_0 = 4, 10 and 40 GeV, respectively.

For the two gamma separation with an efficiency higher than 90% $D \geq 3.5$ cm is required from Fig. 3.13(a) or Fig. 3.14. This value for $Z \sim 11$ m corresponds to $E_0 \sim 148$ GeV for π^0 and 344 GeV for η, which are larger enough than the typical energies in the real observation (Fig. 3.15). Gammas from different particle decays, however, might come within the closer distance. The probability to fail the separation procedure due to the near miss of two gamma including the above case was studied with Monte Carlo simulation and was found not to be significant for the case of $\eta\pi^0 \rightarrow 4\gamma$ (section 5.3.3).

False gammas arising from the separation procedure are due to the fluctuation of deposited energies or electronics noises, both of which differentiate the shower profile from an ideal one. The reconstruction program would find two gammas instead of true one gamma with this non-ideal shower shape. To avoid these misreconstruction, gammas which are very close to each other and have a very small invariant mass were merged after the reconstruction procedure.

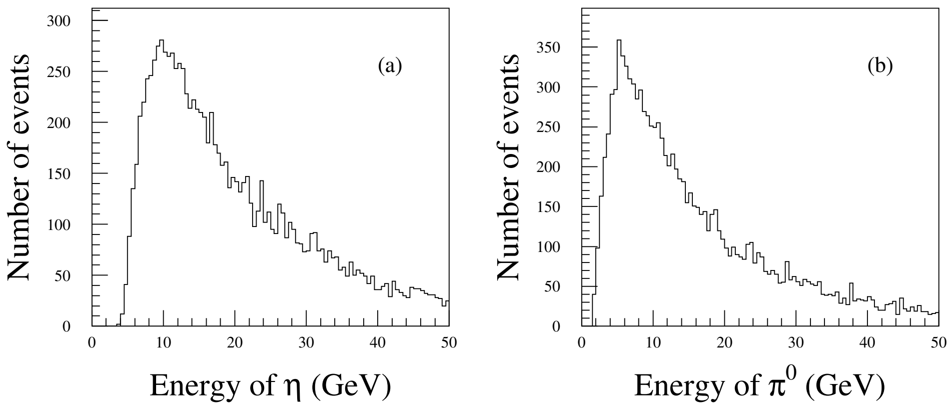

Figure 3.15: (a) Observed η and (b) π^0 energy distributions.

Chapter 4

Event selection for the $\eta\pi^+\pi^-\pi^0$ channel in WA102

This chapter describes details about the selection of the reaction

$$pp \to p_f X^0 p_s,\ X^0 \to \eta\pi^+\pi^-\pi^0,\ \eta/\pi^0 \to 2\gamma,$$

which has four outgoing charged track (the fast proton, slow proton and $\pi^\pm$) and four gammas which arise from η and π^0 decays in the final states.

4.1 Removal of charged track impacts on GAMS

Not only gammas, but also charged particles from the decay of the central system would also hit GAMS and be reconstructed as 'gamma's. These fake gammas make 0,1,2 or 3 gamma events look like four gamma events while turn true four gammas into $5, 6, \ldots$ gammas. To remove these fake gamma events, each charged track was traced from its last measured position to GAMS using its reconstructed momentum, by a fourth order Runge-Kutta method. Figure 4.1(a) shows the distribution of the distance R between the impact points of the extrapolated charged tracks and the nearest GAMS clusters observed in the same event, and (b) presents the distribution of the energies of the clusters being $R < 6$ cm. Events where the number of observed gammas are less than that of observed tracks except the fast and slow proton were selected for the plots. An enhancement below 1 GeV in the energy distribution is thought to correspond to the minimum ionization energy of incident hadrons. Hence all the clusters within being $R < 6$ cm were removed.

4.2 Removal of gammas due to noise

In the WA102 experimental setup, many tracking chambers (A, B and drift chambers, see section 3.1) were located between the target and GAMS to measure the charged particles. The interaction between charged particles and the material

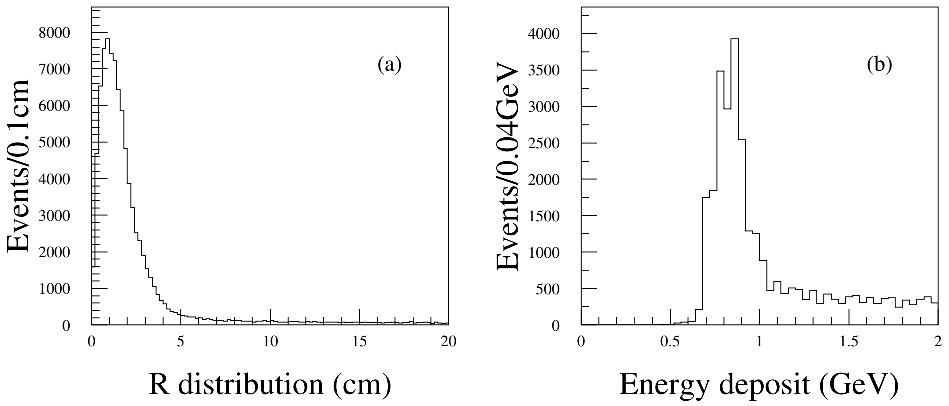

Figure 4.1: (a) Distribution of the distance R between the impact point of the extrapolated track and the nearest GAMS cluster and (b) energy of the cluster being $R < 6$ cm.

of chambers may cause the δ-ray. Because no guard system for slow photons were installed in front of GAMS, the δ-rays would be observed and change the true number of gammas as the same way as the charged track impacts do. The δ-rays are supposed to be observed much more around the center hole of GAMS due to the high intensity of the fast proton.

Figure 4.2 presents the distribution of the observed gamma energy against the distance between its cluster position and the center of GAMS (hole). It can be seen that more low energy gammas are observed at the distance closer to the center of GAMS. The distribution of knock-on electrons with kinetic energy T and passing length x is given by[1]

$$\frac{d^2N}{dTdx} = 2\pi N_A r_e^2 m_e c^2 \frac{Z}{A} \cdot \frac{1}{\beta^2} \cdot \frac{F}{T^2}, \tag{4.1}$$

where Z and A are atomic number and atomic weight of an element passed through, m_e and r_e are the mass and the classical radius of the electron. Here β is p/E where p and E are the momentum and the energy of an incident particle, F is a factor which is dependent on the spin of an incident particle. When the incident particle is the proton with the incident energy of 400 GeV, which is a typical energy of the fast proton, both of β and F are approximately equal to 1 and Eq. (4.1) becomes

$$\frac{dN}{dT} = 1.54 \times 10^{-4} \frac{Z}{A} \cdot \frac{1}{T^2} \cdot \Delta x, \tag{4.2}$$

where T is given in GeV and x is given in g/cm^2. Integrating from T_{thr} to T_{max}, where T_{max} is the maximum kinetic energy that the recoiled electron can have, being

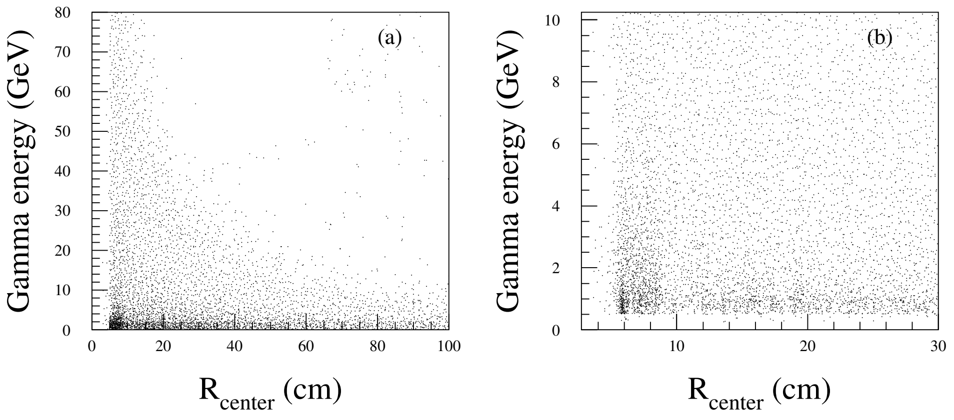

Figure 4.2: (a) Distribution of the observed gamma energy against the distance between its cluster position and the center of GAMS and (b) its enlargement.

approximately 250 GeV in this case, Eq. (4.2) becomes

$$N = 1.54 \times 10^{-4} \frac{Z}{A} \cdot \frac{1}{T_{thr}} \cdot \Delta x, \tag{4.3}$$

since N becomes nearly zero at $T \simeq T_{max}$. The material in front of GAMS is estimated as $Z \sim 10$, $A \sim 20$ and Δx being of the order of 1 g/cm^2, therefore the probability that the δ-ray arises with the energy above 1 GeV during one fast proton passes through can be estimated to be of the order of 1/10000. In the case of the medium tracks, which have a typical energy of 10 GeV, this probability becomes much smaller. Considering above, energy threshold values were set as follows:

$$\begin{array}{rl} R < 9.0 \text{ cm} & E_\gamma > 2.4 \text{ GeV} \\ 9.0 < R < 20.0 \text{ cm} & E_\gamma > 1.2 \text{ GeV} \\ R > 20.0 \text{ cm} & E_\gamma > 0.8 \text{ GeV} \end{array}$$

where R is the distance between the cluster position and the center of GAMS. By imposing these energy thresholds, δ-rays can be almost removed.

4.3 Removal of other channels

At first events with four outgoing charged tracks and four gammas were selected by imposing cuts on the missing momentum of the reaction as follows:

$$\begin{array}{l} |\text{Missing } P_x| < 20.0 \text{ GeV}/c \\ |\text{Missing } P_y| < 0.25 \text{ GeV}/c \\ |\text{Missing } P_z| < 0.20 \text{ GeV}/c \end{array}$$

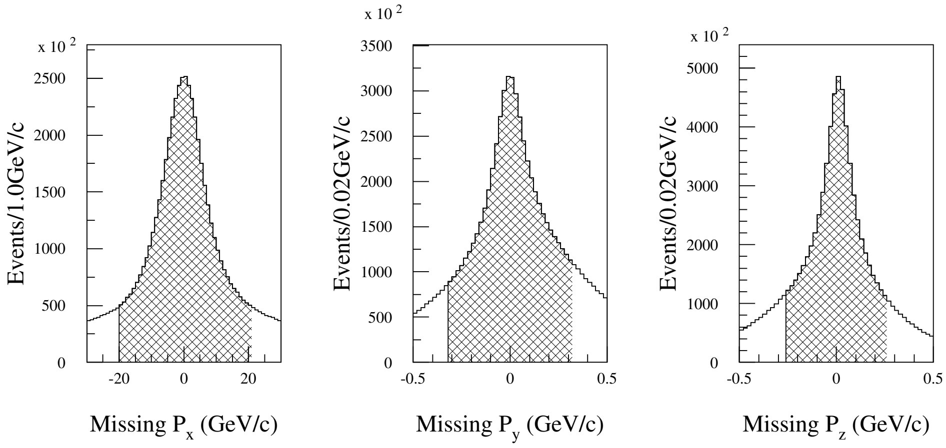

Figure 4.3: Missing x (left), y (middle) and z (right) momentum distributions of the reaction. The hatched section is the selected region by the missing momentum cut.

where the x-axis is along the beam direction. Figure 4.3 presents the x, y and z component of the missing momentum of the reaction.

Then combinations of gamma pairs in each event were investigated. To select a gamma pair which arose from η or π^0 decays, the following mass windows are set:

$$0.10 < M(2\gamma) < 0.17 \text{ GeV}/c^2 \quad \text{for } \pi^0,$$
$$0.46 < M(2\gamma) < 0.64 \text{ GeV}/c^2 \quad \text{for } \eta.$$

If the invariant mass of one pair is within the η mass window and the another pair is within the π^0 mass window, these four gammas are marked as a $\eta\pi^0$ candidate. Events with four gammas which have at least one marked combination were selected at this step.

The two-dimensional plot of invariant mass of any two gammas (M_{12}) versus that of two others (M_{34}) for the selected event are shown in Fig. 4.4(a) (three entrees per one event). Two concentrations of events at $M_{12} \sim 0.13$ GeV/c^2 and $M_{34} \sim 0.55$ GeV/c^2 and at $M_{12} \sim 0.55$ GeV/c^2 and $M_{34} \sim 0.13$ GeV/c^2 correspond to combinations which are selected by the $\eta\pi^0$ mass window. Figure 4.4(a) also shows another concentration of events at M_{12} and $M_{34} \sim 0.13$ GeV/c^2. This suggests four gammas which arose from $\pi^0\pi^0$ decay are also included in the selection cut. Figure 4.4(b) shows the projection of the η mass region in (a) sliced with the π^0 mass window. It contains many backgrounds below an unclear η signal. Figure 4.4(c) is the enlargement of Fig. 4.4(a) ($\pi^0\pi^0$ region is removed from the plot for the better view), which shows clear bands at the π^0 mass vertically and horizontally. Figure 4.4(d) presents the projection of the vertical and horizontal bands except the $\pi^0\pi^0$ region, where a clear signal of π^0 can be seen. This suggests that events, two of whose four gammas arose from π^0 decay but the rest of them did not come from π^0 nor η decays, are also included in the selection cut.

These $\pi^0\pi^0$ and $\pi^0 2\gamma$ backgrounds are thought to originate from:

1. $\pi^+\pi^-\pi^0\pi^0$ channel—the $\pi^+\pi^-\pi^+\pi^-$ channel is observed dominantly in the central production[36, 37], therefore the $\pi^+\pi^-\pi^0\pi^0$ channel is also expected to be dominant in the same process.

2. $\pi^+\pi^-\pi^0\pi^0\pi^0$ channel with falling 2γ within the momentum balance cuts—the cross section for $f_1(1285)$ production is calculated as being 6919 ± 886 nb in the present experiment and $f_1(1285)$ decays into $\eta\pi\pi$ with a fraction of 52.8%[38], and η decays into 3π with a fraction of 55.5% (31.9% into $3\pi^0$ and 23.6% into $\pi^+\pi^-\pi^0$)[1], hence $\pi^+\pi^-\pi^0\pi^0\pi^0$ channel is also expected to have a large intensity.

The $\pi^+\pi^-\pi^0\pi^0\pi^0$ channel would appear in such two different way as:

a) falling two gamma from one π^0 decay, that is, as $\pi^+\pi^-\pi^0\pi^0$,

b) falling one gamma from one π^0 decay and another one from a different π^0 decay, that is, as $\pi^+\pi^-\pi^0 2\gamma$.

Therefore the $\pi^+\pi^-\pi^0\pi^0\pi^0$ channel would create both of the $\pi^0\pi^0$ peak and π^0 bands in Figs. 4.4(a) and (c). To remove the backgrounds originating from both of the $\pi^+\pi^-\pi^0\pi^0$ and $\pi^+\pi^-\pi^0\pi^0\pi^0$ channel, the following criterion was applied:

- any two gamma pair must not have an invariant mass within the π^0 window except the pair from the $\eta\pi^0$ combination.

This selection cut completely removes backgrounds which have a $\pi^0\pi^0$ component and the remaining background is the case b) of the $\pi^+\pi^-\pi^0\pi^0\pi^0$ channel only when the two remaining gammas which arose from different π^0 decays have an invariant mass within the η mass window accidentally. The probability that this happens is thought to be very small.

Figure 4.5 is same as Fig. 4.4(b) but with the condition described above. Backgrounds are considerably reduced and the η signal becomes much clearer than one in Fig. 4.4(b). This selection cut, however, rejects about 15% of true $\eta\pi^+\pi^-\pi^0$ events around mass of 2.0 GeV/c^2 and this ratio increases up to as high as 60% near the $f_1(1285)\pi^0$ threshold ($\sim$ 1.4 GeV/c^2). The most important region lies around 2.0 GeV/c^2, however, and the intensity of exotic states is expected to be small compared with that of $f_1(1285)$ or other background channels, this selection cut is really needed[1].

[1]The selection cuts in the present analysis are optimized for the observation of $f_1(1285) \rightarrow \eta\pi^+\pi^-$ signal. If this cut is not applied, the ratio of the $f_1(1285)$ signals to backgrounds is considerably small.

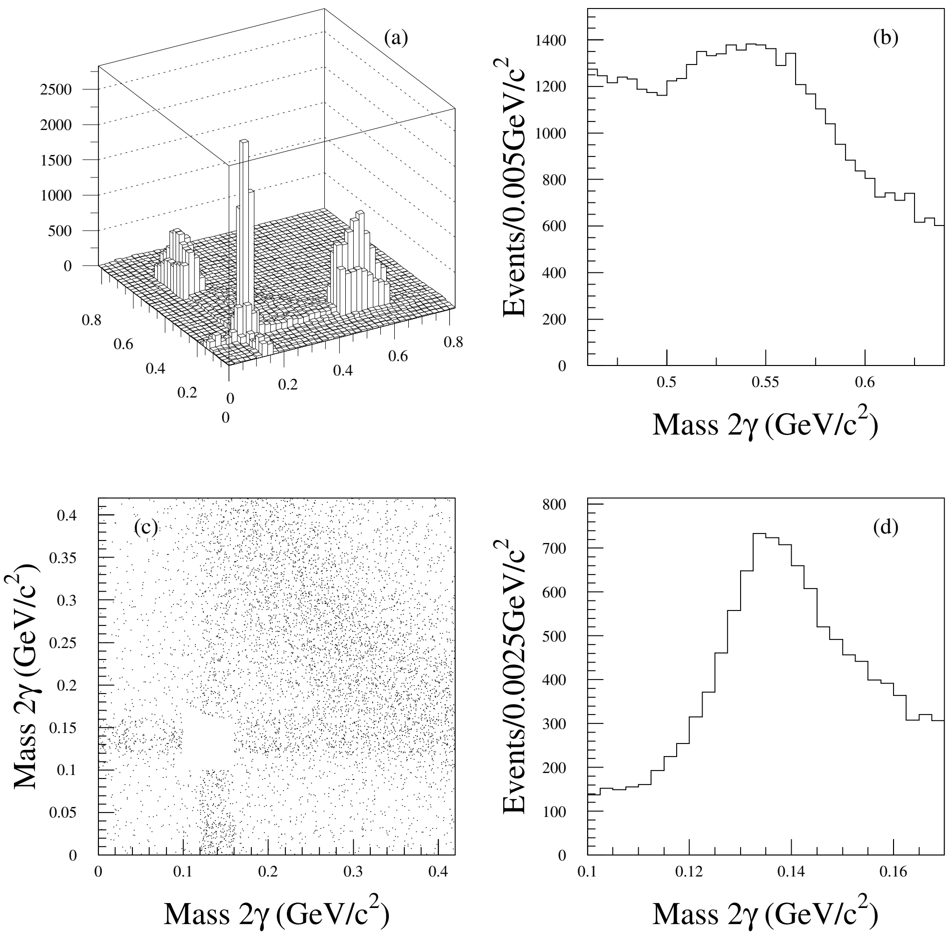

Figure 4.4: (a) Two-dimensional plot of two gamma mass versus two gamma mass for any combination from four gammas selected as $\eta\pi^0$ candidates (three entries per one event). (b) Projection of the $\eta\pi^0$ region in (a). (c) Enlargement of (a) (the $\pi^0\pi^0$ region is removed from the plot). (d) Projection of the bands at π^0 mass in (c).

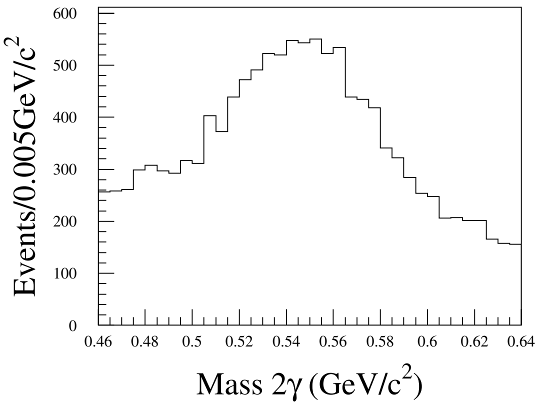

Figure 4.5: Same as Fig. 4.4 (b) but with the condition that any two gamma except the pair from the $\eta\pi^0$ combination doesn't have an invariant mass within the π^0 mass window.

$f_1(1285)$ also has an $\eta\pi\pi$ decay mode with the largest decay fraction of 50%. Thus it is also needed to check the contribution of such events as

$$\eta\pi^+\pi^- + 2 \text{ fake gammas},$$

which pass through the momentum balance cuts. The contribution of these events is expected not to be large, however, due to the energy threshold of GAMS which reduces δ-ray events. The δ-rays are the most possible origin of fake gammas. To investigate the affect of these events, true $\eta\pi^+\pi^-$ events were sampled and randomly mixed with the two gammas which were selected as π^0 in the $\eta\pi^+\pi^-\pi^0$ channel. Figure 4.6(a) shows the mass spectrum of the generated event. A dominant peak can be seen at 1.6 GeV/c^2 which corresponds to $f_1(1285)$ + 2 fake gammas. Figure 4.6(b) presents the $\eta\pi^+\pi^-\pi^0$ mass spectrum and no peak corresponding to the peak in Fig. 4.6(a) can be seen. Hence the contribution of the $\eta\pi^+\pi^-$ channel has been found to be negligible.

4.4 Cut on the confidence level

For the events which were selected by the procedure described in previous sections, a kinematical fit was applied to identify the $\eta\pi^+\pi^-\pi^0$ channel and correct kinematical parameters of particles.

The procedure of the kinematical fit was as follows. The following function is defined for each event:

$$\chi^2 = \sum_{i=1}^{N} \left(\frac{x_i - x_i^o}{\sigma_i} \right)^2, \tag{4.4}$$

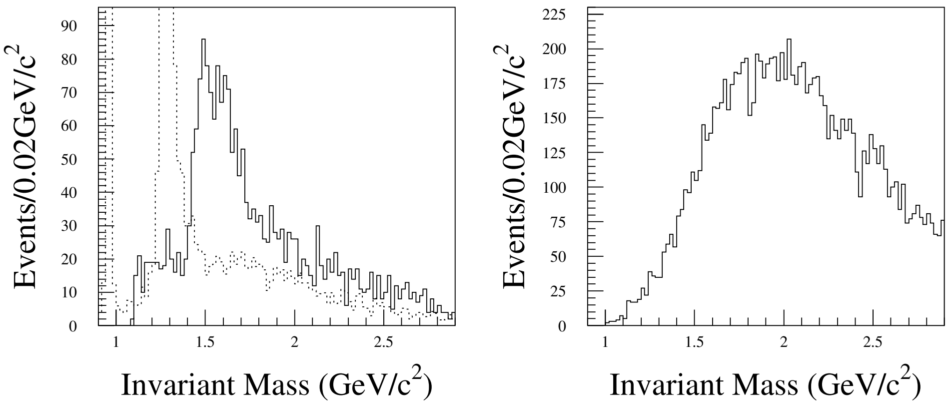

Figure 4.6: (a) Mass distribution of generated events, where events sampled from the $\eta\pi^+\pi^-$ channel were mixed with two gammas selected as π^0 in the $\eta\pi^+\pi^-\pi^0$ channel. The dotted histogram shows the mass distribution of the $\eta\pi^+\pi^-$ channel (the number of events is normalized to that of the generated event). (b) Mass distribution of the $\eta\pi^+\pi^-\pi^0$.

where x_i represents the corrected kinematical parameter to be obtained by the fit, x_i^o and σ_i represents the measured value and its error of the parameter. The kinematical parameters are took as three components of each particle momentum. There are 9 particles in the reaction except the target (the beam, fast, slow proton, $\pi^\pm$ and four gammas) therefore there are $N = 3\times 9 = 27$ kinematical parameters for the $\eta\pi^+\pi^-\pi^0$ channel. Because the coordinate x, y on GAMS and energy E_γ are measured values for each gamma, kinematical parameters for gammas are practically x, y and E_γ. From these parameters momentum of each gamma is calculated as

$$p_{x_i} = E_\gamma \cdot \frac{x_i}{r}, \tag{4.5}$$

where $x_i = \{x, y, z\}$ and $r = \sqrt{x^2 + y^2 + z^2}$. Then a set of the parameters which minimize function (4.4) was searched with following constraints:

$$\begin{aligned} &\text{Missing } P_x = 0, \\ &\text{Missing } P_y = 0, \\ &\text{Missing } P_z = 0, \\ &MM^2(p_f p_s) - M^2(\pi^+\pi^-4\gamma) = 0, \\ &M^2(\gamma_1\gamma_2) - M_\eta^2 = 0, \\ &M^2(\gamma_3\gamma_4) - M_{\pi^0}^2 = 0, \end{aligned} \tag{4.6}$$

where $MM(p_f p_s)$ denotes the missing mass of the fast and slow protons, $\gamma_1\gamma_2$ and $\gamma_3\gamma_4$ are gamma pairs which are selected as η and π^0 candidates, respectively. The

$\eta\pi^+\pi^-\pi^0$ events were selected by imposing $\chi^2 < 20$, which corresponds to approximately 50% confidence level.

4.5 Removal of the fast proton correlation

WA102 experiment is designed to observe the central production process, and events from the target diffraction process, where medium particles are correlated with the target proton, are rejected by the slow proton trigger (section 3.1.4). Events where medium tracks correlate with the fast proton, however, are not rejected with any trigger. Figure 4.7 shows the $p_f\pi^+$, $p_f\pi^-$, $p_f\pi^0$ and $p_f\eta$ mass distributions and a clear Δ^{++} signal can be seen at 1.2 GeV/c^2 on the the $p_f\pi^+$ mass spectrum. Though Δ^+ or Δ^0 signals are not clear on the $p_f\pi^0$ and $p_f\pi^-$ mass spectra, events were removed if $M(p_f\pi^+)$, $M(p_f\pi^-)$ or $M(p_f\pi^0) < 1.5$ GeV/c^2 in order to ensure that the observed events come from the central production. No structures cannot be seen on the $p_f\eta$ mass spectrum, and correlations between the slow proton and medium particles were also checked and no enhancements were found on their mass spectra.

Figure 4.8 presents the Feynmann X_F distribution for the fast proton, slow proton and $\eta\pi^+\pi^-\pi^0$ system. The $\eta\pi^+\pi^-\pi^0$ system is clearly separated from the fast and slow protons and this shows the $\eta\pi^+\pi^-\pi^0$ system is centrally produced.

4.6 Results of the event selection

Finally 5669 events of the centrally produced $\eta\pi^+\pi^-\pi^0$ channel were obtained from the 1995 run and 7930 events were obtained from the 1996 run. Figure 4.9 presents the $\eta\pi^+\pi^-\pi^0$ mass spectra of the 1995 and 1996 run, which shows very similar shape each other. Figure 4.10 shows the $\pi^+\pi^-\pi^0$ mass spectrum in the $\eta\pi^+\pi^-\pi^0$ channel and the $\eta\pi^+\pi^-\pi^0$ mass spectrum with the $\eta \to \pi^+\pi^-\pi^0$ cut. Clear η and ω signals can be seen at 0.55 and 0.78 GeV/c^2 in the $\pi^+\pi^-\pi^0$ mass spectrum and a clear peak at 1.6 GeV/c^2 can be seen in the $\eta\pi^+\pi^-\pi^0$ mass spectrum which corresponds to the sum of $f_2'(1525)$ and $f_0(1500)$ state in the $\eta\eta$ channel[39]. These clear signals show the $\eta\pi^+\pi^-\pi^0$ events have been well reconstructed.

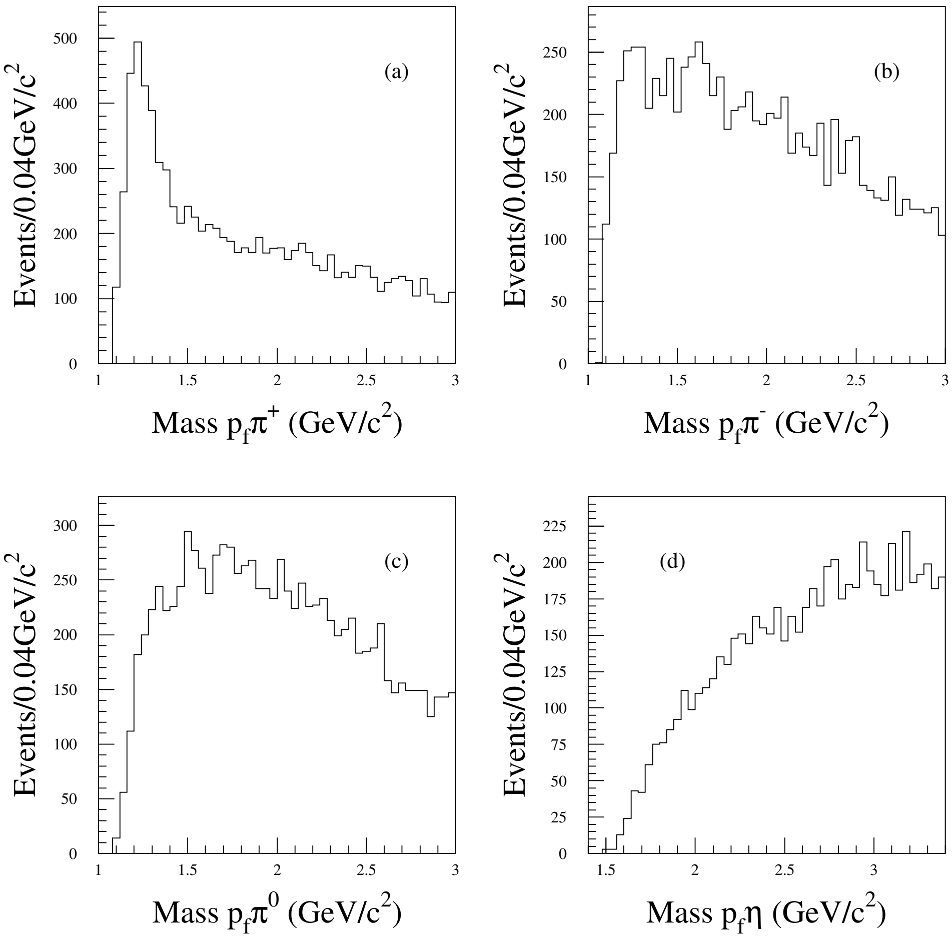

Figure 4.7: Mass distributions of (a) $p_f\pi^+$, (b) $p_f\pi^-$, (c) $p_f\pi^0$ and (d) $p_f\eta$.

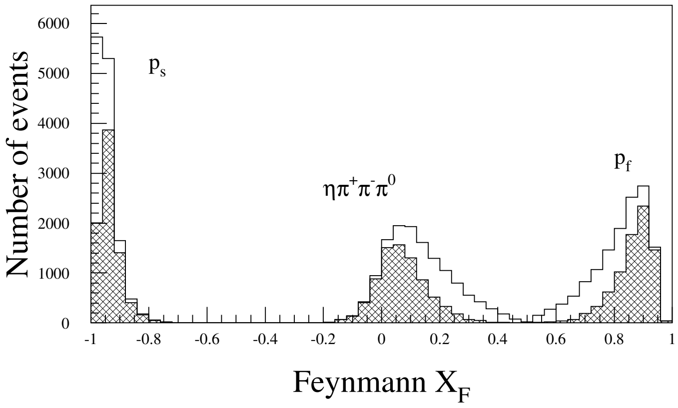

Figure 4.8: Feynmann X_F distribution for the slow proton (left), $\eta\pi^+\pi^-\pi^0$ system (center) and fast proton (right). The open histogram represents the Feynmann X_F before the cut for the fast proton correlation and the hatched section is after the cut.

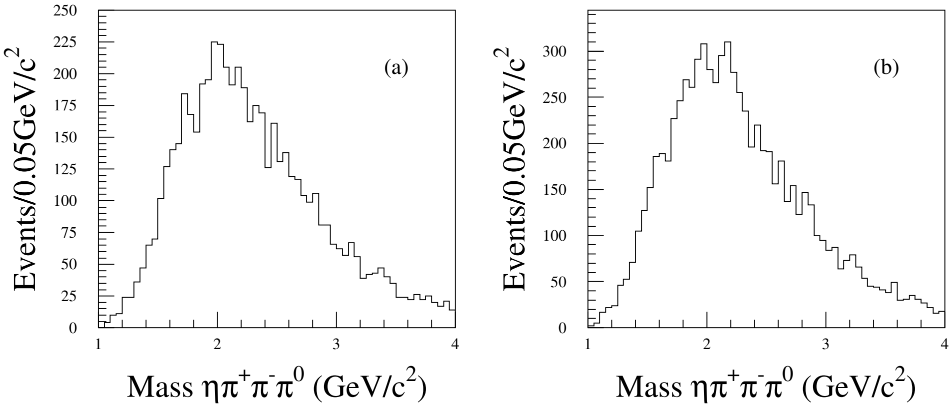

Figure 4.9: (a) Mass spectrum of the $\eta\pi^+\pi^-\pi^0$ system obtained from the 1995 run and (b) 1996 run.

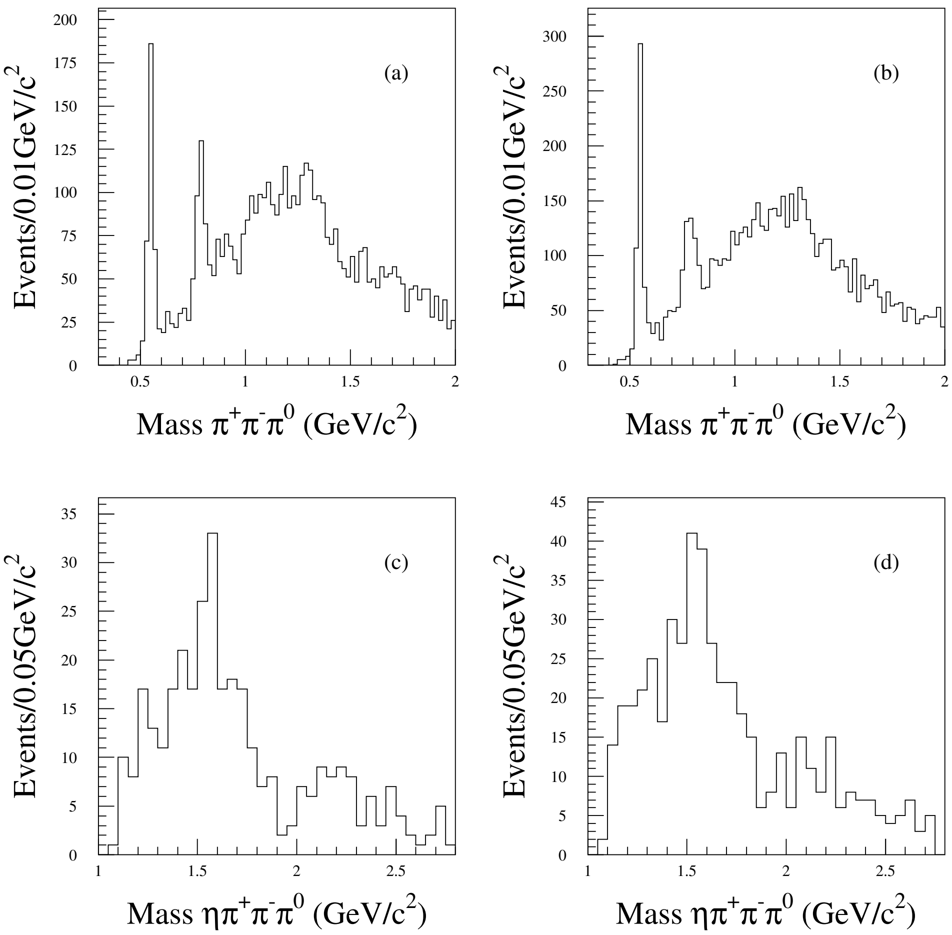

Figure 4.10: (a) $\pi^+\pi^-\pi^0$ mass distribution of the $\eta\pi^+\pi^-\pi^0$ channel and (c) $\eta\pi^+\pi^-\pi^0$ mass distribution with the $\eta \to \pi^+\pi^-\pi^0$ cut. (a) and (c) are obtained from the 1995 data. (b)(d) Same as (a) and (c), respectively, but from the 1996 data.

Chapter 5

Analysis of the $f_1(1285)\pi$ channel

5.1 Selection of the $f_1(1285)\pi^0$ channel

In the WA102 experiment the most suitable mode for the observation of the $f_1(1285)\pi$ channel is one with a decay topology such as,

$$pp \to p_f X^0 p_s,\ X^0 \to f_1(1285)\pi^0,\ f_1(1285) \to \eta\pi^+\pi^-, \tag{5.1}$$

that is, a condition of $\eta\pi^+\pi^- \to f_1(1285)$ is imposed to the $\eta\pi^+\pi^-\pi^0$ channel which is selected with the procedure described in chapter 4. Furthermore, the $\eta\eta$ and η/ω events have been removed if $\pi^+\pi^-\pi^0$ in $\eta\pi^+\pi^-\pi^0$ events are considered to arise from η/ω decay. Figure 4.10 suggests many $\eta\eta/\omega\eta$ events are included in $\eta\pi^+\pi^-\pi^0$ channel and these events appears as backgrounds for $f_1(1285)\pi^0$ channel. In order to avoid $\eta\eta/\omega\eta$ contribution, events have been removed if $\pi^+\pi^-\pi^0$ system has a mass in the following regions

$$0.50 < M(\pi^+\pi^-\pi^0) < 0.60,\ 0.73 < M(\pi^+\pi^-\pi^0) < 0.84\ \text{GeV}/c^2. \tag{5.2}$$

Figures 5.1 and 5.2 present obtained mass spectra of $\eta\pi^+\pi^-\pi^0$ system and its subsystems from the 1995 and 1996 run, respectively. Figures 5.1(a) and 5.2(a) show the $\eta\pi^\pm$ mass distribution and (b) show $\eta\pi^+\pi^-$ mass distribution. Appreciable events can be seen in an $a_0(980)$ region in the $\eta\pi^\pm$ mass spectrum. A hatched section in $\eta\pi^+\pi^-$ mass spectrum is for the events selected with the cut of an $a_0(980)$ region ($0.85 < M(\eta\pi^\pm) < 1.15$ GeV/c^2). An enhancement around 1.3 GeV/c^2 in the $\eta\pi^+\pi^-$ mass plot corresponds to $f_1(1285)/\eta(1295)$ and the same appearance of this peak after the $a_0(980)$ cut shows that the $f_1(1285)/\eta(1295)$ decay is entirely through the $a_0(980)\pi$ channel. An ambiguity of $f_1(1285)/\eta(1295)$ has to be solved by a spin analysis. Figures 5.1(c) and 5.2(c) presents the mass spectrum of two gamma which are selected as a π^0, for the events with a $f_1(1285)$ cut ($1.20 < M(\eta\pi^+\pi^-) < 1.36$ GeV/c^2). Figures 5.1(d) and 5.2(d) presents the $\eta\pi^+\pi^-\pi^0$ mass spectrum with the $f_1(1285)$ cut. A hatched section is obtained after the η/ω regions are removed as described above. Contributions of $\eta\eta/\omega\eta$ events concentrate in the lower mass region of the $\eta\pi^+\pi^-\pi^0$ system and thus the removal of $\eta\eta/\omega\eta$ events is found not to affect much on the mass spectrum in the region above 1.7 GeV/c^2, which is the important region for the search for the hybrid of the $f_1(1285)\pi^0$ channel.

5.2 Study of the mass spectrum

Finally obtained mass spectra of $\eta\pi^+\pi^-\pi^0$ with $f_1(1285)$ cut are presented in Figs. 5.1(d) and 5.2(d) for the 1995 and 1996 data, respectively. Total of 742 events remain after removal of $\eta/\omega \rightarrow \pi^+\pi^-\pi^0$ (hatched section in histogram) from the 1995 data and 1069 events from the 1996 data.

The number of events included in π^0 peaks (Figs. 5.1(c) and 5.2(c)) is greater than those included in $f_1(1285)/\eta(1295)$ peaks (Figs. 5.1(b) and 5.2(b)). To confirm that the peak of $\eta\pi^+\pi^-$ mass spectrum is correlated to the π^0 signals, the narrower mass window has been imposed for π^0 signals and it has been found that the $f_1(1285)/\eta(1295)$ peak clearly remains. Figure 5.3 shows $\eta\pi^+\pi^-$ mass spectrum with the π^0 window of $0.13 < M(2\gamma) < 0.15$ GeV/c^2.

In order to estimate the number of $f_1(1285)\pi^0$ signals the number of events included in the $f_1(1285)/\eta(1295)$ peak was calculated by fit to the spectrum using a Breit-Wigner convoluted with a Gaussian and a background of the conventional form $a(m-m_{th})^b \exp(-cm-dm^2)$, where m is the $\eta\pi^+\pi^-$ mass, m_{th} is the threshold mass and a, b, c, d are fit parameters. The Gaussian accounts for the experimental resolution. The Breit-Wigner convoluted with a Gaussian is calculated as

$$bwcon(m) = \int_{m'_{low}}^{m'_{high}} Gauss(m'-m) BW(m', m_0) dm', \tag{5.3}$$

where $bwcon(m)$ is the calculated contribution for each value m, summing over m', the full mass range of the meson, $Gauss(m'-m)$ is a Gaussian centered at $m'-m$ from the peak of the meson, and BW is the value of the Breit-Wigner at m'. The result of the fit is presented in Fig. 5.4. In the fit m'_{high} and m'_{low} were taken as 1.20 and 1.36 GeV/c^2, respectively, and the experimental resolution and Breit-Wigner width were fixed to 0.020 and 0.024 GeV/c^2, respectively. The experimental resolution was estimated with the Monte Carlo simulation (section 5.3.3). Both of the $\eta\pi^+\pi^-$ mass spectra of the 1995 and 1996 data are represented well and the number of events included in the peak was obtained as

$$\begin{aligned} &210 \pm 36 \quad \text{(for the 1995 data)}, \\ &320 \pm 43 \quad \text{(for the 1996 data)}. \end{aligned} \tag{5.4}$$

Comparing the number of events included in the $f_1(1285)/\eta(1295)$ peak with that of backgrounds under the peak, the $\eta\pi^+\pi^-\pi^0$ mass spectrum with $f_1(1285)$ cut has been estimated to contain backgrounds about 2.5 times more than $f_1(1285)/\eta(1295)\pi^0$ signals. The structure of backgrounds can be estimated by $\eta\pi^+\pi^-$ events in the regions at sidebands of the $f_1(1285)/\eta(1295)$ peak (what is called "control region").

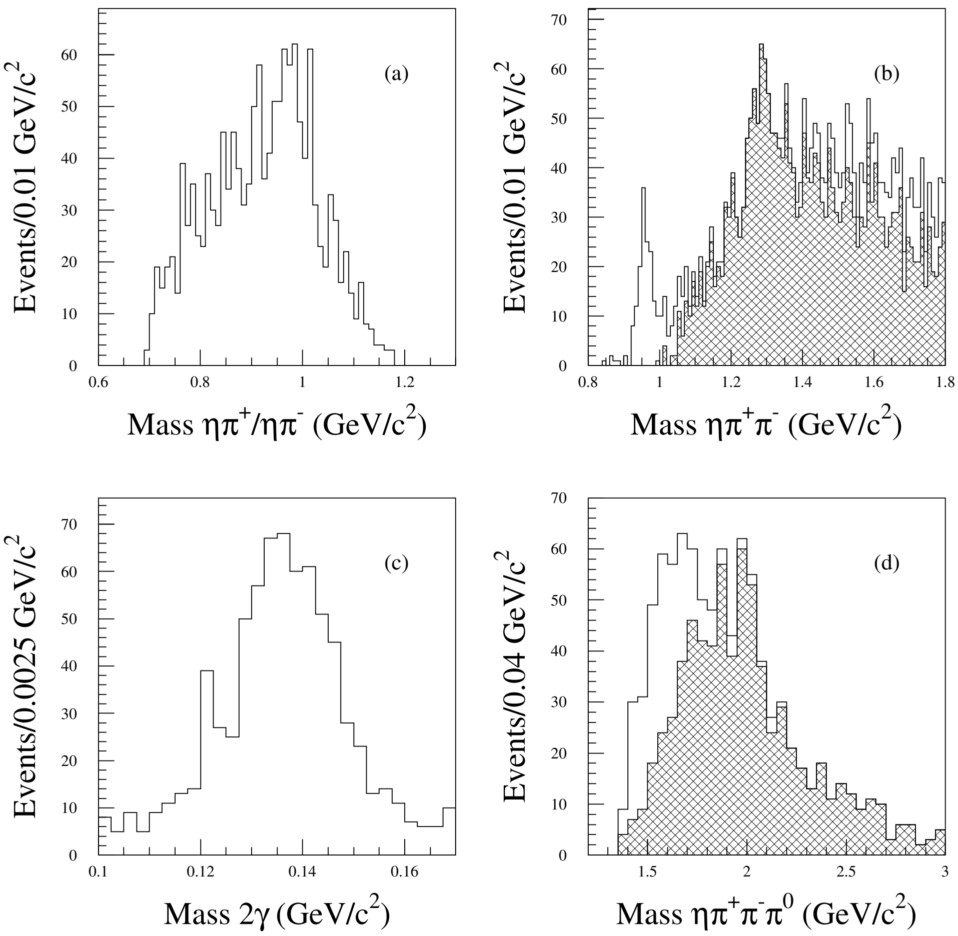

Figure 5.1: Mass distributions for the 1995 data. (a) $\eta\pi^{\pm}$ mass spectrum. (b) $\eta\pi^+\pi^-$ mass spectrum. A hatched section is for the $a_0(980)$ cut. (c) 2 gamma mass spectrum for π^0 with the $f_1(1285)$ cut. (d) $\eta\pi^+\pi^-\pi^0$ mass spectrum. A hatched section is for the removal of $\eta\eta/\omega\eta$ events.

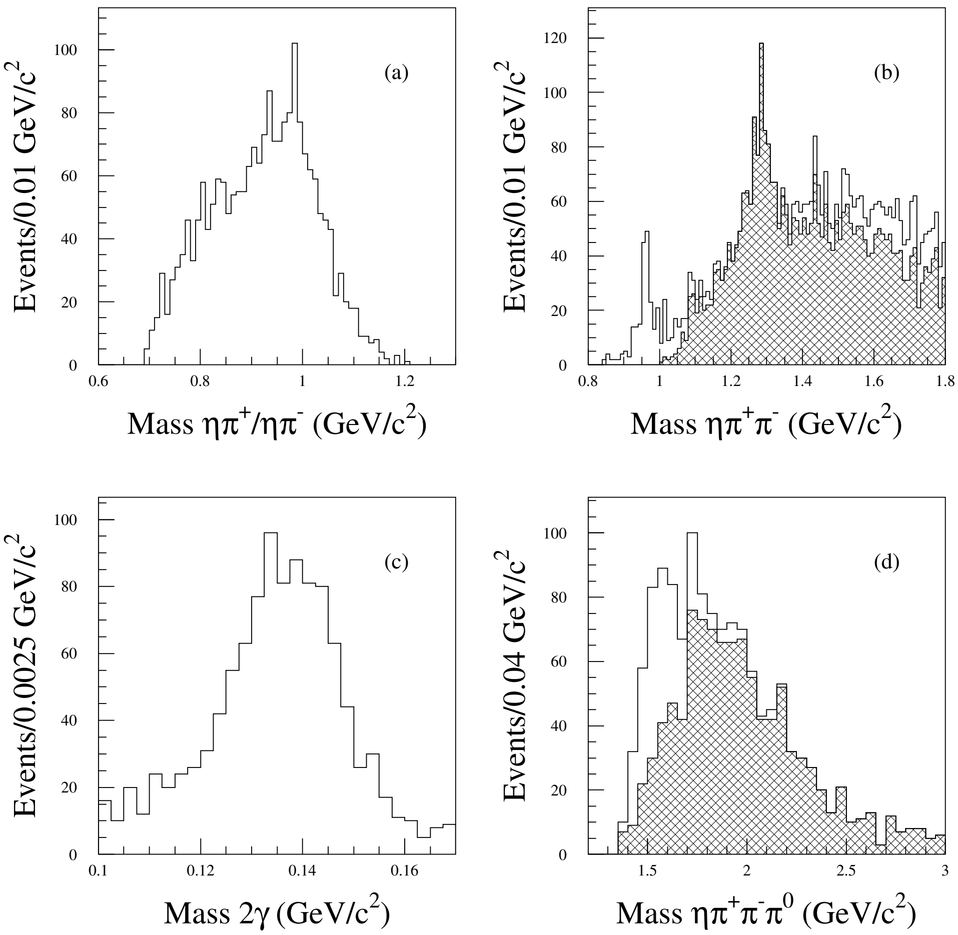

Figure 5.2: Same as Fig. 5.1 but data are from the 1996 run.

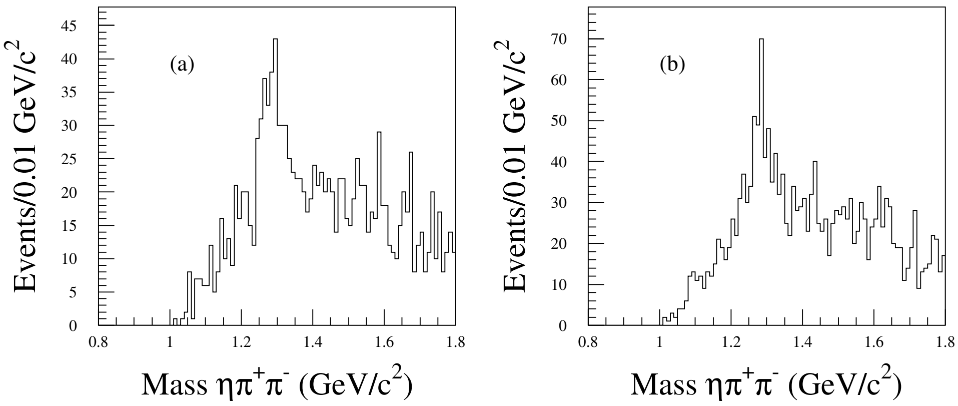

Figure 5.3: (a) $\eta\pi^+\pi^-$ mass spectrum with the narrower π^0 window of $0.13 < M(2\gamma) < 0.15$ GeV/c^2 for the 1995 data. (b) Same as (a) but for the 1996 data.

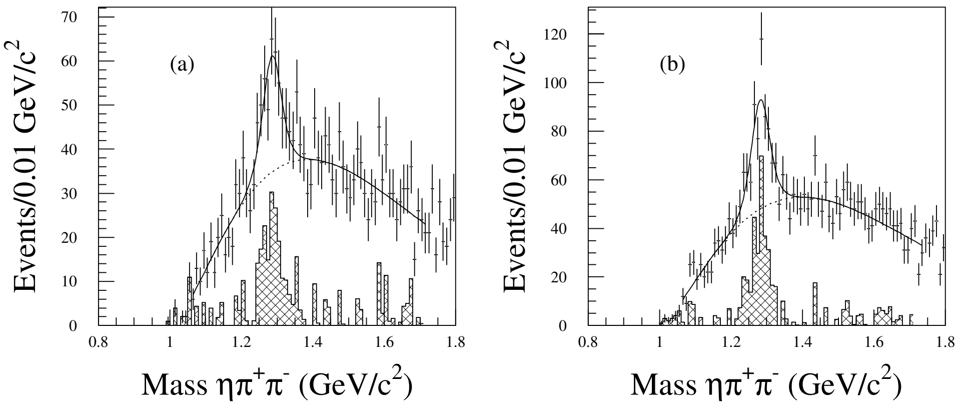

Figure 5.4: (a) $\eta\pi^+\pi^-$ mass spectrum with the fit as described in the text from the 1995 data. A hatched histogram is after backgrounds are subtracted. (b) Same as (a) but for the 1996 data.

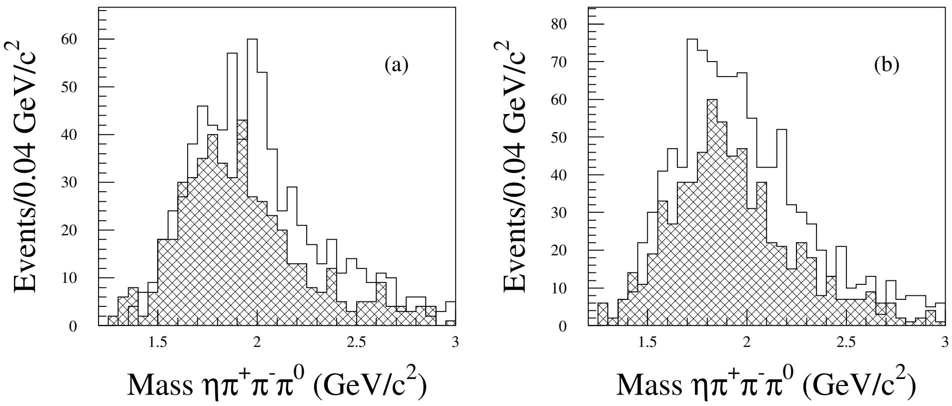

Figure 5.5: (a) Comparison between $\eta\pi^+\pi^-\pi^0$ mass spectra obtained with the $f_1(1285)$ cut and with the control region cut for the 1995 data. (b) Same as (a) but for the 1996 data.

Figure 5.5 presents comparisons between the $\eta\pi^+\pi^-\pi^0$ mass spectrum with the $f_1(1285)$ cut and that of the control regions. The control regions have been defined as $1.07 < M(\eta\pi^+\pi^-) < 1.20$ GeV/c^2 and $1.36 < Mass(\eta\pi^+\pi^-) < 1.43$ GeV/c^2 so as that the number of events included in the control region is compatible with that of backgrounds included in the $f_1(1285)$ cut. Figure 5.5 suggests that the broad structure of the $\eta\pi^+\pi^-\pi^0$ mass spectrum is almost characterized by the background events.

Besides the broad structure, the $\eta\pi^+\pi^-\pi^0$ mass spectra of both of the 1995 and 1996 data have small bumps in the mass region of 1.7–2.2 GeV/c^2, though the statistical fluctuation is not small. In this mass region, some significant partial wave intensities have been observed in the previous experiments (summarized in Table 2.2). To check if the structure in the mass of 1.7–2.2 GeV/c^2 are originated by the $f_1(1285)/\eta(1295)\pi^0$ events, the narrower π^0 mass window was applied, which would enhance the $f_1(1285)/\eta(1295)\pi^0$ events against the background events relatively (see Figs. 5.1(c) and 5.2(c)). Figure 5.6 shows the $\eta\pi^+\pi^-\pi^0$ mass spectrum with the $f_1(1285)$ cut and the narrower π^0 window of $0.13 < M(2\gamma) < 0.15$ GeV/c^2. The bumps in both spectra remain but are difficult to be distinguished from the statistical fluctuation.

In summary, the broad structure of the $\eta\pi^+\pi^-\pi^0$ mass spectrum with the $f_1(1285)$ cut is considered to be due to backgrounds. A small bump has been observed in the mass region of 1.7–2.2 GeV/c^2, where the previous experiments observed some significant partial waves. However, it appears difficult to extract any conclusions from the total mass spectrum, and a partial wave analysis is really needed for further studies.

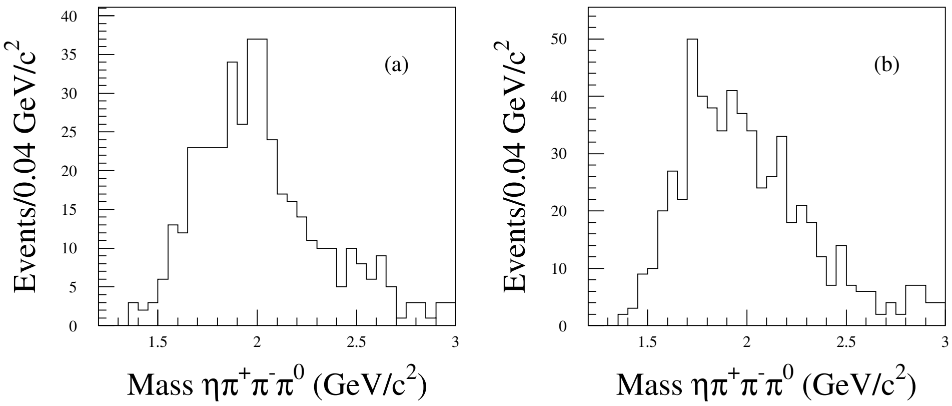

Figure 5.6: (a) $\eta\pi^+\pi^-\pi^0$ mass spectrum with $f_1(1285)$ cut and the narrower π^0 window of $0.13 < M(2\gamma) < 0.15$ GeV/c^2 for the 1995 data. (b) Same as (a) but for the 1996 data.

5.3 Spin analysis for the $f_1(1285)\pi^0$ channel

5.3.1 Definition of axes

In the peripheral case (diffraction process, charge exchange process, etc.), it is easier to define axes so as to give a fixed reference direction to decaying particles, such as the well-known Gottfried-Jackson axes[40]. In the case of central production reaction it is more complicated since there is no plane which will in general contain the 3-momenta of all the particles. Recently, however, successful results of spin analyses of central production have been reported[36, 41, 37, 42]. In their analyses the axes are defined by considering the reaction

$$ab \to X^0, \tag{5.5}$$

where a and b represent the exchanged particles and X^0 represents the central system. The z-axis can be chosen to be along the direction of either of a or b in this case.

The application of above definition to the present analysis is illustrated in Fig. 5.7(a). a and b are taken as the exchanged particles at the fast and slow vertex, respectively. The z-axis is chosen to be along the direction of b in the (a, b) rest frame, since the slow vertex is better measured than the fast one. The (a, b) rest frame is equivalent to the X^0 rest frame, that is, $\eta\pi^+\pi^-\pi^0$ rest frame. The y-axis is defined as $\vec{p}_a \times \vec{p}_b$ in the beam + target rest frame (overall rest frame) and then the x-axis is defined by $\hat{x} = \hat{y} \times \hat{z}$. The decay angle (θ, ϕ) of $X^0 \to f_1(1285)(\eta(1295))\pi^0$ is defined as the

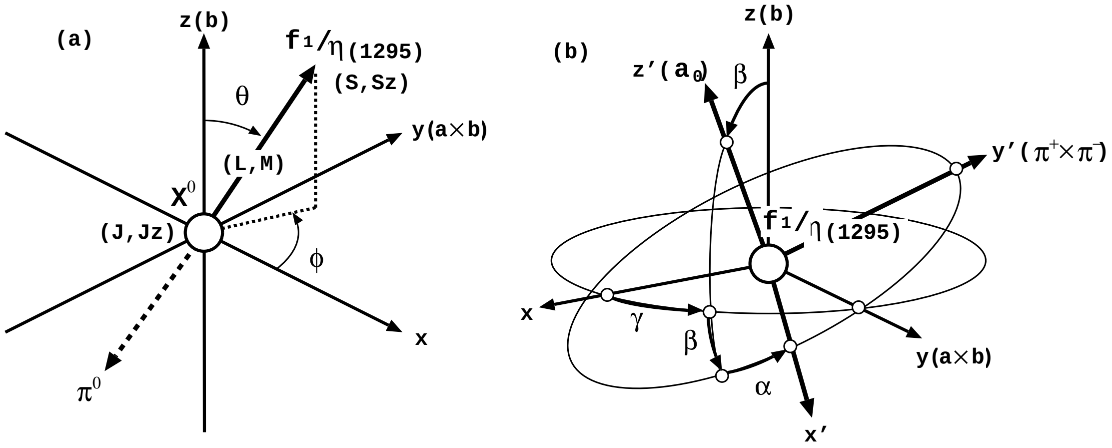

Figure 5.7: (a) Definition of axes for $X^0 \to f_1(1285)/\eta(1295)\pi^0$ decay and (b) for $f_1(1285)/\eta(1295) \to a_0(980)^{\pm}\pi^{\mp}$ decay

direction of $f_1(1285)(\eta(1295))$ in this coordinate system, calculated as

$$\begin{aligned}\cos\theta &= \frac{\vec{p}_{f_1}\cdot\hat{z}}{|\vec{p}_{f_1}|},\\ \phi &= \tan^{-1}\frac{\vec{p}_{f_1}\cdot\hat{y}}{\vec{p}_{f_1}\cdot\hat{x}}.\end{aligned} \tag{5.6}$$

To consider the identification of $f_1(1285)/\eta(1295)$, a sub coordinate system for the decay of $f_1(1285)/\eta(1295)$ into $\eta\pi^+\pi^-$ is also defined, which is illustrated in Fig. 5.7(b). The definition of the coordinate system follows that of the Standard Isobar Model by Herndon et al[43]. The z'-axis is defined to be along the direction of an isobar in the $\eta\pi^+\pi^-$ rest frame, where the isobar is assumed as $a_0(980)$ which is whether $\eta\pi^+$ or $\eta\pi^-$ system in the present analysis. Then the y'-axis is defined as normal to the decay plane of the three particles and the x'-axis is defined by $\hat{x}' = \hat{y}' \times \hat{z}'$. The y'-axis is calculated as $\hat{y}' = \vec{p}_{\pi^+} \times \vec{p}_{\pi^-}/|\vec{p}_{\pi^+} \times \vec{p}_{\pi^-}|$, where $\vec{p}_{\pi^\pm}$ are three momenta of $\pi^\pm$ in the $\eta\pi^+\pi^-$ rest frame. The decay angles, α, β and γ are defined as the Euler angles between the (xyz) and $(x'y'z')$ coordinate system, where the (xyz) coordinate is same as defined in Fig. 5.7(a). Here α, β and γ can be calculated as

$$\begin{aligned}\alpha &= \tan^{-1}\frac{\hat{z}'\cdot\hat{y}}{\hat{z}'\cdot\hat{x}},\\ \beta &= \cos^{-1}\hat{z}'\cdot\hat{z},\\ \gamma &= \tan^{-1}\frac{\hat{y}'\cdot\hat{z}}{-\hat{x}'\cdot\hat{z}}.\end{aligned} \tag{5.7}$$

5.3.2 Calculation of decay amplitudes

For the calculation of decay amplitudes the spin-orbit (LS) scheme using spherical harmonics is applied[36]. In the present analysis L corresponds to the orbital angular momentum between $f_1(1285)/\eta(1295)$ and π^0 and S corresponds to the spin of $f_1(1285)/\eta(1295)$. Since the decay of $f_1(1285)/\eta(1295)$ is observed to be entirely through the $a_0(980)\pi$ channel (Figs. 5.1(b) and 5.2(b)), $a_0(980)$ state is assumed for a $\eta\pi$ isobar and hence the spin of $f_1(1285)/\eta(1295)$ is represented by the orbital angular momentum between the isobar and a bachelor pion. In the following, notations for the axes and angles are the same as defined in the previous section.

Firstly the amplitude for $f_1(1285)/\eta(1295) \to (\eta\pi)\pi$ decay is considered. The $\eta\pi$ isobar and bachelor pion are combined to give the spin of the $f_1(1285)/\eta(1295)$, then the decay amplitude is written as

$$
\begin{aligned}
A^{(S)}(S, S_z) &= \sum_{m,s_z} \left(\begin{array}{cc|c} l & s & S \\ m & s_z & S_z \end{array} \right) Y_l^m(\cos\beta, \gamma) BW(a_0) \qquad (5.8) \\
&= Y_{S_z}^S(\cos\beta, \gamma) BW(a_0) \qquad (5.9)
\end{aligned}
$$

where S is the spin of $f_1(1285)/\eta(1295)$, l is the orbital angular momentum between an $\eta\pi$ isobar and a bachelor pion, s is the spin of the isobar and S_z, m, s_z are their z-components, respectively. The direction of the isobar can be determined by two of three Euler angles, (β, γ), measured in the $f_1(1285)/\eta(1295)$ rest frame as described in the previous section. $BW(a_0)$ represents a Breit-Wigner amplitude used for the propagation of the $a_0(980)$ state and the expression in brackets denotes a Clebsh-Gordan coefficient. Since the $a_0(980)$ is assumed for the isobar, $s = s_z = 0$ and it leads to $S = l, S_z = m$, which simplifies $A^{(S)}(S, S_z)$ as (5.9).

Then the amplitude of $X^0 \to f_1(1285)/\eta(1295)\pi^0$ is coupled with (5.9) to give the total amplitude of the decay. Denoting the angular momentum between f_1/η and π^0 as (L, M) and the spin of X^0 as (J, J_z), the total amplitude is represented as

$$
\begin{aligned}
A^{(L,S)}(J, J_z) &= \sum_{M,S_z} \left(\begin{array}{cc|c} L & S & J \\ M & S_z & J_z \end{array} \right) Y_L^M(\cos\theta, \phi) \\
&\quad \times BW(f_1/\eta) A^{(S)}(S, S_z). \qquad (5.10)
\end{aligned}
$$

where $BW(f_1/\eta)$ is a Breit-Wigner representation of either $f_1(1285)$ or $\eta(1295)$. Because $f_1(1285)/\eta(1295)$ decays into both of $a_0^+(980)\pi^-$ and $a_0^-(980)\pi^+$ with the same probability, $A^{(S)}$ can be represented as

$$
A^{(S)} = \frac{1}{\sqrt{2}}\{A^{(S)+} + A^{(S)-}\}, \qquad (5.11)
$$

where $A^{(S)\pm}$ are calculated with Eq. (5.9) for the $\eta\pi^\pm$ systems, respectively. Each state (5.10) are distinguished by a set of (JJ_zLS), where S determines whether $f_1(1285)$ $(S = 1)$ or $\eta(1295)$ $(S = 0)$ is assumed for the $\eta\pi^+\pi^-$ system.

As examples, some apparent forms of Eq. (5.10) are given in the following. In the case of $X^0 \to \eta(1295)\pi^0$, since $S = S_z = 0$ for $\eta(1295)$, $A^{(L,S)}(J, J_z)$ becomes

$$
A_\eta^{(L,S)}(J, J_z) = A^{(L,S=0)}(J, J_z)
$$

$$= \sum_M \left(\begin{array}{cc|c} L & 0 & J \\ M & 0 & J_z \end{array} \right) Y_L^M(\cos\theta,\phi)$$
$$\times BW(\eta)\frac{1}{\sqrt{2}}\{A^{(0)+}(0,0) + A^{(0)-}(0,0)\}$$
$$= Y_J^{J_z}(\cos\theta,\phi)BW(\eta)\frac{1}{\sqrt{2}}\{BW(a_0^+) + BW(a_0^-)\}. \qquad (5.12)$$

For $X^0 \to f_1(1285)\pi^0$ with $J = 2$, $J_z = 1$ and $L = 2$, (M, S_z) can take $(2,-1)$, $(1,0)$ and $(0,1)$, hence $A^{(L,S)}(J, J_z)$ becomes

$$A^{(L=2,S=1)}(J = 2, J_z = 1) = BW(f_1)\times \qquad (5.13)$$
$$\left\{\frac{1}{\sqrt{3}}Y_2^2(\cos\theta,\phi)\frac{1}{\sqrt{2}}\{Y_1^{-1}(\Omega^+)BW(a_0^+) + Y_1^{-1}(\Omega^-)BW(a_0^-)\}\right.$$
$$+\frac{1}{\sqrt{6}}Y_2^1(\cos\theta,\phi)\frac{1}{\sqrt{2}}\{Y_1^0(\Omega^+)BW(a_0^+) + Y_1^0(\Omega^-)BW(a_0^-)\}$$
$$\left.-\frac{1}{\sqrt{2}}Y_2^0(\cos\theta,\phi)\frac{1}{\sqrt{2}}\{Y_1^1(\Omega^+)BW(a_0^+) + Y_1^1(\Omega^-)BW(a_0^-)\}\right\}. \qquad (5.14)$$

where $\Omega^\pm$ represent $(\cos\beta,\gamma)$ for $\eta\pi^\pm$, respectively.

5.3.3 Study of the detector acceptance

Due to the imperfect detection efficiencies of the experimental setup, each angular distribution will be distorted from the ideal one. Thus it must be corrected in order to calculate the decay amplitude correctly. In the present analysis Monte Carlo simulation was used to estimate the detector acceptance.

In general, proper models should be used to generate physical events for the simulation. However, there are no models that incorporate double exchange processes, where exchanged particles are unknown in the real event, into a single description of central production. Hence events were simulated by a following procedure:

1. A sample of $\eta\pi^+\pi^-\pi^0$ events is taken from real data. The constraint fit has been applied for each sampled event, thus each event satisfies the momentum and energy conservation.

2. 4-momentum of a central system in each event is calculated. This is the sum of η, π^+, π^- and π^0 momenta.

3. Decay of the central system is simulated. Final state particles, $\pi^\pm$ and four gammas, are given 4-momentum.

4. $\pi^\pm$ are tracked and tested if they are detected and can be reconstructed. The detector planes which they pass through, trigger scintillator efficiencies and vertex finding efficiency of TRIDENT are taken into account for the detection and reconstruction criteria.

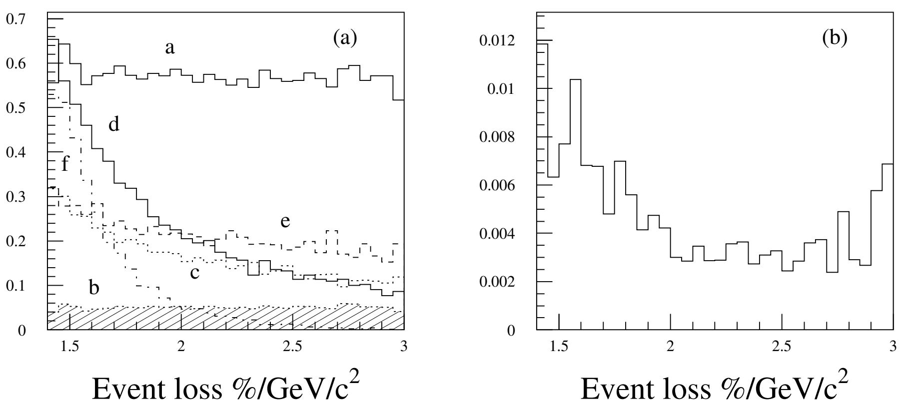

Figure 5.8: (a) Estimated event loss (%) as a function of $f_1(1285)\pi^0$ mass. a: geometrical acceptance for gammas. b: geometrical acceptance and reconstruction efficiency for charged tracks. c: energy cut of GAMS. d: the number of π^0 combinations > 1. e: diffractive cut. f: $\eta/\omega \to 3\pi$ cut. (b) Estimated event loss by the failure of separation procedure of nearby gammas.

5. Gammas are also tested if they are detected by GAMS. Conversion into e^-e^+ pair in the material of tracking chambers (and Čerenkov counter for the 1996 data) and GAMS geometry (its size and a center hole of GAMS) are taken into account.

6. For events where all tracks and gammas are detected, the same event selection procedures as used for the real data are applied.

The fast and slow protons are ignored and detection efficiencies for them can not be estimated in this procedure. However, detection efficiencies for protons are not needed for the correction of the angular distribution. Major sources of event loss are summarized in Fig. 5.8. Geometrical acceptance for gammas almost determines overall detection efficiency. Event loss by the failure of separation procedure of nearby gammas is estimated to be less than 1%.

Then effects of the detector acceptance to an angular distribution were investigated. Figure 5.9 shows a comparison of angular distributions between generated events and accepted ones (for isotropic decay). Dips at $\cos\theta \sim -1$ and 1 are due to poor detections of low energy gammas and the center hole of GAMS. Note that at $\cos\theta \sim -1$ and 1, either of η or π^0 goes along the slow proton and hence they have low energy in the laboratory frame while the other goes to the forward direction and its decay gammas are likely to pass through the hole of GAMS. On the other hand, dips on the $\cos\beta$ distributions are due to diffractive cuts. Figure 5.10 shows these explanations.

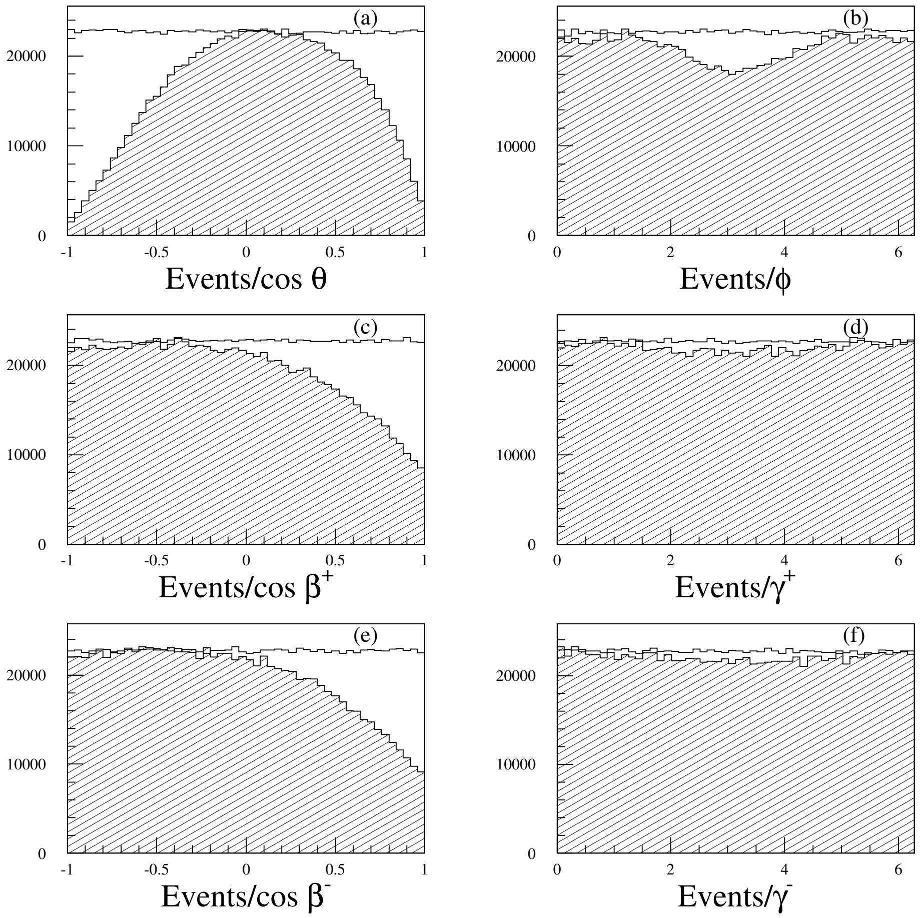

Figure 5.9: Angular distributions of generated events and accepted ones (simulation). (a) $\cos\theta$. (b) ϕ. (c) $\cos\beta^{+}$. (d) γ^{+}. (e) $\cos\beta^{-}$. (f) γ^{-}. Open histograms represent angular distributions of generated events and hatched ones represent those of accepted events. The number of accepted events are arbitrarily normalized.

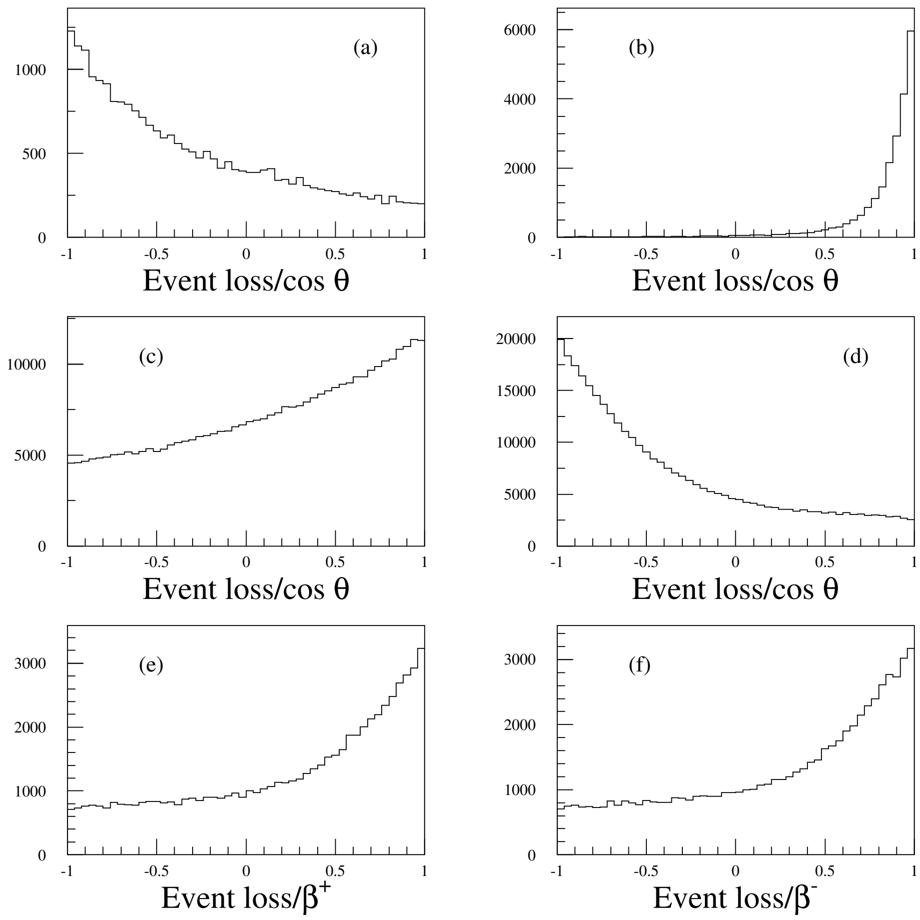

Figure 5.10: Estimated event loss as a function of angular distributions. Each event loss is caused by: (a) gammas from η decay pass through the hole of GAMS. (c) gammas from η decay do not hit GAMS (including the center hole). (b)(d) same as (a)(c) but gammas from π^0 decay. (e)(f) diffractive cut for $\eta\pi^{\pm}$, respectively.
.

In order to correct the distorted angular distribution, each event has to be weighted by a factor ϵ^{-1}, where ϵ represents detector acceptance. Here ϵ will be a function of decay angles $(\theta, \phi, \beta^+, \gamma^+, \beta^-, \gamma^-)$ and $f_1(1285)\pi^0$ mass m in general. However, it needs considerably long computer time to calculate ϵ as a function of full variables by simulation. In practice it is impossible to obtain enough statistics through all dimensions to calculate reliable acceptances. Instead, in the present analysis, ϵ has been calculated as a function of m and a spin model. That is, ϵ has been calculated for each spin hypothesis (as a function of m). Since the acceptance is low at $\cos\theta \sim -1$ and 1, and $\cos\beta^{\pm} \sim 1$, channels with a decay amplitude maximized around these angles lose more events than the other channels. For an example, the acceptance for $(JJ_zLS) = (1010)$ state is estimated to be approximately 10% lower than that of (2211) state at $m = 2.0$ GeV/c^2.

Then an accuracy of the acceptance correction by the above method was investigated as follows. Events were generated by simulating a decay of the central system following an assumed spin model. For these generated events and accepted events, amplitudes of various spin models including one assumed for simulation were calculated and accumulated. The amplitudes for accepted events were weighted by each acceptance factor before accumulated. Then comparing the accumulated amplitude for generated event with that for accepted events, one can check the accuracy of the acceptance correction for each spin state. Significance of each spin amplitude relative to others in a given angular distribution can also be checked in this procedure.

Figure 5.11 shows the sum of squared decay amplitude calculated for generated events. Each bin in a histogram corresponds to each spin model and different spin models are assumed in different histograms for simulating the decay of central system. Digits in histogram titles represent the JJ_zLS of the assumed spin model. The shaded bin in each histogram corresponds to the spin model assumed for simulation. States with spin up to $J = 2$, $L = 2$ were considered. Figure 5.11 shows that all spin models have the largest strength in its own angular distribution. Figure 5.12 presents the case of accepted events without acceptance corrections. Upsets of relative strength occur between some spin models (for an example, 1101 and 1011 strength in 1101 wave). These are due to the different detection acceptances between different states, as described before. Figure 5.13 shows the case of accepted events with acceptance corrections. The upsets have disappeared and an original order of relative strength is almost recovered.

Study of mass resolution

The mass resolution of the present experiment has been studied by the same Monte Carlo procedure. Main parameters of each detector resolution were referred to values from the previous runs[44, 45].

Figures 5.14(a) and (b) show comparisons between the observed and simulated mass spectra of π^0 and η before the kinematical fit. The resolutions of observed data are $\sigma = 9.5 \pm 0.2$ and 28.7 ± 1.2 MeV/c^2 for π^0 and η, respectively, and that

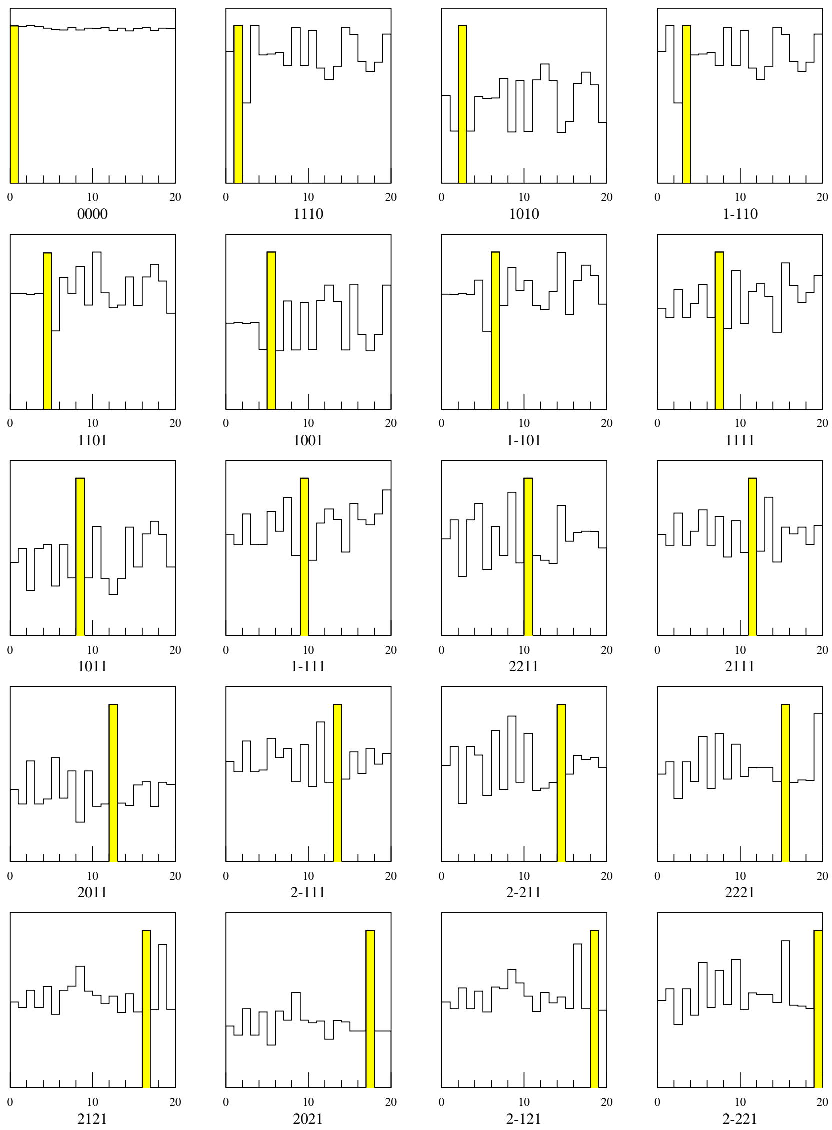

Figure 5.11: Sum of squared decay amplitudes calculated for events generated by simulation. Each bin in a histogram corresponds to each spin model and different spin models are assumed in different histograms for simulating the decay of central system. Digits in histogram titles represent the JJ_zLS of the assumed spin model. The shaded bin in each histogram corresponds to the spin model assumed for simulation.

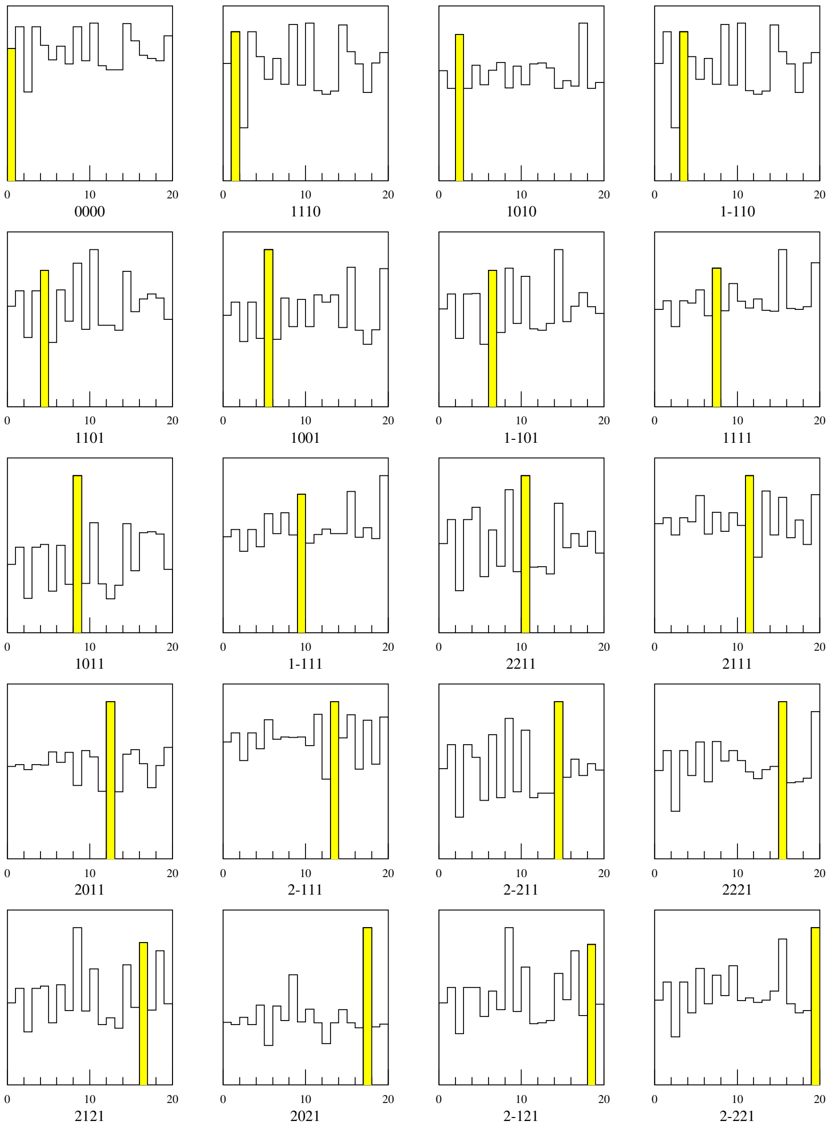

Figure 5.12: Same as Fig. 5.11 but for the case of accepted events without acceptance corrections.

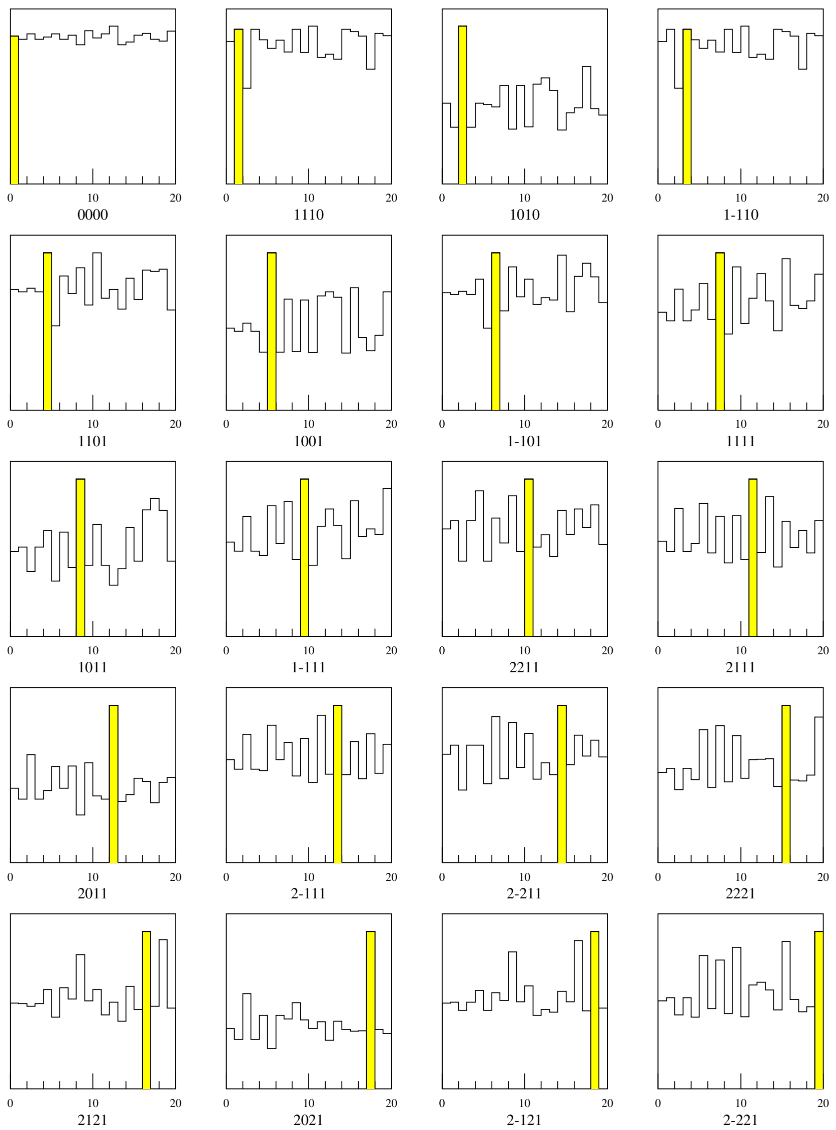

Figure 5.13: Same as Fig. 5.11 but for the case of accepted events with acceptance corrections.

of simulated data are $\sigma = 8.2$ and 27.4 MeV/c^2, respectively. The simulated data reproduce observed data well. Figure 5.14(c) presents the simulated mass spectrum of $f_1(1285)$ with zero width input. This shows expected mass resolution for $f_1(1285)$ after kinematical fit and $\sigma = 19.1$ MeV/c^2 has been obtained. Figure 5.14(d) shows estimated mass resolution for $\eta\pi^+\pi^-\pi^0$ system as a function of mass. A mass resolution $\sigma = 34.4$ MeV/c^2 has been obtained at mass of 2.0 GeV/c^2.

5.3.4 Results of the spin analysis

In order to perform a spin parity analysis, the Log Likelihood Method has been used. The present analysis has referred to the results of the previous experiments (Table 2.2) and spin states with $L \leq 2, J \leq 2$ have been considered.

For each event i and spin model j, a probability weight $P_j(i)$ is constructed as

$$P_j(i) = \frac{|M_j(i)|^2}{\epsilon_j(m)\langle|M_j(m)|^2\rangle}, \tag{5.15}$$

where M_j represents a choice of one of the $A^{(L,S)}(J, J_z)$ terms (5.10) and ϵ_j denotes the acceptance for model j at the $\eta\pi^+\pi^-\pi^0$ mass m. The term $\langle|M_j(m)|^2\rangle$ is the normalization factor which is calculated as the Monte Carlo expectation of the model at m, integrated over the phase space variables. This normalization factor makes all model amplitudes equally probable[1]. The detector acceptance ϵ_j has been calculated by Monte Carlo method for each spin model as described in the previous section. Since there is no interference between different helicity states and both positive and negative helicity amplitudes should be produced at equal rates, the mean of both squared helicity amplitudes is used. Thus each spin model is represented by $JMLS$, which is the same notation described in section 5.3.2 but with the replacement of Jz by its absolute value M. By using the spin-parity of $f_1(1285)$ (1^{++}), $\eta(1285)$ (0^{-+}) and π^0 (0^{-+}), the equivalent notation, J^{PC}[isobar]M will be also used in the following.

In order to include more than one model in the fit, the log likelihood function is defined as the incoherent sum of them[36]:

$$\mathcal{L} = -\sum_i \log\left(\sum_j a_j P_j(i) + (1 - \sum_j a_j)\right), \tag{5.16}$$

where a_j denotes an event fraction of each spin model j and the term $(1 - \sum_j a_j)$ has been introduced to represent background events. Each probability weight P_j

---

[1] Decay amplitudes used in the present analysis have already been normalized within the same decay mode—$f_1(1285)\pi^0$ or $\eta(1295)\pi^0$, by using the normalized spherical harmonics. The difference of amplitudes between $f_1(1285)\pi^0$ and $\eta(1295)\pi^0$ arises from different parametrizations between $f_1(1285)$ and $\eta(1295)$ which are dependent on the phase space of the $\eta\pi^+\pi^-$ system (and thus on m) and the interference term of the spherical harmonics describing the spin of $f_1(1285)$ which is independent of m.

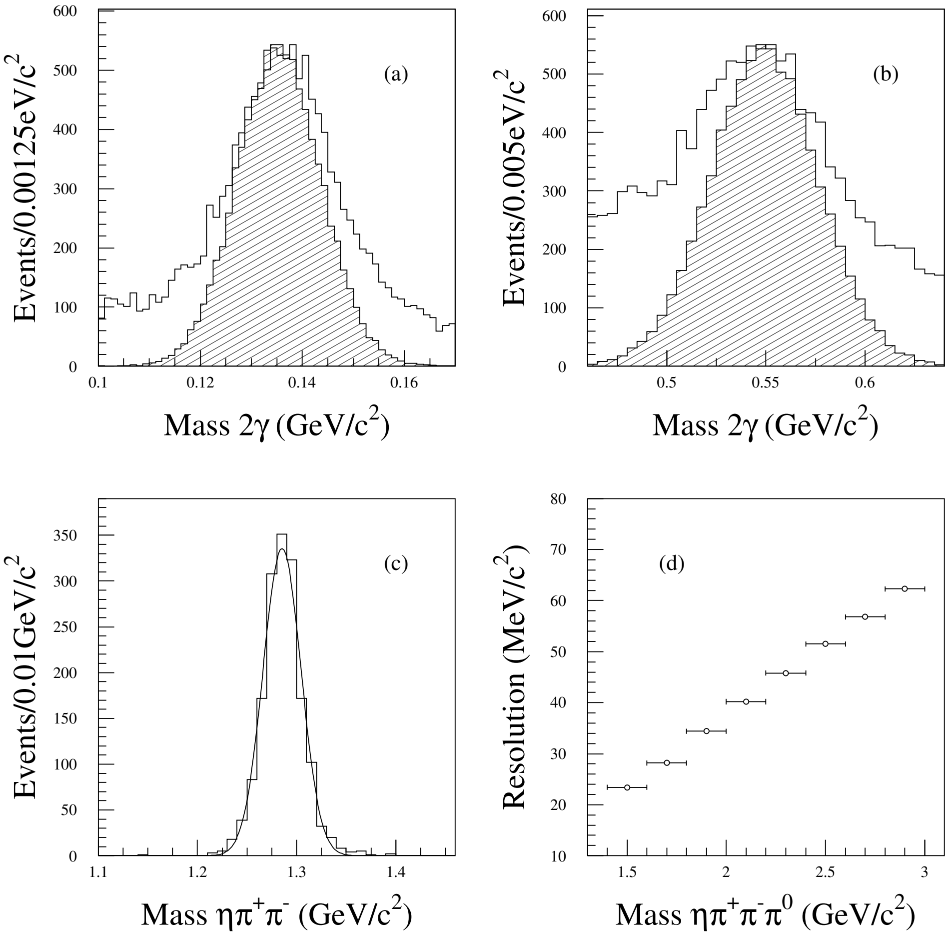

Figure 5.14: (a) Mass spectrum for π^0. Open histogram shows observed data and hatched one shows simulated data. (b) Same as (a) but for η. (c) Mass spectrum for $f_1(1285)$ obtained by simulation. The width of $f_1(1285)$ is input as zero. (d) Estimated mass resolution for $\eta\pi^+\pi^-\pi^0$ system as a function of mass.

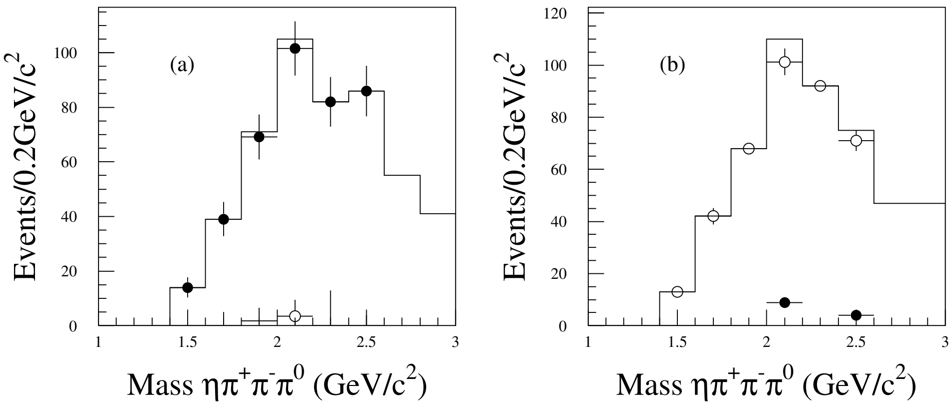

Figure 5.15: Results of the fit to the simulated data samples. (a) Phase space events. (b) 1010 spin model events. Closed circles represent background intensities and open circles represent 1010 wave intensities, obtained from the fit.

has been renormalized using a common factor through all spin models so that the background term $(1-\sum_j a_j)$ represents phase space background events correctly. To obtain the proper normalization factor, data samples generated by simulation have been used. The normalization factor has been adjusted so that $a_j \sim 0$ for phase space events and $a_j \sim 1$ for spin model j events are obtained in the fit. Figure 5.15 shows the fit results for input of the phase space events and spin model 1010 events. Figure 5.16 is same as Fig. 5.15 but for the case of the spin model 2211. For the spin model 1010, the detector acceptance is minimum while it is maximum for the spin model 2211. Figures 5.15 and 5.16 shows the probability weights P_j for both spin models have been properly normalized relative to the background term with a common normalization factor.

Data samples of the 1995 and 1996 runs were combined and included in the fit simultaneously. Each acceptance ϵ_j was normalized to the acceptance for the 0000 spin model in the 1995 run. Combined data sample was divided into three 0.4 GeV/c^2 mass bins from 1.4 to 2.6 GeV/c^2 so that each mass bin contains more than 100 $f_1(1285)\pi^0$ events. In order to estimate the number of $f_1(1285)\pi^0$ events, the number of events included in the $f_1(1285)$ peak on the $\eta\pi^+\pi^-$ spectrum has been calculated by the fit (see section 5.2). Figure 5.17 shows the $\eta\pi^+\pi^-$ spectra and estimated numbers of $f_1(1285)$ signals in three mass intervals.

In each mass bin, the log likelihood function (5.16) was calculated separately and the negative value of the function was minimized using the CERN library package MINUIT[46], by varying each event fraction a_j.

At first only a single spin model has been included in the fit. Table 5.1 shows the likelihood difference from the case of the 0000 spin model. Only three waves

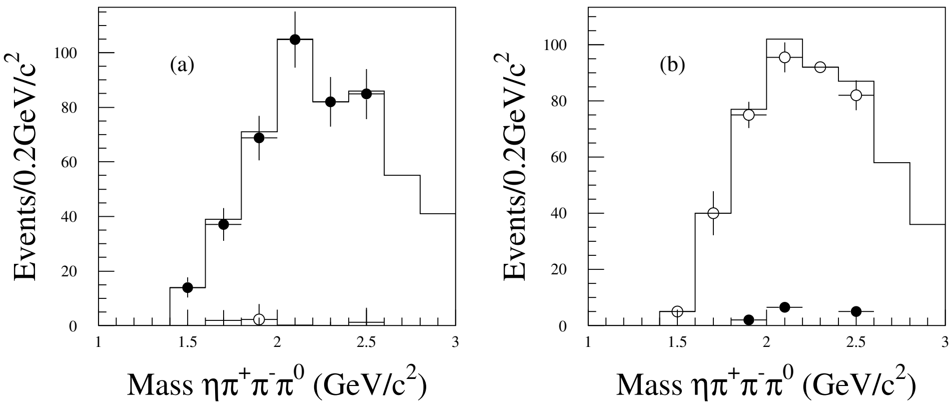

Figure 5.16: Same as Fig. 5.15 but in the case of 2211 spin model.

with the largest likelihood values in each mass bin are shown in the table. For the purpose of the comparison, the likelihood differences of $1^{++}[f_1(1285)]$ waves are also presented. Results of the fit are summarized as follows:

- In the 1.8–2.2 and 2.2–2.6 GeV/c^2 mass bins, two $J^{PC} = 1^{-+}$ waves, $1^{-+}[f_1(1285)]1$ and $1^{-+}[\eta(1295)]0$, have large likelihood values.
- The $1^{++}[f_1(1285)]$ wave, which was observed dominantly at ~ 1.7 GeV/c^2 in the $\pi^- p$ diffractive reaction, has considerably small likelihood values both in $M = 0$ and 1.

Then two waves which have large likelihood value in each single model fit have been included in the fit. Table 5.2 shows the results of the fit. The best fitted combination in each mass bin is presented on the top of the table and likelihood differences represent differences relative to the likelihood of the best fitted combination. The results of the fit are summarized as follows:

- In the 1.4–1.8 GeV/c^2 mass bin, any combination does not give so different likelihood value than other combinations. Moreover, the fit with two waves does not improve the likelihood so much compared with the case of the fit with a single wave ($\sim +1.4$).
- In the 1.8–2.2 and 2.2–2.6 GeV/c^2 mass bins, a combination of 1^{-+} waves, $1^{-+}[f_1(1285)]1$ and $1^{-+}[\eta(1295)]0$, gives the largest likelihood, and the likelihood difference between this best fitted combination and other combinations are significantly large ($\sim +4 = 3\sigma$).

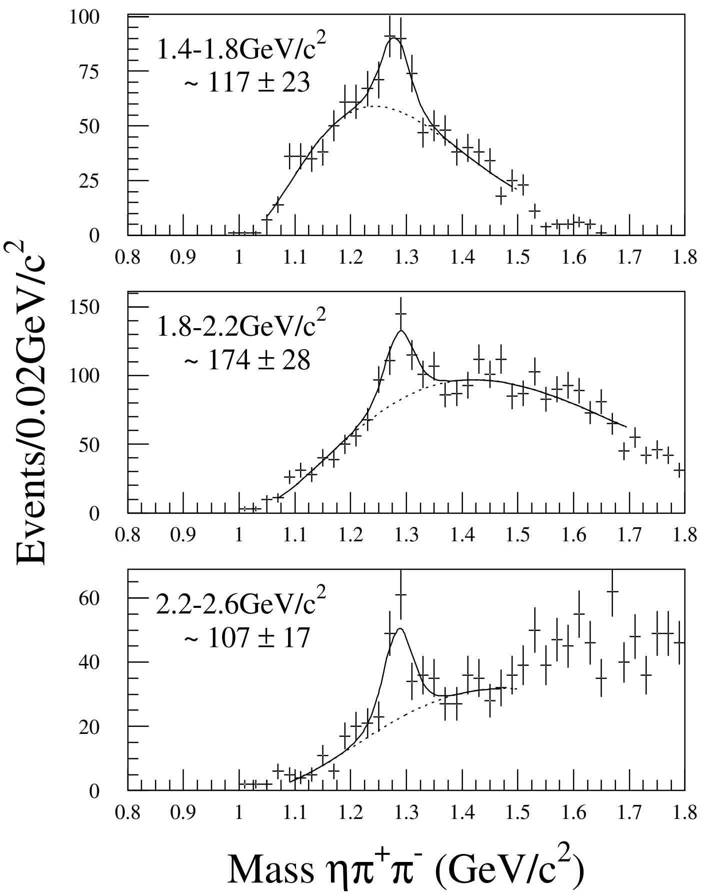

Figure 5.17: $\eta\pi^+\pi^-$ spectra and estimated numbers of $f_1(1285)$ signals in three $\eta\pi^+\pi^-\pi^0$ mass intervals. The curve in each plot shows the fit by a Breit-Wigner convoluted with a Gaussian and a background of the conventional form.

J^{PC}[isobar]M	1.4–1.8*	1.8–2.2*	2.2–2.6*
$0^{-+}[\eta(1295)]0$	0	0	0
$1^{-+}[\eta(1295)]1$	−0.2		
$1^{-+}[\eta(1295)]0$		+2.4	**+8.7**
$1^{-+}[f_1(1285)]1$	**+0.6**	**+7.8**	+4.3
$2^{++}[f_1(1285)]2$		+2.8	
$2^{-+}[f_1(1285)]1$	+0.3		
$2^{-+}[f_1(1285)]0$	+0.3		+3.5
$1^{++}[f_1(1285)]1$	−5.5	−1.7	+0.4
$1^{++}[f_1(1285)]0$	−3.7	−8.8	−4.5

* in GeV/c^2.

Table 5.1: Likelihood differences in the case of the single spin model included in the fit. Only three waves with the largest likelihood values in each mass bin are shown in the table, together with $1^{++}[f_1(1285)]$ waves.

- In the 1.8–2.2 and 2.2–2.6 GeV/c^2 mass bins, the best fitted combination also gives larger likelihood compared with the case of the fit with a single wave: +3.8 for 1.8–2.2 GeV/c^2 and +7.8 for 2.2–2.6 GeV/c^2.

Results of the fit are plotted in Fig. 5.18. Figure 5.18(a) presents total events input for the fit and backgrounds estimated from the fit. The ratio of signals to backgrounds has been well reproduced by the fit in each mass bin. Figure 5.18(b) shows partial wave intensities for the best fit combination in each mass bin.

In order to check the validity of PWA, the following procedures have been done:

(a) The best fitted combination in each mass bin has been fitted to the 100% phase space event (simulation).

(b) To check the significance of likelihood differences obtained in the fit, the same fitting procedures have been attempted for the simulated data sample, which consist of the same spin components and backgrounds with the same proportions as obtained from the fit to the real data sample.

From the check (a), it has been found that all event fractions for waves included in the fit become consistent with zero. This guarantees that any wave has not been produced artificially.

For the check (b), data sample input for the fit have been constructed as follows:

	1.8–2.2	2.2–2.6
phase space	620	170
$1^{-+}[f_1(1285)]1$	100	50
$1^{-+}[\eta(1295)]0$	50	50

1.4–1.8 GeV/c^2	
$0^{-+}[\eta(1295)]0+2^{-+}[f_1(1285)]1$	0
$1^{-+}[f_1(1285)]1+2^{-+}[f_1(1285)]1$	-0.1
$1^{-+}[f_1(1285)]1+1^{-+}[\eta(1295)]1$	-0.7
$0^{-+}[\eta(1295)]0+1^{-+}[f_1(1285)]1$	-1.0

1.8–2.2 GeV/c^2	
$1^{-+}[f_1(1285)]1+1^{-+}[\eta(1295)]0$	0
$1^{-+}[f_1(1285)]1+0^{-+}[\eta(1295)]0$	-3.8
$1^{-+}[f_1(1285)]1+1^{-+}[\eta(1295)]1$	-3.8
$1^{-+}[f_1(1285)]1+2^{++}[f_1(1285)]2$	-3.8

2.2–2.6 GeV/c^2	
$1^{-+}[f_1(1285)]1+1^{-+}[\eta(1295)]0$	0
$2^{-+}[f_1(1285)]0+1^{-+}[\eta(1295)]0$	-4.4
$1^{-+}[f_1(1285)]1+2^{-+}[f_1(1285)]0$	-4.5
$0^{-+}[\eta(1295)]0+1^{-+}[\eta(1295)]0$	-5.9

Table 5.2: Likelihood differences in the case of two waves included in the fit. The best fitted combination in each mass bin is presented on the top of each table and likelihood differences are relative to the best fitted combination.

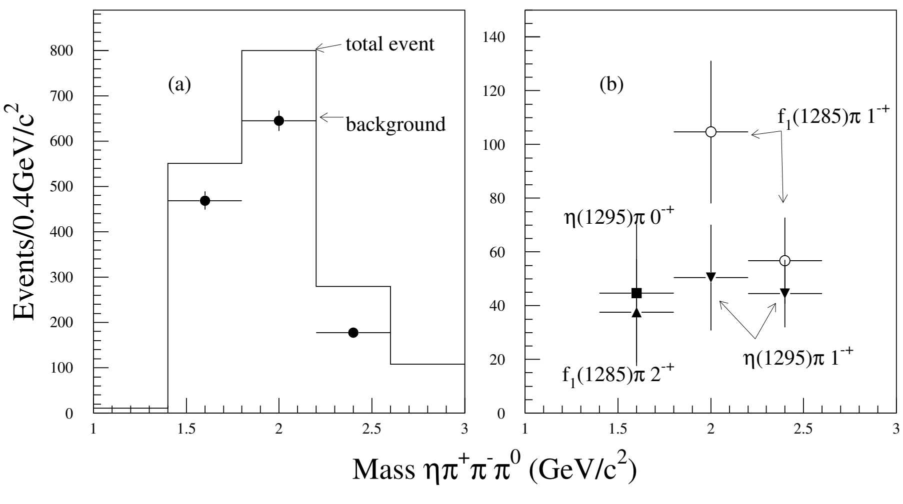

Figure 5.18: Results of the fit. (a) Total events input for the fit (histogram) and backgrounds estimated from the fit (closed circles). (b) Partial wave intensities for the best fit combination in each mass bin.

1.8–2.2 GeV/c^2	
$1^{-+}[f_1(1285)]1$+$1^{-+}[\eta(1295)]0$	0
$1^{-+}[f_1(1285)]1$+$0^{-+}[\eta(1295)]0$	-2.1
$1^{-+}[f_1(1285)]1$+$1^{-+}[\eta(1295)]1$	-3.4
$1^{-+}[f_1(1285)]1$+$2^{++}[f_1(1285)]2$	-3.5

2.2–2.6 GeV/c^2	
$1^{-+}[f_1(1285)]1$+$1^{-+}[\eta(1295)]0$	0
$2^{-+}[f_1(1285)]0$+$1^{-+}[\eta(1295)]0$	-4.0
$1^{-+}[f_1(1285)]1$+$2^{-+}[f_1(1285)]0$	-6.5
$0^{-+}[\eta(1295)]0$+$1^{-+}[\eta(1295)]0$	-3.6

Table 5.3: Likelihood differences for the fit to a simulated data sample.

Since the components of the real events in the 1.4–1.8 GeV/c^2 mass bin are not clear from the fit, only 1.8–2.2 and 2.2–2.6 GeV/c^2 mass bins have been concerned. The results of the fit to this data sample are presented in Table 5.3 and Fig. 5.19. Figure 5.19 shows event fractions obtained from the fit reproduce the proportions of event components well even if signals are mixed with a rather larger number of background events. For the fit to the simulated data sample, the almost same combinations of spin models as the case of the fit to real data sample have large likelihood values and the likelihood difference between the best fit combination and other combinations has been found to be ~ 2.0 (2σ). From this result, it can be considered that the likelihood difference ~ 4.0 (3σ) in the case of the real data sample is clearly at the significance level.

In summary, results of PWA are:

- In the 1.8–2.2 and 2.2–2.6 GeV/c^2 mass bins, the combination of 1^{-+} waves, $1^{-+}[f_1(1285)]1$ and $1^{-+}[\eta(1295)]0$, is best fitted and has significantly larger likelihood values than other combinations ($\sim 3\sigma$).

- In the 1.4–1.8 GeV/c^2 mass bin, some different spin combinations have the almost same likelihood values (within $\sim 1\sigma$) therefore any dominant wave cannot be determined in this mass region.

- The $1^{++}[f_1(1285)]$ wave, which is observed dominantly at ~ 1.7 GeV/c^2 in the $\pi^- p$ diffraction reaction, has only a considerably small likelihood in any mass bin.

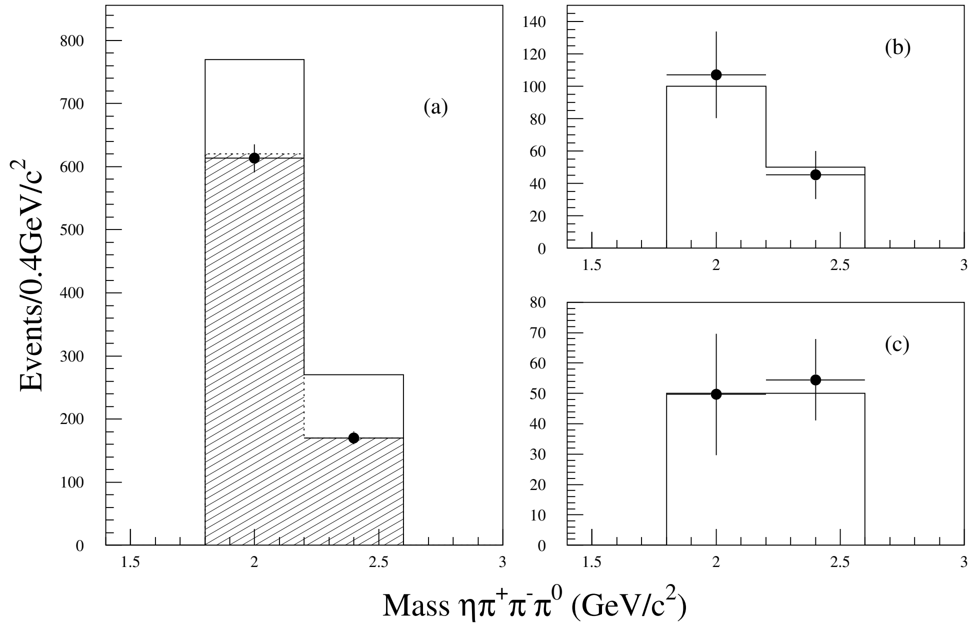

Figure 5.19: Results of the fit to a simulated data sample, which consists of the same components as estimated from the fit to the real data sample. (a) Total events input for the fit (open histogram) and phase space events (hatched histogram). Closed circles represent backgrounds estimated from the fit. (b) Input $1^{-+}[f_1(1285)]1$ events (histogram) and $1^{-+}[f_1(1285)]1$ wave intensities obtained from the fit (closed circles). (c) Same as (b) but for the $1^{-+}[\eta(1295)]0$ wave.

5.4 Discussion

The 1^{-+} wave is obtained in the $f_1(1285)\pi^0$ S-wave, therefore it is considered that this exotic wave can be created easily by the non-correlated $f_1(1285)\pi^0$ pair, which will form an isotropic angular distribution. The correlation between $f_1(1285)$ and π^0 has been tested by imposing a very narrow π^0 window, and found that the $f_1(1285)$ signal is enhanced against backgrounds by this cut (Fig. 5.3). This will support that $f_1(1285)$ and π^0 are produced in the mechanism of the central production, not by uneliminated background processes (for example, $f_1(1285)$ + δ-rays). However, this test is not responsible to whether the produced $f_1(1285)\pi^0$ system is a resonance or not.

In the case that the observed 1^{-+} wave is a non-resonance, a conclusion will be that any state which has the $f_1(1285)\pi$ decay mode has not been observed within the sensitivity of the present experiment (approximately 50 events/nb for the 1995 run[44]). The $f_1(1285)\pi^0$ channel has $I = 1$, thus this channel cannot be produced by the Double Pomeron Exchange (DPE) process. DPE is believed to dominate the central production process at high energies, since its cross section is predicted to be nearly constant against the energy variation while Reggeon-Pomeron and Reggeon-Reggeon exchange processes are predicted to have energy dependencies, s^{-1} and s^{-2}, respectively[7]. These prediction has been supported by the observation of ρ productions at different center-of-mass energies by WA76 collaboration[47]. WA76 took data of centrally produced $\pi^+\pi^-$ system at the center-of-mass energy of 12.7 and 23.8 GeV, and the suppression of ρ production has been clearly observed at $\sqrt{s} = 23.8$ GeV (Fig. 5.20). This may be able to be applied for the suppression of the $f_1(1285)\pi$ channel of the present experiment ($\sqrt{s} = 29$ GeV), which would make any resonant state missed from an observation in the present analysis.

If the $f_1(1285)\pi^0$ 1^{-+} wave is assumed as a resonant state, we may be able to claim that it is the hybrid state that the flux tube model predicts. At present there are no clear theoretical considerations for the connectivity between the central production process and the production of the hybrid states (or in other words, the contribution of "valence gluon" to the production of the hybrid states), but the observation of the strongest 1^{-+} intensity and the absence of significant intensities of other non-exotic waves which have been clearly observed in the peripheral reaction is considered to suggest an apparent difference between their production mechanisms and a dominant production of the 1^{-+} state in the "gluon rich" $I = 1$ process, which would be formed by the "Reggeon–Pomeron" exchange.

It is interesting to refer the other channels of the central production process. Figure 5.21 presents the mass spectrum of the $\eta'\pi^0$ system obtained by the same event selection as the $f_1(1285)\pi^0$ channel, except imposing the η' cut ($0.91 < M(\eta\pi^+\pi^-) < 1.02$ GeV/c^2) instead of the $f_1(1285)$ cut. Because of the limited statistics, it is impossible to carry out the partial wave analysis. However, the obtained spectrum shows a very similar structure as that of the $\eta'\pi^-$ system of VES[19] (see Fig. 2.3). The broad structure of the $\eta'\pi^0$ peaks around 1.7 GeV/c^2, which is expected to corre-

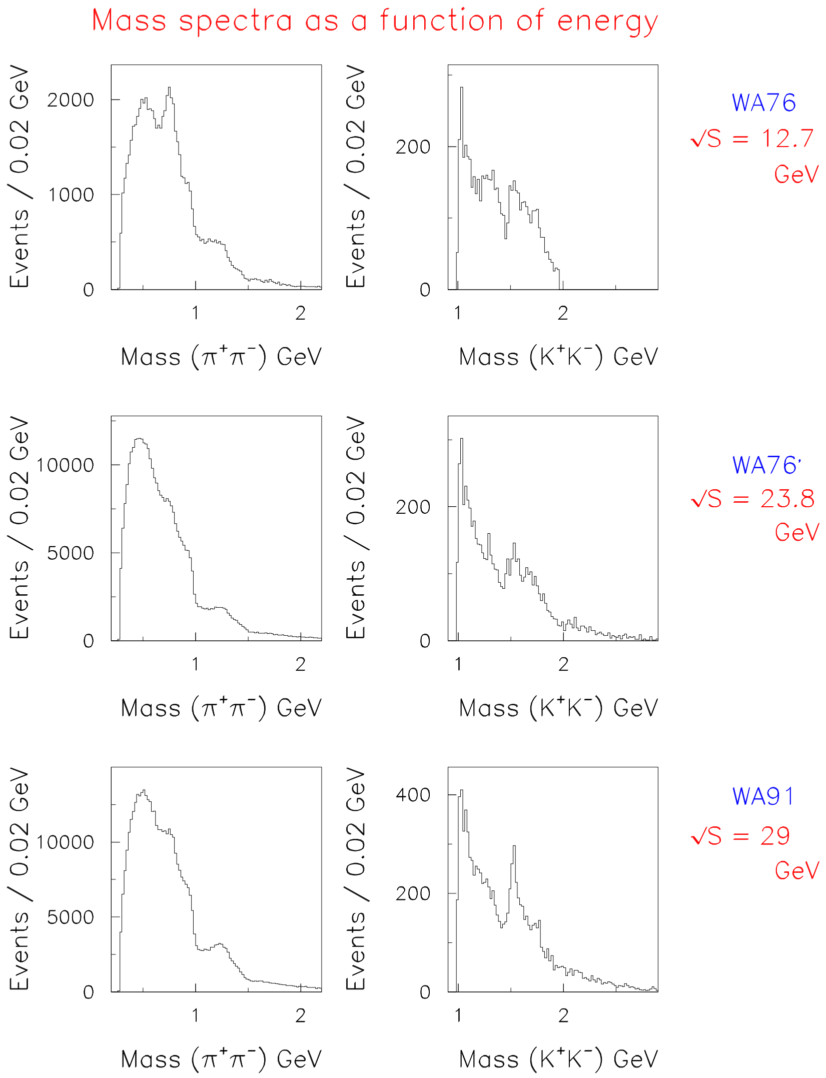

Figure 5.20: $\pi^+\pi^-$ (left) and K^+K^- (right) mass spectra at different center-of-mass energies[48]. It is observed that the peak of ρ on the $\pi^+\pi^-$ mass spectrum becomes smaller as the center-of-mass energy becomes higher relative to the background. The peak on the K^+K^- is $f_2'(1525)$.

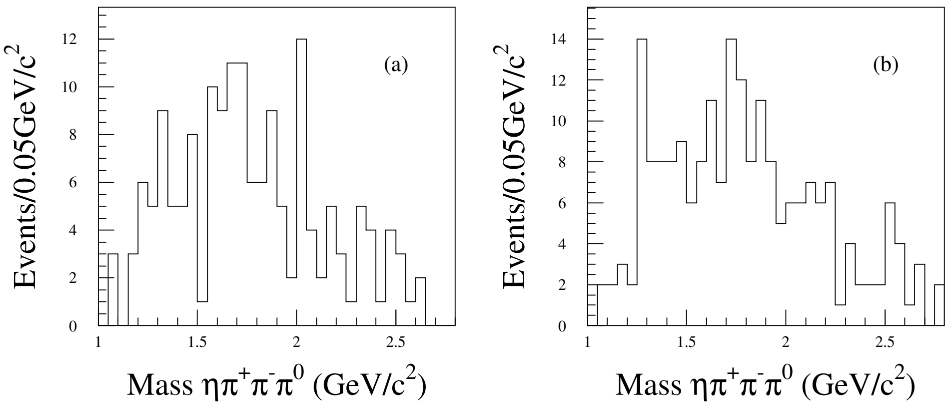

Figure 5.21: (a) Mass spectrum of the $\eta\pi^+\pi^-\pi^0$ system with the η' cut obtained from the 1995 run and (b) 1996 run.

spond to the 1^{-+} intensity observed by VES, and the shoulder-like structure at ~ 1.3 GeV$/c^2$ may correspond to $a_2(1320)$ state[2]. The rough estimation of a ratio expected for the 1^{-+} intensities in the $\eta'\pi^0$ and $f_1(1285)\pi^0$ channel, which has been calculated by comparing the acceptance corrected number of η' and $f_1(1285)$ signals assuming almost all events would arise from each 1^{-+} state, gives $I(1^{-+}_{\eta'\pi^0})/I(1^{-+}_{f_1(1285)\pi^0}) \sim 0.7$. This value appears comparable to that of the preliminary results of VES[23], but is inconsistent with the prediction of the flux tube model (see Eq. 2.3).

In the analysis of the centrally produced $\pi^+\pi^-\pi^0$, the $\rho\pi$ 1^{-+} state was not reported[49]: addition of the $\rho\pi$ 1^{-+} wave to the likelihood fit produced very little change in the log likelihood and the distribution produced looked very much like a broad phase space[44]. Though it would happen that the strong signals from the $a_1(1260)$, $a_2(1320)$ and $\pi_2(1670)$ hide the relatively weak 1^{-+} signal, this results may support the prediction of the flux tube model that the decay of the hybrid states into $\rho\pi$ should be suppressed, if the preferential production of the hybrid state in the central production process is assumed.

Two preliminary results of the analysis of the centrally produced $\eta\pi^0$ channel are also negative to the existence of the 1^{-+} state in the $\eta\pi^0$ channel[50, 51], which is also consistent with the prediction of the flux tube model.

In summary, if the central production process is a good source of the hybrid states as the case of the glueballs, it is suggested that the analyses of the various centrally produced systems support the prediction of the flux tube model, except that for the $\eta'\pi$ channel. From the rough estimation of the ratio of the 1^{-+} intensities

[2]It is noted that the intensity of the mass region < 1.5 GeV$/c^2$ may have a large uncertainty due to the rejection cut for the $\eta\eta$ and $\eta\omega$ events (see section 5.1).

in the $\eta'\pi^0$ and $f_1(1285)\pi^0$ channel, and by seeing the preliminary results of the analysis of the $\eta'\pi^-$ channel by VES and E852, the observed 1^{-+} intensity of this channel appears not small compared with that of the $f_1(1285)\pi$ channel. If the 1^{-+} intensity of the $\eta'\pi$ channel is really comparable to that of the $f_1(1285)\pi$ channel, the selection rule given by the flux tube model that the decay of the hybrid states into $(L = 0) + (L = 0)$ pair should be strongly suppressed is considered to be broken far from the limit allowed by the difference of the spatial wave functions of final mesons[12]. This would be a crucial question for the validity of the flux tube model. The firm analysis results of VES and E852 for the $\eta'\pi$ and $f_1(1285)\pi$ channel should be waited. Of course, it must be clarified simultaneously whether the 1^{-+} wave in each channel is a hybrid state or not. For this purpose, it appears to be also needed to investigate the relation of the central production process and the production of the hybrid states, since the different appearance of the 1^{-+} wave in the different process will give hints for the understanding of the nature of each 1^{-+} wave. For that purpose, $b_1(1235)\pi^0$ channel should be analysed since this channel is also expected by the flux tube model to be dominant decay mode of the hybrid state and results of analysis of the $b_1(1235)\pi$ channel in the peripheral reaction will be provided by VES and E852 in the future. Moreover, it may be interesting to see the reaction which can be studied with data of the WA102 experiment, such as[44]

$$pp \to \Delta^{++} f_1(1285)\pi^- p_s. \tag{5.17}$$

In this kind of reaction, the exchange of both of Reggeon and Pomeron is more mandatory. Experimental data which belong to the reaction (5.17) is rejected by the "diffractive cut" in the usual analysis, but it looks quite worth trying for the searches for the hybrid states.

Chapter 6

Conclusion

The existence of hadronic matters with extra gluonic degree of freedoms is naturally predicted by the non-Abelian nature of QCD. To confirm the existence of such states, glueballs and hybrids, would be a direct proof of the non-Abelian nature of QCD and thus it is one of main subjects of the present hadron physics. Currently many experiments have been trying to disclose the existence of such exotic states by searching them in “gluon rich” reaction processes, and now many candidates have been reported.

The WA102 experiment was performed to study one of such “gluon rich” processes, the central production process. In this thesis, a hybrid meson, which has the exotic quantum number $J^{PC} = 1^{-+}$ and is strongly predicted to decay into the $f_1(1285)\pi$ channel, was concerned and a detailed analysis was done using $\eta\pi^+\pi^-\pi^0$ data obtained in the WA102 experiment.

Total of 1811 events were selected from the 1995 and 1996 data as centrally produced $f_1(1285)\pi^0$ candidates, and a partial wave analysis based on the maximum likelihood fit method was attempted in order to obtain the spin parity of the observed system. As results, it was found that a combination of exotic 1^{-+} waves of the $f_1(1285)\pi^0$ and $\eta(1295)\pi^0$ was best fitted and gave about 3σ larger likelihood than other combinations in the 1.8–2.6 GeV/c^2 mass region. On the other hand, any combination did not have a significantly larger likelihood than the others in the 1.4–1.8 GeV/c^2 region. Especially the 1^{++} wave, which was observed dominantly at ~ 1.7 GeV/c^2 in all three previous π^-p diffractive reaction experiments, had only a considerably smaller likelihood in any mass bin.

In conclusion, only a combination of the exotic $f_1(1285)\pi^0$ and $\eta(1295)\pi^0$ 1^{-+} waves was observed with a significant likelihood difference. As it was impossible to see the phase motion of waves due to the limited statistics, it cannot be concluded that the 1^{-+} waves are resonant states. However, it is considered that the clear appearance of the exotic 1^{-+} wave in the “gluon rich” central production suggest the hybrid nature of the 1^{-+} wave in the $f_1(1285)\pi$ channel.

In order to study further and disclose the nature of the 1^{-+} wave in the $f_1(1285)\pi$ channel, the analysis of the $b_1(1235)\pi^0$ channel is thought to be also needed. The

$b_1(1235)\pi^0$ channel has five pions in the final state, and thus its analysis is much more complicated than that for the $f_1(1285)\pi^0$ channel due to the multiplicity of pion combinations. However, the flux tube model predicts that the partial width of the $b_1(1235)\pi$ channel of the hybrid decay is about 3 times as large as that of the $f_1(1285)\pi$ channel. Therefore, if the 1^{-+} wave observed in the present analysis is truly a hybrid state, it should be also observed dominantly in the centrally produced $b_1(1235)\pi^0$ channel and this will be a test for the flux tube model.

For firm conclusions, the complete consistency between experimental results and theoretical explanations is necessary. Now apparent signs of 1^{-+} exotics have been observed in various channels. However, it has not been successful to classify all the observed 1^{-+} exotics into glueball, hybrid, four quarks, dimeson or "artifact" without any ambiguity nor any inconsistency. In order to confirm the existence of the hybrid meson, it is thought to be needed to understand not only the 1^{-+} exotic in the $f_1(1285)\pi$ channel but also those in other channels correctly.

Bibliography

[1] Particle Data Group, Phys. Rev. **D54** (1996) 1.

[2] F. E. Close, *An Introduction to Quarks and Partons*, Academic Press (1979).

[3] F. Halzen and A. D. Martin, *Quarks and leptons: An Introductory Course in Modern Particle Physics*, John Wiley & Sons (1984).

[4] G. Bali *et al.*, Phys. Lett. **B309** (1993) 378.

[5] D. Weingarten, Nucl. Phys. Proc. Supp. **B34** (1994) 29.

[6] *Proceedings of the 7th Int. Conf. on Hadron Spectroscopy*, edited by S. U. Chung and H. J. Willutzki (American Institute of Physics Conference Proceedings, New York, 1997).

[7] S. N. Ganguli and D. P. Roy, Phys. Rep. **67** (1980) 203.

[8] S. Okubo, Phys. Lett. **5** (1963) 165.

[9] G. Zweig, CERN-TH/401, 402, 412 (1964).

[10] J. Iizuka, Prog. Theor. Phys. Suppl. **37–38** (1966) 21.

[11] N. Isgur and J. Parton, Phys. Rev. **D31** (1985) 2910.

[12] N. Isgur, R. Kokoski and J. Paton, Phys. Rev. Lett. **54** (1985) 869.

[13] R. Kokoski and N. Isgur, Phys. Rev. **D35** (1987) 907.

[14] F. E. Close and P. R. Page, Nucl. Phys. **B443** (1995) 233.

[15] D. Alde *et al.*, Phys. Lett. **B205** (1988) 397.

[16] Yu. D. Prokoshkin and S. A. Sadovsky, Phys. Atom. Nucl. **58** (1995) 606.

[17] Yu. D. Prokoshkin and S. A. Sadovsky, Phys. Atom. Nucl. **58** (1995) 853.

[18] H. Aoyagi *et al.*, Phys. Lett. **B314** (1993) 246.

[19] G. M. Beladidze *et al.*, Phys. Lett. **B313** (1993) 276.

[20] D. R. Thompson *et al.*, Phys. Rev. Lett. **79** (1997) 1630.

[21] A. Abele *et al.*, Phys. Lett. **B423** (1998) 175.

[22] F. E. Close and H. J. Lipkin, Phys. Lett. **B196** (1987) 245.

[23] Y. P. Gouz *et al.*, *Proceedings of the XXVI Int. Conf. on High Energy Physics*, edited by J. R. Sanford (American Institute of Physics Conference Proceedings No. 272, New York, 1993), p. 572.

[24] J. H. Lee *et al.*, Phys. Rev. **B323** (1994) 227.

[25] T. Adams, *Proceedings of the 7th Int. Conf. on Hadron Spectroscopy*, edited by S. U. Chung and H. J. Willutzki (American Institute of Physics Conference Proceedings, New York, 1997), p. 104.

[26] D. Alde *et al.*, Phys. Lett. **B216** (1989) 447.

[27] P. Lacock *et al.*, Phys. Lett. **B401** (1997) 308.

[28] A. Donnanchie and P. R. Page, Phys. Rev. **D58** (1998).

[29] G. Ascoli *et al.*, Phys. Rev. **D8** (1973) 3894.

[30] F. Binon *et al.*, Nucl. Instr. and Meth. **A248** (1986) 86.

[31] F. Binon *et al.*, Nucl. Instr. and Meth. **A256** (1987) 444.

[32] J. C. Lassalle *et al.*, Nucl. Instr. and Meth. **176** (1980) 371.

[33] A. A. Lednev, Nucl. Instr. and Meth. **A366** (1995) 292.

[34] A. A. Lednev, IFVE 93-153 (1993).

[35] G. A. Akopdjanov *et al.*, Nucl. Instr. and Meth. **140** (1997) 441.

[36] S. Abatzis *et al.*, Phys. Lett. **B324** (1994) 509.

[37] D. Barberis *et al.*, Phys. Lett. **B413** (1997) 217.

[38] D. Barberis *et al.*, Phys. Lett. **B440** (1998) 225.

[39] A. V. Singovski, Nuovo Cim. **107** (1994) 1911.

[40] K. Gottfried and J. D. Jackson, Nuovo Cim. **33** (1964) 309.

[41] K. L. Norman, *An Analysis of the Centrally Produced $\pi^+\pi^-$ System at 450 GeV/c*, PhD Thesis, Birmingham (1996).

[42] M. A. Reyes *et al.*, Nucl. Phys. Proc. Suppl. **56A** (1997) 285.

[43] D. J. Herndon *et al.*, Phys. Rev. **D11** (1975) 3165.

[44] A. Kirk, private communication.

[45] A. V. Singovski, private communication.

[46] F. James and M. Roos, *MINUIT Computer Physics Communications* 10 (1975).

[47] T. A. Armstrong *et al.*, Phys. Lett. **B228** (1989) 536.

[48] A. Kirk, Status report on experiment WA102 in CERN/SPSLC, unpublished (1996).

[49] D. Barberis *et al.*, Phys. Lett. **B422** (1998) 399.

[50] T. Kinashi, KEK Preprint 95-160 (1995).

[51] A. Sobol, LEAP'98 conference, unpublished (1998).